Electrochemical Ammonia Synthesis

Development of a Cell With a Hydrogen Permeable Electrode

Sidi D. Ruis

Delft University of Technology

TU Delft

Electrochemical Ammonia Synthesis

Development of a Cell With a Hydrogen Permeable Electrode

by

Sidi D. Ruis

to obtain the degree of Master of Science

at Delft University of Technology,

to be defended publicly on Thursday February 1, 2024 at 14:00.

Student number:	4720717	
Project duration:	March 1, 2023 – February 1, 2024	
Thesis committee:	Prof. dr. ir. F. M. Mulder,	TU Delft, TNW, responsible supervisor
	Prof. dr. ir. A. Urakawa	TU Delft, TNW
	Dr. ir. R. Kortlever,	TU Delft, ME
	D. D. van Noordenne,	TU Delft, TNW, daily supervisor

Cover: Generated with Canva Magic Media using 'metal catalyst surface' as prompt.

An electronic version of this thesis is available at http://repository.tudelft.nl/.

TU Delft

Summary

Climate change and its negative consequences for both nature and human health and welfare necessitate a sharp reduction in anthropogenic greenhouse gas emissions [1]. Ammonia is an essential chemical for global food security, while its conventional production through the Haber-Bosch process accounts for 1.4% of global carbon dioxide emissions and 2% of global energy consumption [2]. Furthermore ammonia is an interesting molecule for energy storage, as it is easily liquefied and energy dense [3]. Hence, decarbonising ammonia production through electrochemical ammonia synthesis is a highly relevant topic for the energy transition. The goal of an active, stable, and selective catalyst for dinitrogen reduction to ammonia has proven to be extremely challenging. Competition with hydrogen evolution, mass transport limitations in aqueous electrolytes, and the stability of dinitrogen's triple bond are the primary challenges in conventional cell designs [4]. In earlier research [5], an unconventional cell design with a non-porous, hydrogen permeable metal electrode has been demonstrated, in which the generation of hydrogen is physically separated from the catalytic nitrogen activation and hydrogenation to ammonia. This design has potential to overcome the challenges mentioned above.

This research aims to build on an earlier study reporting a stable ammonia production rate when elevating the cell temperature to 120 °C [6]. The study used nickel hydrogen permeable electrodes with a nickel nitride (Ni_3N) surface. Broadening the understanding of the reaction mechanism of ammonia synthesis with a hydrogen permeable electrode and demonstrating methods to improve the ammonia production rate are the main goals. A further improvement in ammonia production rate was deemed achievable through an increase in cell pressure. The raised pressure was expected to increase nitrogen adsorption on the gas side of the electrode, and hydrogen permeation from the electrolyte side. When nitrogen adsorption is the limiting reaction step, a pressure increase would yield a proportional increase in ammonia production rate. Moreover, enhancing the electrochemical active surface area of the electrode was investigated as a method to improve ammonia production.

An experimental setup was built to allow operation of the hydrogen permeable electrode cell at elevated pressure. Nitrogen was deposited onto nickel foil electrodes using two methods of plasma enhanced chemical vapour depositioning, creating a nickel nitride surface layer. The surface composition of the treated electrodes was analysed, and depth profiles were made to determine the N content of the nitride layer. Subsequently, these electrodes were used in the ammonia synthesis cell, using in-line gas chromatography to analyse the product gases. Presence of a catalytic reaction from gaseous N_2 to NH_3 was confirmed using a control experiment with argon gas. The NH_3 production rate and H permeation were measured at different operating parameters to determine the effect of pressure, temperature and current density. Furthermore, electrodes with increased electrochemical surface area were produced through electrodeposition of nickel nanostructures on the nickel foil electrodes. The effect of this treatment was confirmed using electric double layer capacitance measurements of the electrodes before and after the electrodeposition, and the electrode surface structure was examined using SEM.

The results show a significant increase in hydrogen permeation and ammonia production rate through increasing temperature, and a modest beneficial effect from a pressure increase, that does not extend to pressure increases beyond 2 bar. Overall, the stable production in [6] could not be reproduced without the associated experimental data being available. The present research identified nitrogen adsorption on the hydrogen permeable electrode as the limiting elementary step, gaining prevalence over time as the abundance of pre-deposited nitrogen decreases. Nitrogen activation and adsorption by the nickel nitride surface is insufficient to replenish N vacancies resulting from ammonia synthesis. Nickel nitride more readily activates nitrogen than pure nickel, further reducing nitrogen adsorption over time. With sufficient nitrogen available from the nitride layer, hydrogenation of nitrogen is most probably the limiting step. Results from the present research also reveal decomposition of the Ni_3N on the hydrogen permeable electrode to ammonia, and possibly to dinitrogen. This decomposition is accelerated by elevated temperatures and the presence of hydrogen.

For future research, it is recommended to raise the cell pressure further, aiming to balance the reaction steps through increasing nitrogen adsorption. Furthermore, the presence of a decomposition reaction of the nickel nitride should be investigated, determining a stability window for the catalyst. Finally, introduction of an additional catalyst component that promotes regeneration of the nitride through nitrogen adsorption is recommended, to combine the favourable properties of the nickel nitride electrode with the enhanced nitrogen adsorption of another material. Overall, these findings in this research expand the understanding of the mechanisms underlying the nitrogen reduction reaction, paving the way for the development of a more efficient green ammonia synthesis process.

Acknowledgements

This project would not have been possible without the crucial support and expertise of my professor Fokko Mulder. I am also deeply grateful to my supervisor Dylan van Noordenne, who provided invaluable feedback and was always ready to discuss ideas. Special thanks to Herman Schreuders and Joost Middelkoop, who have helped me countless times with troubleshooting the setup and the use of lab systems.

Many thanks to my fellow students at MECS, it was a pleasure to be working alongside you and exchange ideas. Thanks should also go the MECS employees, for their moral support and interest in the project. I picked up a multitude of valuable ideas during coffee breaks and group meetings. Thank you to Roos Roeling for helping with the organisation of the defence.

Lastly, I would like to mention my family and friends, especially my parents, who have always supported and believed in me. And Evie, for always making me happy.

I cannot deny that this project has been challenging, and the results would sometimes not be what we had been hoping for or expecting. But without difficulties there is no learning, and the experience became all the more enriching because of it. With perseverance and ingenuity, the brightest days for green ammonia are certainly ahead.

Sidi
Delft, January 2024

The simple truth is that truth is hard to come by, and that once found may easily be lost again.
Karl Popper

Contents

List of Figures

List of Tables

Nomenclature

Abbreviations

ALD Atomic Layer Deposition
BCC Body-Centered Cubic
DFT Density Functional Theory
ECSA Electrochemical Active Surface Area
EDL Electric Double Layer
EDS Electron Diffraction X-Ray Spectroscopy
EPDM Ethylene Propylene Diene Monomer
FCC Face-Centered Cubic
FE Faradaic Efficiency
FEA Finite Element Analysis
FED Free Energy Diagram
GC Gas-Chromatography
GDE Gas Diffusion Electrode
GHG Greenhouse Gas
GSA Geometric Surface Area
HCP Hexogonal Close-Packed
HER Hydrogen Evolution Reaction
HOMO Highest Occupied Molecular Orbital
HPE Hydrogen Permeable Electrode
IHP Inner Helmholtz Plane
IPCC Intergovernmental Panel on Climate Change
LUMO Lowest Unoccupied Molecular Orbital
MFC Mass Flow Controller
ML Monolayer
MvK Mars-van Krevelen
Ni_3N Nickel Nitride
NRR Nitrogen Reduction Reaction
OCP Open Circuit Potential
OER Oxygen Evolution Reaction
OHP Outer Helmholtz Plane
OPH Overpotential H
PDD Pulsed Discharge Ionisation Detector
PDS Potential Determining Step
PEEK Polyether Ether Ketone
PTFE Polytetrafluorethylene

RDS Rate Determining Step
RF Roughness Factor
SEM Scanning Electron Microscopy
TCD Thermal Conductivity Detector
TM Transition Metal
TMN Transition Metal Nitride
UHV Ultra High Vacuum
UPH Underpotential H
XPS X-Ray Photoelectron Spectroscopy

Symbols

Symbol	Definition	Unit
A	(Electrode) area	[cm^2]
a	Exponential prefactor	[-]
a_i	Chemical activity	[-]
b	Exponent in Sieverts' Law	[-]
C	Capacitance	[F]
c	Specific capacitance	[$F\,cm^{-2}$]
c_i	Molar concentration of species i	[$mol\,L^{-1}$]
c_0	Standard molar concentration, 1 $mol\,L^{-1}$	[$mol\,L^{-1}$]
D	Diffusivity coefficient	[$m^2\,s^{-1}$]
d	Distance	[various units]
E	Cell potential	[V]
E^0	Equilibrium cell potential	[V]
E^0_{th}	Thermoneutral cell potential	[V]
E_b	Electron binding energy	[eV]
E_p	Photon energy	[eV]
E_k	Kinetic energy of electron	[eV]
E_a	Activation energy	[$kJ\,mol^{-1}$]
ΔE_{vac}	Free energy difference between an N vacancy on the surface and in the first sub-surface layer	[$kJ\,mol^{-1}$]
e	Electron charge	$1.602 \cdot 10^{-19}$ C
F	Faraday constant	$9.6485 \cdot 10^4\,C\,mol^{-1}$
$f(\theta)$	Surface coverage coefficient	[-]
ΔG	Gibbs free energy change	[J]
ΔG^0	Gibbs free energy change for a electrochemical reaction in equilibrium	[J]
ΔH	Enthalpy change	[J]
i	Current density	[$A\,cm^{-2}$]

i_0	Exchange current density	[A cm^{-2}]
I	Current	[A]
k	Reaction rate constant	
k_B	Boltzmann constant	$1.381 \cdot 10^{-23}$ J K^{-1}
L_v^0	Ostwald coefficient	[-]
M	Molar mass	[g mol^{-1}]
$\dot{m}$	Mass flow rate	[mL$_n$ s^{-1}]
N_i	Permeation flux density of species i	[mol m^{-2} s^{-1}]
n	Number of electrons transferred per mole of product in a half reaction	[-]
P	Permeability coefficient	[mol m^{-1} bar$^{-0.5}$]
p	Pressure	[Pa]
p_i	Partial pressure for species i	[Pa]
Q	Reaction quotient	[-]
q	Charge	[C]
R	Universal gas constant	[J mol^{-1} K^{-1}]
r	Specific reaction rate	[mol cm^{-2} s^{-1}]
r_{ads}	Molar adsorption rate	[mol cm^{-2} s^{-1}]
S	Solubility coefficient	[mol m^{-3} bar$^{-0.5}$]
s	Sticking coefficient	[-]
ΔS	Entropy change	[J K^{-1}]
T	Temperature	[K]
U	Applied potential	[V]
u_i	Specific molar production rate of species i	[mol cm^{-2} s^{-1}]
V_g	Volume of dissolved gas	m^3
V_l	Volume of liquid solvent	m^3
V_c	Deposition growth in the dislocation core direction	s^{-1}
V_o	Deposition growth in the outer edge direction	s^{-1}
v	Potential scan rate	V s^{-1}
V_{RHE}	Potential relative to RHE	[V]
x_i	Mole fraction of species i in a mixture	[-]
z_i	Charge number of species i	[-]

β	Symmetry factor of a faradaic current described by the Butler-Volmer equation	[-]
Γ	Molecular flux	[mol cm^{-2} s^{-1}]
γ_i	Activity coefficient of species i	[-]
η	Overpotential	[V]
θ	Surface coverage fraction	[-]
$\kappa(\theta)$	Condensation coefficient	[-]

λ_i	Absolute activity of species i	[-]
λ_i^0	Absolute activity at standard conditions of species i	[-]
μ_i	Electrochemical potential of species i	[J mol^{-1}]
μ_i^0	Equilibrium electrochemical potential of species i	[J mol^{-1}]
ρ	Gravimetric density	[g cm^{-3}]
τ	Atomic density	[mol cm^{-2}]
Φ	Electric potential	[V]
Φ_m	Electric potential in a metal electrode	[V]
Φ_s	Electric potential in an electrolyte solution	[V]
ϕ	Work function correcting for energy losses between bulk emission and detection of a photoelectron in XPS	[eV]
φ	Fugacity coefficient	[-]

1 Introduction

1.1. Climate Change and the Shift to Renewable Energy

Climate change causes the earth's surface temperature to rise, leading to adverse effects to the environment, society, and the economy. The primary contributor to this temperature rise is the emission of Greenhouse Gases (GHGs) from human activities, particularly those associated with burning fossil resources [1]. To curb and potentially halt climate change, the Intergovernmental Panel on Climate Change (IPCC) emphasises the need to limit the temperature increase to 1.5 °C above pre-industrial levels [1]. Achieving this goal necessitates a substantial reduction in GHG emissions, aiming for net-zero emissions by 2050. Renewable energy sources, such as wind, solar, geothermal, and hydropower, offer a sustainable solution, providing clean and cost-effective energy. The decreasing cost of renewable power generation has made it competitive with fossil-based electricity [7]. Renewable electricity sources gain importance as the world transitions to a renewable energy-based society, while their daily and seasonal variations require new methods of energy storage. Chemicals such as ammonia could play an important role in this challenge [8].

1.2. Ammonia: Essential for Food Security and a Potential Energy Carrier

Ammonia is an essential component in fertilisers, with estimates indicating that half of the global population is dependent on synthetic nitrogen fertiliser [9]. The synthesis of ammonia from its elements is achieved industrially by the Haber-Bosch process, a thermochemical process reliant on steam-methane reforming and high-pressure conditions that accounts for 2% of global energy consumption and 1.4% of global carbon dioxide emissions [2]. Recognised for its high energy density and hydrogen content that enable large-scale energy storage and transportation, ammonia is a promising carbon-free energy carrier candidate [10]. However, the current reliance on the Haber-Bosch technology, fueled by natural gas, poses environmental challenges. To align with the net-zero emissions goal for 2050 of the Intergovernmental Panel on Climate Change (IPCC), ammonia production must transition to a sustainable pathway. Direct electrochemical nitrogen reduction to ammonia, powered by renewable energy sources, emerges as an environmentally friendly and flexible alternative. This can be achieved in the short to medium term by transitioning from steam-methane reforming to water electrolysis as the hydrogen source for the Haber-Bosch process. In the long term, direct electrochemical ammonia synthesis from nitrogen could be a pathway that enables decentralised operation with intermittent energy sources.

1.3. Overcoming Challenges in Electrochemical Ammonia Synthesis

The electrochemical conversion of N_2 to NH_3 in aqueous media faces several challenges, including low solubility of N_2 in water, competition with hydrogen evolution, and the complex activation of the N_2 molecule. Further challenges arise from catalyst poisoning by oxides, and issues related to the formation of stable intermediates on the catalytic surface that limit available sites for activation. The low NH_3 production rates cause difficulties with quantification, leading to irreproducible results and false positives from detection of contaminations [11]. Overcoming these challenges is crucial for realising the potential of electrochemical ammonia synthesis, an essential focus of the subsequent chapters in this thesis.

Recent research identified an unconventional cell design with a hydrogen permeable electrode as a possible pathway to overcome these challenges [12]. Through the use of a solid metal membrane that allows passage of hydrogen atoms, hydrogen generation is physically separated from the nitrogen activation and hydrogenation to ammonia. A further study showed that elevating the cell temperature to 120 °C resulted in a stable ammonia production reaction. The objective of this research is to expand the knowledge of the ammonia synthesis reaction mechanism for hydrogen permeable electrodes, and to develop this design concept further. The investigated improvement directions are elevating the cell pressure and modifying to the electrode surface morphology.

1.4. Research Questions and Project Goals

The project is aimed at deepening the understanding of the reaction mechanism of electrochemical ammonia synthesis using Hydrogen Permeable Electrodes (HPEs). This is achieved through a literature study and experimental work, where the goal is to devise and demonstrate methods that improve the ammonia production rate. The research questions are as follows:

1. What are the elementary reaction steps in NH_3 synthesis with HPEs?
    a. Which elementary steps are limiting?
    b. If present, what is the mechanism of deactivation?
2. How does increasing pressure in an NH_3 synthesis cell with an HPE affect the NH_3 production rate and faradaic efficiency?
    a. How can an NH_3 synthesis cell with an HPE be pressurised?
    b. How can the gas-chromatographic measuring equipment be used on a pressurised cell?
    c. How are the elementary steps influenced by an increase in pressure?
3. What are other strategies to improve the NH_3 production rate and faradaic efficiency in a cell with an HPE, apart from an increase in pressure?
    a. How does increasing the temperature affect the ammonia production rate and faradaic efficiency?
    b. How does modifying the electrode surface morphology affect the ammonia production rate?

1.5. Thesis Outline

A comprehensive literature review is presented in chapter 2. Starting out from the history of ammonia synthesis and the Haber-Bosch process, the field of electrochemical ammonia synthesis is explored on three further levels. Essential electrochemistry concepts are discussed, and subsequently used to understand electrochemical ammonia synthesis and its challenges in aqueous electrolytes. Next, the physics and chemistry of nitrogen reduction using hydrogen permeable electrodes are discussed, and hypotheses for the effect of the desired modifications are given. Finally, the used analysis techniques are discussed. chapter 3 details the design of the used experimental setups and methods. The results are presented and discussed in chapter 4, followed by conclusions and recommendations in chapter 5.

2

Ammonia Synthesis

Reactive nitrogen is essential for the sustenance life on earth. Ammonia (NH_3) is one of the primary forms of reactive nitrogen, which plants use to form more complex nitrogen containing compounds. Before the first successful synthesis of NH_3 from atmospheric nitrogen, the world had been utilising the limited reserves of naturally occurring reactive nitrogen for chemical processes and fertiliser production. Peruvian guano and Chilean saltpeter were the most prominent sources of reactive nitrogen [13], and in the early 20th century demand was threatening to outgrow the waning supply. Fritz Haber first synthesised NH_3 from nitrogen and hydrogen gas in 1908, while Carl Bosch succeeded in industrialising Haber's invention in 1913, making the resulting Haber-Bosch process the main method of nitrogen fixation since. It is estimated that since the 21st century, nearly half of the human population has been reliant on food containing synthetically fixated nitrogen for their survival [9]. Figure 2.1 shows how the exponential growth of the world population coincided with the sharp increase in annual ammonia production.

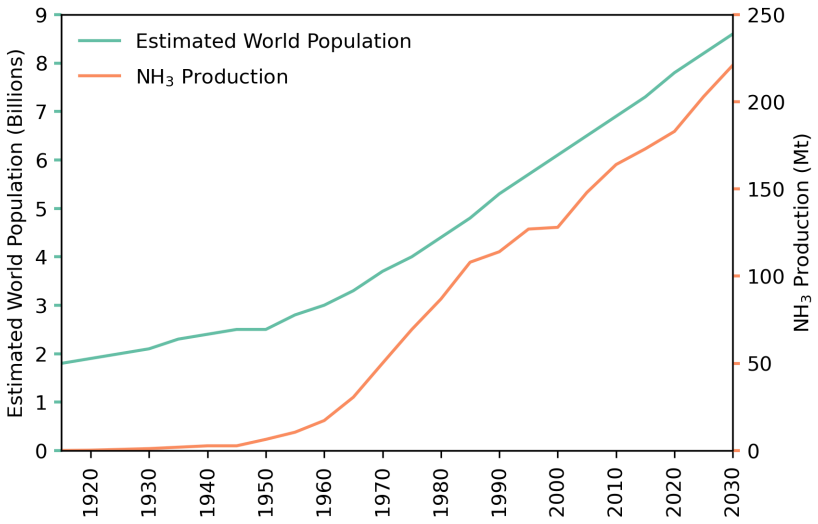

Figure 2.1: Development of world population and annual ammonia production during the the 20th century. The acceleration of population past 3 billion coincides with the growth of synthetic ammonia production. The plotted data after 2020 are predictions. Data obtained from [14].

Nowadays, ammonia is primarily used as a fertiliser and as feedstock for chemical processes. Apart from its uses as a bulk chemical, research interest into the potential of ammonia as an energy storage vector is growing. Ammonia can be liquefied at room temperature and a pressure of 8 bar, or at -33 °C and atmospheric pressure [15], enabling easy storage and transportation at large scale. Furthermore, the high energy density of 22.5 MJ kg^{-1} [16] is competitive with other potential energy storage molecules such as methanol. In 2020 the worldwide ammonia production was around 183 Mt [17]. Nearly this full amount is produced with the Haber-Bosch process, according to the highly exothermic reaction in Equation 2.1.

$$3\,H_2 + N_2 \rightleftharpoons 2\,NH_3 \quad (\Delta H^0 = -45.9\,\mathrm{kJ\,mol}^{-1}_{NH_3}) \tag{2.1}$$

The hydrogen source for the reaction is typically produced by steam methane reforming of natural gas or the gasification of coal, causing significant GHG emissions. The Haber-Bosch process, including heating and auxiliary equipment, accounts for around 2% of global energy consumption and 1.4% of annual CO_2 emissions [2]. Two thirds of these emissions are associated with hydrogen production, while the remainder originates from the ammonia synthesis loop [18].

Climate change caused by anthropogenic GHG emissions necessitates a transition to emission-free chemical processes. This is especially important for ammonia, given its significant contribution to global emissions, and its necessity in the global food supply. Three kinds of ammonia synthesis technology with different technology readiness levels are being developed in parallel. Since its invention, the Haber-Bosch process has been developed with a focus on increasing the energy efficiency, from 100 GJ $t^{-1}_{NH_3}$ in 1910 to 27 GJ $t^{-1}_{NH_3}$ at present [19]. This existing process together with future improvements can be classed as 1st generation ammonia synthesis, which can only be emission free by capturing the emissions from steam methane reforming, thus using what is called blue hydrogen. Fully replacing the blue ammonia feedstock with green ammonia produced through electrolysis will directly eliminate nearly all emissions. This change is currently nearing viability, and the technology can be classed 2nd generation ammonia synthesis. Beyond second generation ammonia synthesis lies the promise of departure from the Haber-Bosch process altogether. 3rd generation ammonia synthesis is the direct electrochemical reduction of nitrogen, thereby allowing for highly distributed implementation at any scale from kW to GW [8]. Research efforts into this technology are at an elementary stage, and different concepts are being actively studied.

This chapter starts with a short history of the Haber-Bosch process before moving on to the electrochemistry fundamentals needed to understand electrochemical ammonia synthesis. The concepts will be applied specifically to the nitrogen reduction reaction, and to the electrochemical ammonia synthesis cell with a hydrogen permeable electrode. Different strategies to improve the production rate and faradaic efficiency of electrochemical ammonia synthesis will be discussed.

2.1. History of the Haber-Bosch Process

Fixed nitrogen is a building block for living organisms, essential to the formation of amino acids and proteins. Natural fixation occurs through enzymatic processes in some bacteria (Rhizobium bacteria species), by atmospheric deposition, and from the recycling of crop waste and animal manures [20]. The yield of intensive agriculture is limited by the availability of reactive nitrogen. Already in 1798, Thomas R. Malthus recognised that the earth's finite resources were not sufficient to sustain the growth of global population, and warned about the possibility of large scale starvation [21]. A century later this prospect had come closer, as reserves of fixed nitrogen were dwindling. In 1898 at an address before the British Association for the Advancement of Science, Sir William Crookes argued that a method for synthetic nitrogen fixation was needed to fend off disaster, and pleaded the scientific community to develop this process [22]. Different processes would be developed in parallel in the decades thereafter. In 1908, within a decade from Crookes' speech, a thermochemical synthesis process was discovered by Fritz Haber, one year after Nernst had concluded that synthetic nitrogen fixation would be unfeasible.

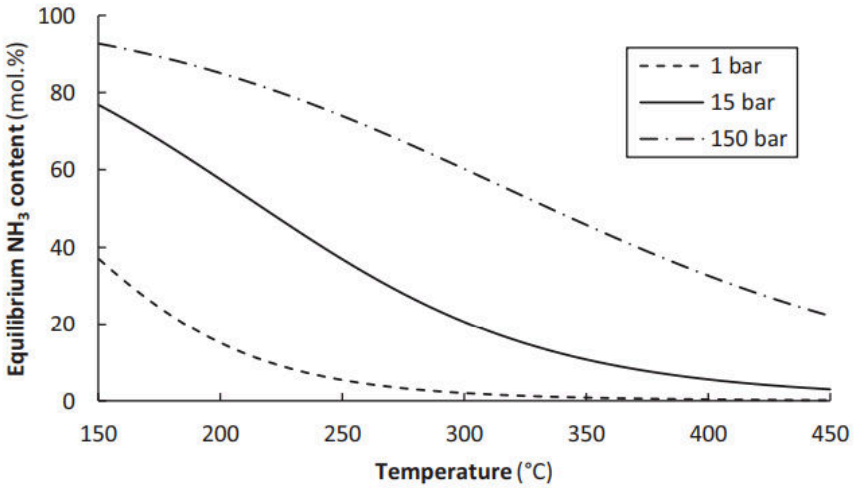

Figure 2.2: Equilibrium NH_3 mole fraction dependence on temperature and pressure, H_2:N_2=3:1. Due to the necessity of running at high temperatures for kinetics reasons, a high pressure is needed to achieve a viable conversion rate. Image reproduced from [25].

Haber demonstrated a process operating at a temperature of 500 °C and pressures between 100 bar to 200 bar with an osmium catalyst, producing 2 kg_{NH_3} d^{-1} [23]. A process with such extreme conditions, had never before been industrialised. Nevertheless, Carl Bosch and a team of scientists and engineers at Badische Anilin- und Soda-Fabrik (BASF) overcame the challenges within five years from Haber's discovery. The first industrial scale ammonia synthesis process would be started at a newly developed site in Oppau in 1913.

Haber was awarded the Nobel Prize for Chemistry in 1918 for the synthesis of ammonia from its elements. In 1931 the Nobel Prize was awarded to Bosch for his work on high pressure chemical processes. It is not without some irony that their inventions, similar to Nobel's own invention of dynamite, also had major use in armaments manufacturing. Both inventions show nitrogen is of great importance to explosives and chemical weapons production. With the Haber-Bosch process, Germany obtained a local source of fixed nitrogen to circumvent the blockade of Peruvian guano during the First World War. The need to improve munitions supplies was in reality a central motivation for industrial ammonia production [13].

Gerhard Ertl elucidated the reaction mechanism and kinetics of the Haber-Bosch process from the 1970s onward [24]. The forward reaction in Equation 2.1 is exothermic and thermodynamically favoured at lower temperatures and higher pressures. However, the reaction kinetics are prohibitively slow at low temperatures, therefore the process must imperatively be run at high temperatures. At typical Haber-Bosch conditions of between 100 and 300 bar and 450 to 500 °C, the conversion rate of H_2 and N_2 to NH_3 is still below 40%$_{mol}$. Figure 2.2 displays the effect of temperature and pressure on the equilibrium NH_3 content in the reactor. The low conversion rate means that a recycling loop is used in Haber-Bosch plants.

Developments in the Haber-Bosch process since its first successful industrial application are numerous. Major improvements in energy efficiency were achieved by the adoption of steam methane reforming as the the hydrogen source instead of coal gasification, the use of turbine pumps instead of traditional reciprocating pumps, improvement of heat integration, and the use of more durable, selective, and active catalysts. Further improvements can be made, as the theoretical minimum energy investment for ammonia synthesis with steam methane reforming is 20.9 GJ $t^{-1}_{NH_3}$. Nevertheless, the current Haber-Bosch process is already more energy efficient than natural enzymatic nitrogen fixation [23]. In the 21st century, the decarbonisation of ammonia synthesis has become an important area of focus. Carbon capture and replacing steam methane reforming with electrolysis as the H_2 source are short to medium term improvements to achieve this goal, while in the long term electrochemical ammonia synthesis might bring further efficiency gains and enable decentralisation of ammonia production.

2.2. Electrochemistry Fundamentals

Electrochemistry studies reactions involving electrons that occur at the interface between an electronic conductor and an ionic conductor. Electrons are the mobile species in the electrode, hence the electrode can be used to measure or control the potential of the electrons. Electrodes are usually metals, although other conducting materials such as carbon or intermetallic compounds can also be used. In the electrolyte ions are the mobile species. Usually the electrolyte is a salt solution, even if molten salt electrolytes are also possible. When an electrochemical reaction takes place, electrons are transferred between species in the electrode and species in the electrolyte. When a species loses an electron its oxidation state and charge increase, called oxidation. Conversely, when a species receives an electron its oxidation state decrease, called reduction. Species that easily donate electrons and are thus easily oxidised are called reductants - they facilitate reduction of another species - while species that accept electrons and are thus reduced are called oxidants - oxidising agents. Applying an negative external potential to the electrode increases the energy of the electrons. When an electron's energy exceeds the lowest unoccupied molecular orbital energy of a species in the electrolyte, this species will be reduced.

When a metal electrode is placed in an ionic conducting solution that does not contain the metal's ions, atoms from the surface of the electrode will oxidise and dissolve in the solution according to the reaction below:

$$\mathrm{M}_{red}^{(m-n)+}(\mathrm{s}) \rightleftharpoons \mathrm{M}_{ox}^{m+}(\mathrm{aq}) + n\mathrm{e}^- \tag{2.2}$$

Where $\mathrm{M}_{red}^{(m-n)+}$ denotes the reductant and M_{ox}^{m+} the oxidant with their oxidation states in superscript. The excess electrons in the electrode due to oxidation result in a net negative charge on the electrode surface and a net positive charge in the solution. The associated electrical potential difference will cause ions to spontaneously reduce and deposit back on the electrode. The oxidation and reduction reactions will tend towards an equilibrium, where the reaction rate in both directions is equal. The potential difference between the solution and the electrode at equilibrium is called the equilibrium electrode potential, $E^0 = (\Phi_m - \Phi_s)_{eq}$. This potential difference can be expressed in terms of the electrochemical potentials of the species involved in the reaction. When reaction 2.2 is in equilibrium, the electrochemical potentials of both sides of the reaction are equal, as in Equation 2.3.

$$\mu_{red} = \mu_{ox} + n\mu_e \tag{2.3}$$

It is a fact of thermodynamics that the electrochemical potential of a species is not absolute. Instead the potential is determined relative to an arbitrary potential value at a set of reference conditions, expressed as μ_i^0 for pure species i. Now the electrochemical potential μ_i is dependent on the natural logarithm of the activity of i according to Equation 2.4. An additional term includes the contribution of the electric potential field to the electrochemical potential of charged species.

$$\mu_i = \mu_i^0 + RT\ \ln(a_i) + z_i F\Phi \tag{2.4}$$

Here R is the universal gas constant, T is the temperature, and a_i the activity, which is well approximated by the molar concentration of c_i if the solution is ideal, as discussed in subsection 2.2.1. z_i is the charge number of the species i, F is the Faraday constant or the charge in one mole of elementary charge carriers in $\mathrm{C\,mol^{-1}}$, and Φ the electric potential. Substituting Equation 2.4 into Equation 2.3 for each of the involved species yields:

$$\mu_{red}^0 + RT\ln(a_{red}) + (m-n)F\Phi_s = \mu_{ox}^0 + RT\ln(a_{ox}) + mF\Phi_s + n\mu_e^0 - nF\Phi_m \tag{2.5}$$

Here z_i were replaces by the charge numbers from Equation 2.2. This equation can be rearranged to solve for the electric potential difference between the solution and the metal, giving the equilibrium electrode potential expressed in the electrochemical potentials of the involved species, as given in Equation 2.6.

$$E_{eq} = \Phi_m - \Phi_s = \frac{\mu^0_{ox} - \mu^0_{red} + n\mu^0_e}{nF} + \frac{RT}{nF} \ln\left(\frac{a_{ox}}{a_{red}}\right) = E^0 + \frac{RT}{nF} \ln Q \tag{2.6}$$

Equation 2.6 is known as the Nernst equation for a half-cell. The term in which the electrochemical potentials are aggregated is collapsed into E^0, the equilibrium electrode potential at standard conditions or standard electrode potential. Standard conditions are a temperature of 298.15 °K, pressure of 1 bar and unit activity for all species. At these conditions the logarithm in Equation 2.6 will be 0. Q is the reaction quotient, given by the fraction of the activities of the reductant and the oxidant, $Q = \frac{a_{red}}{a_{ox}} \approx \frac{c_{red}}{c_{ox}}$.

The above derivation pertains to a half-cell, and the same steps can be taken for a cell with two electrodes connected electrically by a wire and ionically by an electrolyte. If no current is flowing between the electrodes, the cell potential is related to the difference in electrochemical potential of the electrons in the anode and cathode.

$$E = \frac{\mu^c_e - \mu^a_e}{F} \tag{2.7}$$

Expressing the electrochemical potentials of the electrons in Equation 2.7 in terms of the species participating in the redox reactions that take place at each electrode yields an equation similar to Equation 2.6 for the two electrode cell. The cell potential is the Gibbs free energy change per coulomb of charge passing through the cell, is displayed in Equation 2.8. This identity allows the Nernst equation to be expressed in Gibbs free energy changes for the cell reaction, as shown in Equation 2.9.

$$\Delta G = -nFE \tag{2.8}$$

$$\Delta G = \Delta G^0 - RT \ln Q \tag{2.9}$$

A negative cell potential indicates the reaction is not spontaneous, making it an electrolytic cell. In contrast, a galvanic cell has a positive cell potential resulting in a spontaneous reaction. When an external power source provides a potential to an electrolytic cell equal to or above the equilibrium cell potential, energy is consumed and stored in the cell. Driving the electrolytic cell at equilibrium potential gives a reversible reaction at negligible current, and an overpotential (subsection 2.2.3) has to be applied to drive significant current flow due to irreversibilities in the reactions. In general, the electrochemical reaction in an electrolytic cell driven at equilibrium voltage at standard conditions will be endothermic, extracting heat from the environment to sustain the reaction. The total energy required for the reaction including possible heat extracted from the environment is the difference in enthalpy ΔH between the reactants and products, which differs from ΔG by the entropic term $T\Delta S$. $T\Delta S$ represents the thermodynamic irreversibility, or the heat demand in the case of a reversible reaction. The voltage that corresponds exactly to the enthalpy difference, and thus marks the point were the reaction is neither endothermic nor exothermic, is called the thermoneutral voltage, given by Equation 2.10.

$$E^0_{th} = \frac{\Delta H_{red} - \Delta H_{ox}}{nF} \tag{2.10}$$

Of course these energetic quantities are dependent on the conditions, so for example an increase in temperature might lead to a decrease in the equilibrium voltage. Figure 2.3 shows the different potential regions for the hydrogen and oxygen evolution redox couple, and their dependence on temperature.

2.2.1. Activity

Chemical activity is a dimensionless quantity that indicates the deviation from the standard chemical potential of a species, according to the relationship shown earlier in a different form in Equation 2.4. The activity is unity in the standard state for the species, where the chemical potential equals the standard chemical potential. The activity of pure solids and liquids is usually taken as unity.

$$a_i = e^{\frac{\mu_i - \mu^0_i}{RT}} \tag{2.11}$$

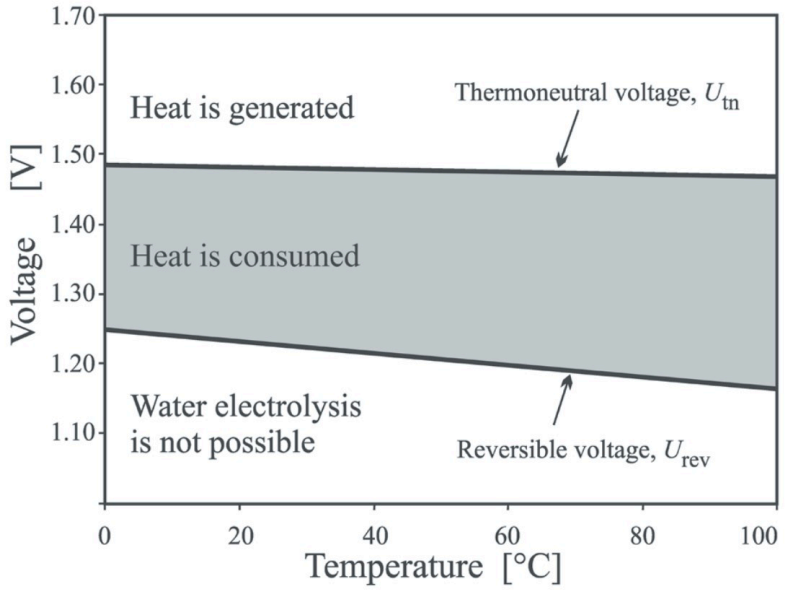

Figure 2.3: Temperature dependence of the equilibrium voltage and thermoneutral voltage of a water electrolysis cell. Image reproduced from [26].

To clarify the relationship between activity and concentration, ideal solutions have to be defined. Ideal solutions are thermodynamically analogous to ideal gases. Instead of the negligible interaction strength between molecules in ideal gases, ideal solutions are defined by equal mean interaction strength between all constituents of the solution. Ideality results in a zero enthalpy of mixing, because the interaction energy of component A with itself is the same as that of component A with component B and of component B with itself, meaning no change in overall energy upon mixing. Ideal solutions obey Henry's law, which states that the amount of dissolved gas in a liquid is proportional to the partial pressure above the liquid, and Raoult's law, which states that partial pressures in a mixture are equal to the vapour pressure of the individual components multiplied by their mole fraction in the mixture.

The chemical potential of a species in a real mixture depends on the activity in the same way as it depends on the concentration for an ideal solution. In this sense the activity measures the effective concentration, incorporating deviations from ideal behaviour caused by interactions between components of the solution. Activity can be related to molar concentration through the dimensionless activity coefficient γ_i:

$$a_i = \gamma_i \frac{c_i}{c^0} \tag{2.12}$$

where c_i is the molar concentration and c_0 is the standard molar concentration, usually $1\,\mathrm{mol\,L^{-1}}$. Furthermore, an absolute activity can be defined that is zero when the species is absent.

$$\lambda_i = e^{\frac{\mu_i}{RT}} \tag{2.13}$$

The actual activity is calculated by dividing the absolute activity by the absolute activity at standard conditions, $a_i = \frac{\lambda_i}{\lambda_i^0}$.

In the same way that activity is the effective concentration for species in a mixture, the fugacity f measures the effective partial pressure for gases incorporating non-ideal behaviours. It is defined by the real gas pressure multiplied by a fugacity coefficient φ. For ideal gases the fugacity coefficient is unity.

2.2.2. Electric Double Layer

The charge distribution near an electrode is usually not uniform and neutral. One species of charged ion, for example hydroxide, might be more likely to approach the electrode's surface than another, for example sodium. This could be due to excess charge on the electrode, and also due to the ion's own tendency to move toward a neutral electrode. When hydroxide is more likely to approach the electrode, a layer with slightly negative charge is formed directly outside the electrode. A layer with slightly positive charge from the excess of sodium ions follows after the negatively charged layer. The sodium ions are attracted to the negative charge of the excess hydroxide ions, forming a stable Electric Double Layer (EDL). An EDL can also form with molecules that have an electric dipole, when one side of the molecule is more likely to bind to the electrode's surface.

Microscopically the EDL consists of four regions. The Inner Helmholtz Plane (IHP) is located about 0.2 nm from the electrode surface, this is where adsorbed molecules or ions are located. Beyond the IHP lies the Outer Helmholtz Plane (OHP), at the closest distance solvated ions or molecules will move toward the electrode surface. After the OHP lies the diffuse layer, with a net charge but presence of both anions and cations. The outer limit of the diffuse layer is located between 1 nm to 10 nm from the electrode surface. Between the bulk electrolyte and the diffuse layer there is a diffusion layer, which is neutrally charged while still containing concentration gradients. A schematic of the EDL structure is given in Figure 2.4

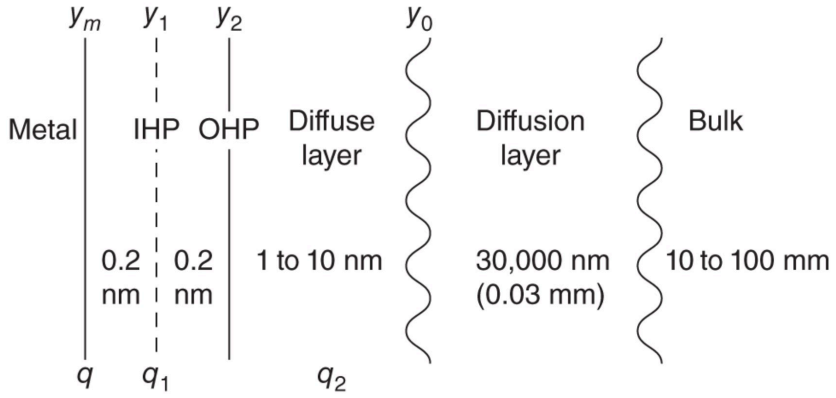

Figure 2.4: Schematic representation of the EDL, showing the IHP (adsorbed species), OHP (closest approach distance of solvated species), diffuse layer (electric potential gradient), diffusion layer (concentration gradient), and bulk electrolyte. Image reproduced from [27].

The charge that accumulates in the IHP upon applying a potential to an electrode is proportional to the applied voltage in non-faradaic conditions. This means the EDL functions as a parallel plate capacitor in the potential range where no net reaction is occurring. The IHP can be viewed as the dielectric layer. The definition of capacitance is given in Equation 2.14.

$$C = \frac{q}{U} \tag{2.14}$$

Here, C is the capacitance in farad, q is the stored charge in coulomb and U the applied potential between the capacitor surfaces. Differentiating Equation 2.14 with respect to time yields a relationship between the EDL (dis)charge current I and the rate of change of the applied potential, with the double layer capacitance C as the slope, namely $I = C\frac{dU}{dt}$. The capacitance of the double layer can thus be determined by imposing different rates of potential change to on the electrode and measuring the resultant EDL (dis)charge currents, and taking the slope of this relationship.

C depends on the specific combination of electrode material and electrolyte species, which governs the amount of species that can enter the IHP and their charge. Assuming this combination to be constant, the capacitance is a measure for the electrode area available for charge storage or electrochemical reactions in general, known as the Electrochemical Active Surface Area (ECSA). The ECSA may be greater than the geometric surface area due to the surface morphology, such as cervices, peaks, or porous structures. Thus, C can be used to determine the ECSA of a surface morphology compared to a perfectly flat morphology of the same material. It may be convenient to express I and C in an area specific manner, as in Equation 2.15, where v denotes the rate of change of the applied potential.

$$i = c_{dl}\frac{dU}{dt} = c_{dl}v \tag{2.15}$$

2.2.3. Electrode Kinetics

The reaction rate of an electrode reaction depends mainly on the composition of the electrode surface and electrolyte, temperature, and previous treatment of the electrode. When an electrode reaction is occurring in steady state, the reaction rate is directly coupled to to passage of current through the electrode by Faraday's law. The potential difference between electrode A that is driven by an external potential and an identical electrode B in the same electrolyte placed just outside the electric double layer of electrode A is known as the overpotential. It can be thought of as the electrochemical potential of the electrons in the driven electrode compared to the electrochemical potentials of the other species in the reaction, showing a departure from equilibrium condition in Equation 2.3. The difference in electrochemical potential on both sides of the equilibrium condition is related to the overpotential η in Equation 2.16 through F and the number of electrons transferred in the reaction n. In general the number of species participating in the electrode reaction can exceed two, and stoichiometric constants should be included in the equation accordingly.

$$\frac{-n\mu_e + \mu_{red} - \mu_{ox}}{nF} = \eta \tag{2.16}$$

Revisiting Equation 2.2, it is noted that the anodic and cathodic reactions on the electrode occur independently, and net reaction rate is equal to the difference in the forward and backward reaction rates. The reactions are first order in the reactants. The reaction rates are comprised of Arrhenius rate constants k_a and k_c for the anodic and cathodic reactions respectively that depend on temperature and the activation energy, multiplied by an exponential factor that depends on the applied potential U.

$$r = k_a c_{red}\text{exp}\left[\frac{(1-\beta)nF}{RT}U\right] - k_c c_{ox}\text{exp}\left[\frac{(-\beta)nF}{RT}U\right] \tag{2.17}$$

In this equation c_{red} and c_{ox} are the concentrations of the reactants and β is known as the symmetry factor. β determines the fraction of the applied potential that promotes or inhibits the cathodic reaction. This can be seen by combining the potential dependent exponential factor and the reaction rate constant k_c into a single Arrhenius rate constant:

$$k_c\text{exp}\left[\frac{(1-\beta)nF}{RT}U\right] = A_c\text{exp}\left[\frac{-E_{a,c}}{RT}\right]\text{exp}\left[\frac{(1-\beta)nF}{RT}U\right] = A_c\text{exp}\left[\frac{-(E_{a,c}+\beta nFU)}{RT}\right] \tag{2.18}$$

Above, k_c is decomposed into its frequency factor term A_c and an exponential term based on the activation energy $E_{a,c}$. The potential increase of ΔU corresponds to an increase in effective activation energy for the cathodic reaction by $\beta nF\Delta U$. The same increase in potential shifts the effective activation energy of the anodic reaction down by $(1-\beta)nF\Delta U$.

In equilibrium, $U = E^0$ and the cathodic and anodic reactions have equal rates:

$$k_a c_{red}\left[\frac{(1-\beta)nF}{RT}E^0\right] = k_c c_{ox}\text{exp}\left[\frac{-\beta nF}{RT}E^0\right] \tag{2.19}$$

Rearranging this equation to solve for E_0 gives a different form of the Nernst equation, Equation 2.20:

$$E^0 = \frac{RT}{nF} \ln\left(\frac{k_c c_{ox}}{k_a c_{red}}\right) \tag{2.20}$$

The overpotential is given by the difference between E^0 and applied potential U, $\eta = U - E^0$. Now Equation 2.17 can be rewritten using η:

$$r = k_a c_{red} \exp\left[\frac{(1-\beta)nF}{RT}(\eta + E^0)\right] - k_c c_{ox} \exp\left[\frac{-\beta nF}{RT}(\eta + E^0)\right] \tag{2.21}$$

$$= k_a c_{red} \exp\left[\frac{(1-\beta)nF}{RT}\eta + (1-\beta)\ln\frac{k_c c_{ox}}{k_a c_{red}}\right] - k_c c_{ox} \exp\left[\frac{-\beta nF}{RT}\eta - \beta \ln\frac{k_c c_{ox}}{k_a c_{red}}\right] \tag{2.22}$$

Here the second terms in the exponents can combine with the rate constants and concentrations in front of the exponents to form the same prefactor for both exponential terms. Expressing the equation in terms of current density using the identity in Equation 2.23 gives Equation 2.24 were i_0 is that shared prefactor.

$$\frac{r}{nF} = i \quad i_0 = nF k_a^{\beta} k_c^{1-\beta} c_{red}^{\beta} c_{ox}^{1-\beta} \tag{2.23}$$

$$i = i_0 \left[\exp\left[\frac{(1-\beta)nF}{RT}\eta\right] - k_c c_{ox} \exp\left[\frac{(-\beta)nF}{RT}\eta\right]\right] \quad \text{where} \quad i_0 = nF k_a^{\beta} k_c^{1-\beta} c_{red}^{\beta} c_{ox}^{1-\beta} \tag{2.24}$$

This equation is known as the Butler-Volmer equation, incorporating properties of the electrode surface, electrolyte and temperature to relate the overpotential to the reaction current density. The exchange current density is the reaction rate constant of both directions when the reaction is in equilibrium. This means that a high exchange current density indicates a facile reaction that will display a high current for relatively small overpotentials.

In reality electrode reactions have numerous additional complexities compared to this model. For example, most electrode reactions are made up of multiple elementary steps, where intermediates are formed. These intermediates can be unstable and hence difficult to detect, and the rates of the elementary steps can differ across the reaction mechanism. The net reaction rate of the macroscopic reaction can be modelled by a set of coupled differential equations. The reaction rate constants and activation energies of elementary steps can be determined experimentally or predicted through computer modelling.

2.3. Electrochemical Ammonia Synthesis

This section applies the electrochemistry fundamentals discussed above to the Nitrogen Reduction Reaction (NRR). The treated subjects are applicable to most forms of electrochemical ammonia synthesis, especially using aqueous electrolytes. The next section 2.4 specialises these concepts further towards the application with hydrogen permeable electrodes.

The half reactions for NRR in acidic and alkaline environments respectively are given by the reactions below:

$$\mathrm{N_2(g) + 6\,H^+(aq) + 6\,e^- \rightleftharpoons 2\,NH_3(aq)} \qquad E^0 = 0.092\,V_{RHE} \tag{2.25}$$

$$\mathrm{N_2(g) + 6\,H_2O(l) + 6\,e^- \rightleftharpoons 2\,NH_3(aq) + 6\,OH^-(aq)} \qquad E^0 = 0.092\,V_{RHE} \tag{2.26}$$

Their equilibrium potentials are slightly above the equilibrium of the hydrogen evolution reaction, indicating that NRR is thermodynamically more favourable than Hydrogen Evolution Reaction (HER) at room temperature and pressure. The thermoneutral voltage of NRR coupled with Oxygen Evolution Reaction (OER) as the anodic reaction calculated using Equation 2.10 is 1.32 V, which is also also lower than the 1.48 V of HER coupled with OER. The HER equations in acidic and alkaline media are respectively:

$$2\,H^+\,(aq) + 2\,e^- \rightleftharpoons H_2(g) \qquad E^0 = 0.000\,V_{RHE} \tag{2.27}$$

$$2\,H_2O\,(l) + 2\,e^- \rightleftharpoons H_2(g) + 2\,OH^-(aq) \qquad E^0 = 0.000\,V_{RHE} \tag{2.28}$$

The Pourbaix diagram of N_2 dissolved in water in Figure 2.5 shows the stability regions for species and phases depending on the solution's pH and applied potential. The orange region is the region where reduction of N_2 to NH_3 and NH_4^+ should thermodynamically occur without HER competition.

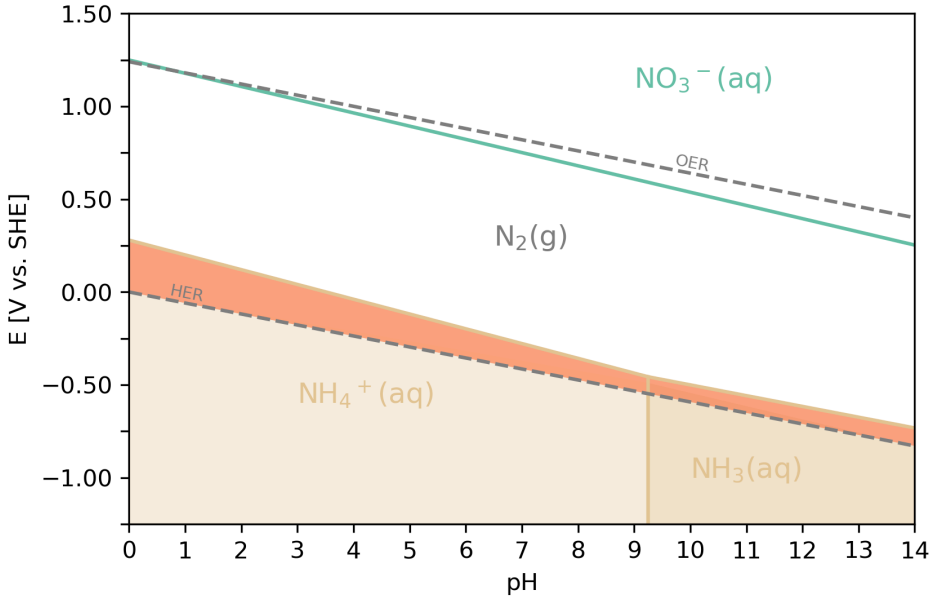

Figure 2.5: Pourbaix diagram of nitrogen dissolved in water at 25 °C and atmospheric pressure, showing that in alkaline environments ammonia is the thermodynamically favoured species in a region above the lower hydrogen stability line. This indicates that in this region nitrogen reduction could take place without competition from HER.

It is clear that nitrogen reduction is theoretically possible at room temperature and pressure. This thermodynamic favourability exists up to temperatures of 200 °C, above which the thermodynamic potential of NRR exceeds water electrolysis. Yet even below 200 °C, there are numerous factors that make direct nitrogen reduction far from a facile process, despite apparent the thermodynamic favourability. For example, three H atoms must be reduced to produce one ammonia molecule, while only two are needed for hydrogen gas. In fact, the associative reaction pathways displayed in Figure 2.6 that are most common in NRR require 6 electron transfers per reaction cycle, compared with two for HER. Furthermore, some elementary reactions in the nitrogen reduction reaction mechanism, notably the hydrogenations, are highly endergonic, meaning they entail a positive Gibbs free energy change. Hence, these reactions have a more negative equilibrium potential than what is implied by the equilibrium potential of the full reaction [28]. One such hydrogenation reaction is the reduction of N_2 (g) and H^+ to N_2H (g), with an equilibrium potential of $-3.2\,V_{RHE}$ [29]. Without a catalyst to stabilise such intermediates, the energy barriers for N_2 reduction are significantly higher than what Figure 2.5 implies. Well-designed catalysts can reduce these barriers.

It is important to realise that endergonic elementary steps can be surmounted by applying a potential bias only if they involve electron transfer. In that case, the electrons are given the free energy required for the elementary reaction by the applied potential, making the overall elementary step downhill in free energy. The free energy change of the elementary step is modified by the applied potential E according to Equation 2.29, which resembles the Nernst equation.

$$\Delta G(E) = \Delta G(0) - neE \tag{2.29}$$

However, if no electron transfer is involved, applying a potential will not change the net free energy, and a change in temperature or pressure is needed to surmount such uphill elementary steps. The adsorption of nitrogen and desorption of ammonia on the catalysts surface are examples of elementary steps without electron transfer. The most endergonic electrochemical elementary step is referred to as the Potential Determining Step (PDS), while the most endergonic non-electrochemical elementary step is referred to as the Rate Determining Step (RDS).

Nitrogen is an especially stable molecule, for which there are numerous reasons. To split N_2, a binding energy of 945 kJ mol^{-1} has to be overcome, which is relatively high. This becomes even more significant when the energy of the first of the triple bond is considered, at 410 kJ mol^{-1} this is nearly half the total bond energy that has to be overcome in the first bond cleavage [30]. Its proton affinity, or the Gibbs free energy released upon combining with a proton is low at 543.5 kJ mol^{-1} and the electron affinity is negative (−1.90 eV) meaning direct reduction is hindered. Further hampering electron transferring reactions is the large gap the Highest Occupied Molecular Orbital (HOMO) and the Lowest Unoccupied Molecular Orbital (LUMO) [31]. These factors make activation of N_2 difficult at mild conditions.

2.3.1. Ammonia Synthesis Reaction Mechanisms

Heterogeneous ammonia synthesis is generally believed to take place according to one of four classes of mechanisms, displayed in Figure 2.6 and Figure 2.8. In the dissociative pathway, N_2 molecules are first split into individual N atoms that are adsorbed to the catalyst surface (dissociative adsorption). These adsorbed N atoms are them triply hydrogenated to form NH_3. This mechanism is dominant in the Haber-Bosch process, where the extreme conditions allow direct cleaving of the triple bond. Conversely, in associative pathways, N_2 molecules are initially adsorbed without completely breaking the triple bond. Instead, step-wise cleavage of the triple bond takes place during the hydrogenation steps. In the alternating associative pathway the N atoms are hydrogenated alternatingly and two ammonia molecules are released successively. On the other hand, in the distal associative pathway the outer N atom is fully hydrogenated and released as ammonia before the hydrogenation of the second N atoms starts.

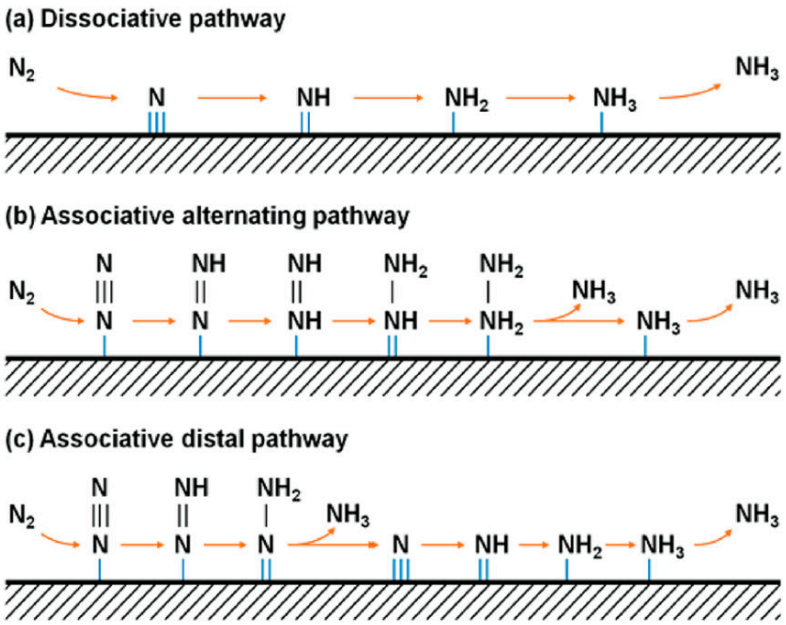

Figure 2.6: Schematic representation of the three main reaction mechanisms for heterogeneous ammonia synthesis. Image reproduced from [32].

The elementary steps for the associative distal reaction mechanism are given in Equation 2.30, in which empty adsorption sites are written as *, and adsorbed species as A*.

$$
\begin{aligned}
N_2(g) + {}^* &\rightleftharpoons N_2{}^* \\
N_2{}^* + H^* &\rightleftharpoons N_2H^* + {}^* \\
N_2H^* + H^* &\rightleftharpoons N_2H_2{}^* + {}^* \\
N_2H_2{}^{*+}H^* &\rightleftharpoons N_2H_3{}^* + {}^* \\
N_2H_3{}^* &\rightleftharpoons N^* + NH_3(g) \\
N^* + H^* &\rightleftharpoons N_2H^* + {}^* \\
NH^* + H^* &\rightleftharpoons N_2H_2{}^* + {}^* \\
NH_2{}^* + H^* &\rightleftharpoons N_2H_3{}^* + {}^* \\
NH_3{}^* &\rightleftharpoons NH_3(g) + {}^*
\end{aligned}
\tag{2.30}
$$

Intermediates present during the associative mechanisms are N_2*, N*, NH*, NH_2*, NH_3*, N_2H*, N_2H_2*, N_2H_3*, and N_2H_4*. An ideal catalyst would strongly bind and stabilise N_2H*, allowing the first steps of the associative mechanisms to take place without substantial free energy expenditure, while at the same time weakly binding NH_2* so that its reaction to desorbed NH_3 would be promoted. In actual fact, because all intermediates are adsorbed to the catalyst's surface with the N atom, the binding energies of most of these intermediates are linearly correlated to the N* binding energy of the catalyst [33]. These correlations are called scaling relations, and allow for calculating the potential determining step (the most energetically uphill electrochemical step) when the binding energy of N* and its scaling relations with the other intermediates are known. The scaling relations dictate that an optimal binding of N_2H* causes overbinding of NH_2*, and a theoretical optimum of the N binding energy for ammonia synthesis exists. Figure 2.7 shows the minimum potential needed to overcome the potential determining step plotted against the N* binding energy for a series of metals. This 'volcano' plot owes its name to the peak in the centre, where the metals bind N not to weakly nor to strongly. The lowest overpotential in the figure is 0.4 V, and iron, rhodium, and ruthenium appear to be the optimal catalysts.

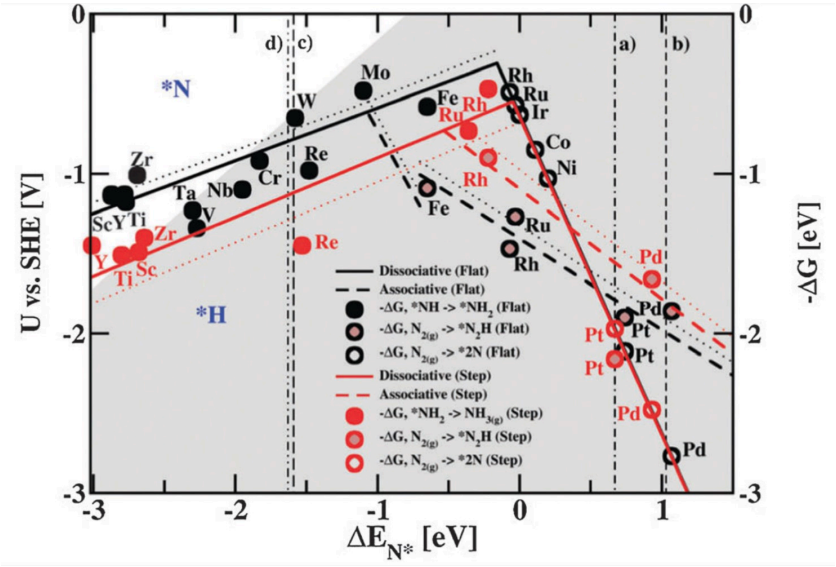

Figure 2.7: Volcano plot of the NRR on different metals. The y-axis shows the potential needed to overcome the electrochemical step with the most positive free energy change. The x axis is the N* binding strength of the metal. A distinction is made between flat and stepped surfaces, and the circles indicate which elementary reaction is the potential determining step for the metal, as shown in the legend. The grey area indicates where H* adsorption is preferred over N* adsorption, which could cause HER competition. Image reproduced from [33].

The fourth class of mechanisms is called Mars-van Krevelen (MvK) mechanisms or regenerative mechanisms, schematically depicted in Figure 2.8. This is a class of mechanisms defined by the consumption of constituents of the catalyst's lattice in the product [34]. The resulting vacancy is subsequently replenished by adsorption of the catalyst, reinstating the lattice. In ammonia synthesis with an MvK mechanism, the catalyst atom leaving the surface in the product molecule is nitrogen, and hence this mechanism involves a metal catalyst with a layer of metal-nitride on its surface. The MvK mechanism was first discovered in a study of the reaction kinetics of the oxidation of SO_4, and is most established for oxide-catalysed reactions, while other elements, such as chlorides, hydrides, and nitrides, can also enable the mechanism [35].

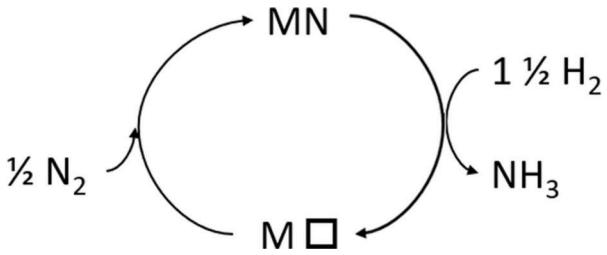

Figure 2.8: Schematic representation of ammonia synthesis via an MvK mechanism. The cyclic nature is evident from a lattice nitrogen being incorporated in the product, followed by replenishment of the resultant vacancy, which is marked by □. Image reproduced from [36].

The elementary steps in the MvK mechanism are given in Equation 2.31. A vacancy for an adsorbed species is again marked with *, while the N vacancies in the metal lattice are marked with □. The displayed steps form the associative MvK variant, in which a single N vacancy is replenished by a nitrogen molecule without cleavage of the triple bond, leaving one atom adsorbed on top of the MN site that is to be hydrogenated to NH_3 to complete the cycle. A dissociative variant is also possible, in which a dimer vacancy consisting of two neighbouring N vacancies is replenished by a single N_2 molecule, cleaving the triple bond. The associative variant seems most favoured for NRR using Ni_3N [36] [37] [38].

$$
\begin{aligned}
\mathrm{MN} + \mathrm{H}^* &\rightleftharpoons \mathrm{MNH} + {}^* \\
\mathrm{MNH} + \mathrm{H}^* &\rightleftharpoons \mathrm{MNH_2} + {}^* \\
\mathrm{MNH_2} + \mathrm{H}^* &\rightleftharpoons \mathrm{MNH_3} + {}^* \\
\mathrm{MNH_3} &\rightleftharpoons \mathrm{M\square} + \mathrm{NH_3(g)} \\
\mathrm{M\square} + \mathrm{N_2(g)} &\rightleftharpoons \mathrm{MN{-}N}^* \\
\mathrm{MN{-}N}^* + \mathrm{H}^* &\rightleftharpoons \mathrm{MN{-}NH}^* + {}^* \\
\mathrm{MN{-}NH}^* + \mathrm{H}^* &\rightleftharpoons \mathrm{MN{-}NH_2}^* + {}^* \\
\mathrm{MN{-}NH_2}^* + \mathrm{H}^* &\rightleftharpoons \mathrm{MN{-}NH_3}^* + {}^* \\
\mathrm{MN{-}NH_3}^* &\rightleftharpoons \mathrm{MN} + \mathrm{NH_3(g)}
\end{aligned}
\tag{2.31}
$$

The MvK mechanism has additional degrees of freedom compared to other mechanisms. Both, one or none of the N atoms can be incorporated into the lattice upon adsorption, each of these exchange modes is characterised by a different reaction rate [35]. It is expected that a correlation exists between the Metal - Nitride bond strength and the catalytic reaction rate [35].

The fact that metal nitrides are consumed in the catalytic cycle implies that the resulting vacancies have to be regenerated through adsorption of N_2, otherwise the cycle will eventually come to a halt when all surface nitrides have been converted to ammonia, and a bare metal catalyst remains. Metal nitrides for which replenishment of vacancies is slower than consumption of N through ammonia synthesis might thus be considered reactants rather than catalysts. Nitride vacancies are known to be able to migrate into the bulk metal, precluding them from being regenerated through nitrogen adsorption. Both bulk migration and N adsorption are reactions with activation energies, and it is expected that the reaction with lower activation energy will prevail over time, leading to either deactivation or continuation of the catalytic cycle. These activation energies are a property of the metal-nitride, with various metals showing lower activation energy for vacancy migration than for N adsorption [38], indicating that experiments with a range of metals might be necessary.

2.3.2. Cell Types

Electrochemical ammonia synthesis at mild conditions is most commonly conducted using aqueous electrolytes. In this class of synthesis cell there are three notable varieties, namely a simple cell without a membrane, an H-type cell with an ion conducting membrane, and a zero-gap Gas Diffusion Electrode (GDE) cell design wherein the electrolyte and the nitrogen gas approach the working electrode from opposite sides. This design overcomes mass transfer limitations of the first two, by circumventing dissolution of N_2 in the electrolyte. The solubility limit of N_2 in water is 0.71mM at 25 °C and atmospheric pressure, with an Ostwald coefficient L_v^0 of $1.274 \cdot 10^{-5}$ [39]. Here $L_v^0 = V_g/V_l$, the dissolved gas volume divided by the liquid volume without gas. This is low solubility promotes the competition of HER due to H atoms being more readily available at the working electrode than N atoms in the cell types without GDEs. The three cell variants are shown in figure Figure 2.9.

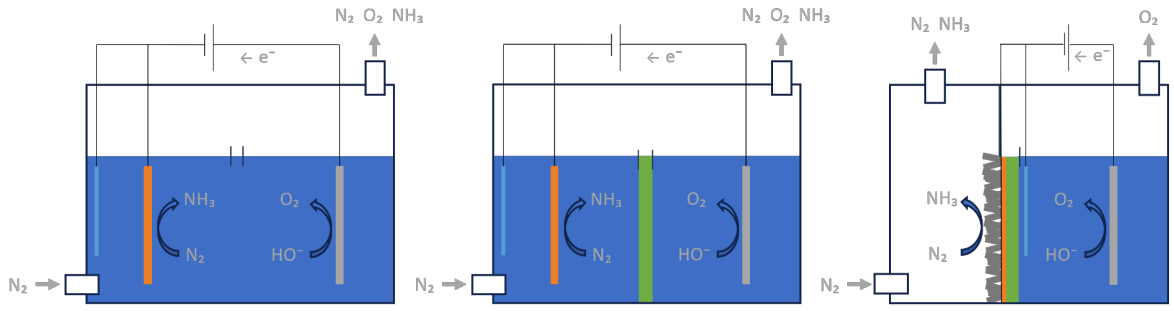

Figure 2.9: Schematics of the three most common NRR cell types. The working electrodes are presented in orange, the counter electrode in grey, the reference electrodes in light blue, and the ion conducting membrane in green. Left: H-type cell without anion exchange membrane. Middle: H-type cell with anion exchange membrane. Right: Cell with a gas diffusion electrode.

This research is focused on an unconventional cell type, namely a cell with a Hydrogen Permeable Electrode (HPE). In this design the working electrode is a metal foil through which H atoms can permeate from an electrolyte compartment to a gas compartment on the other side of the foil. The intent of the design is to separate the competing HER and NRR reactions physically, preventing mass transfer limitations and poisoning of the catalyst with hydrogen. A schematic representation of an HPE cell is given in Figure 2.10. The schematic shows that H_2 will be formed upon recombination of adsorbed H atoms on both sides of the HPE. These side reactions that be minimised. Furthermore, the schematic is made to resemble the lab scale cell used in this research, which does not feature an anion exchange membrane for O_2 and H_2 separation in the electrolyte compartment, or a reference electrode.

2.3.3. Surface Reactions in Alkaline Aqueous Electrolyte

An aqueous electrolyte-electrode interface differs from a gas-metal interface in that H-adsorption always requires the displacement of adsorbed water molecules or ions, and dissociation of H_2 can happen both chemically and electrochemically. Chemical dissociative adsorption of gaseous H_2 involves the dissolution of hydrogen gas in the electrolyte, transport to the metal surface and the dissociative adsorption reaction:

$$H_2(aq) + 2\,(M) \rightleftharpoons 2\,H^*M \tag{2.32}$$

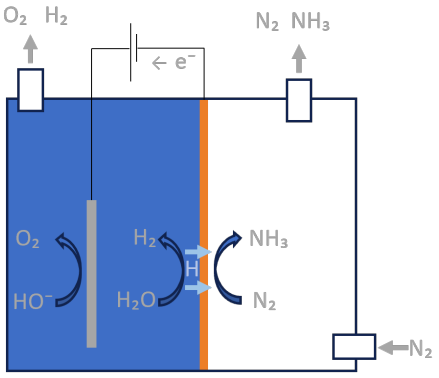

Figure 2.10: Schematic representation of an HPE cell. The working electrode is a metal foil that separates the electrolyte and gas compartments. Hydrogen atoms diffuse through the working electrode and hydrogenate adsorbed N atoms to ammonia on the other side.

2 (M) is a pair of hydrated sites available for adsorption, and H*M is a complex of a hydrogen atom adsorbed on a site M. The reaction may occur directly when two sites are available next to each other, or a physisorbed H_2 molecule may migrate on the surface until available sites are found. The reverse of this reaction is associative recombination, also known as the Tafel reaction.

The potential of the electrode can also be used to drive two electrochemical dissociative adsorption mechanisms, namely the Volmer and Heyrovsky reaction. In alkaline electrolytes the Volmer reaction involves the dissociation of a water molecule into a proton and an hydroxide ion, and subsequent reduction and adsorption of the proton into an available site. The reaction equation is given in Equation 2.33

$$H_2O(l) + e^- + (M) \rightleftharpoons H^*M + OH^-(aq) \tag{2.33}$$

An adsorbed hydrogen atom can be desorbed either chemically by the Tafel reaction, or through electrochemical combination with a water molecule in the Heyrovsky reaction given in Equation 2.34:

$$H^*(M) + H_2O(l) + e^- \rightleftharpoons H_2(aq) + OH^-(aq) + (M) \tag{2.34}$$

Based on these elementary steps, the two overall reaction mechanisms for the hydrogen evolution reaction are the Volmer-Tafel pathway and the Volmer-Heyrovsky pathway.

Impeding HER with hydrostatic pressure overpotential

The Nernst equation for the HER in alkaline media shown in Equation 2.28 is given below:

$$E = E^0 - \frac{RT}{nF} \ln \frac{[OH^-]^2[H_2]}{[H_2O]} = E^0 - \frac{RT}{nF} \ln \frac{[OH^-]^2 \frac{p_{H_2}}{p_0}}{1} \tag{2.35}$$

The activity of condensed species is 1, and the activity of a gas is (assuming ideal gas behaviour) the partial pressure of the gas p_{H_2} divided by standard pressure p_0. It is evident that raising the hydrostatic pressure in the cell from standard pressure makes E more negative by an overpotential of $\frac{RT}{nF} \ln \frac{p_{H_2}}{p_0}$ V or 8.8 mV for every doubling of the hydrostatic pressure. This overpotential corresponds to the energy required to compress the product gas from p_0 to p_{H_2}, since this is the pressure that has to be overcome for H_2 bubbles to form. This inhibition of the recombination reaction causes a greater tendency of hydrogen to be absorbed into the metal lattice. Increasing the pressure is thus a method to impede the HER while not affecting NRR in an HPE cell.

2.3.4. Pathways to Improving Catalytic Performance

The improvement of NH_3 production rate and faradaic efficiency of the NRR hinge on the development of catalysts that offer greater stability, activity, and selectivity than what has been achieved up to now. While the scaling relations are useful in predicting the activity of a material, the optimum that is suggested by the volcano plot is not necessarily the best achievable compromise. There exist strategies that break down the scaling relations, promoting one of the elementary reactions while not affecting the other [40]. Materials that break scaling relations often involve some form of alloying that expressly keeps the benefits from both elements. This section discusses catalysts enhancement strategies for NRR and their applicability to HPEs.

Single-atom doping

Depositing singe atoms of a different element onto a metal surface can enhance the activity by creating regions on the surface with varying N binding strengths [41]. If for example the host metal binds N more weakly than the dopant, the presence of the dopant can increase the rate of N_2 adsorption, and the adsorbed nitrogen atoms can migrate to the bulk metal to be hydrogenated and desorbed. Evidently such a catalyst can break the scaling relations between adsorption and hydrogenation, and this principle could likely be applied to an HPE. The geometric spacing between the dopant is of great importance for the performance of this type of catalyst.

Morphology engineering

The morphology of a heterogeneous catalysts directly affects the performance. For example, adding porosity to the surface can increase reactivity by increasing the proportion of low-coordinated atoms that provide more activity. The nanostructures that are used for this purpose can be hollow, or a solid structure consisting of dendrites or pillars. Defects as a result of morphology engineering can exhibit different binding strength for nitrogen, as do different facets of the same metal [42].

2.4. Ammonia Synthesis Using Hydrogen Permeable Electrodes

As section 2.3 demonstrates, electrochemical ammonia synthesis is faced with a number of major challenges that have to be overcome if the process is to become viable. Principal among these are low selectivity caused by the competition of HER, mass transport limitations of N_2 in the electrolyte, and low activity caused by the scaling relations that mutually exclude facile adsorption of N_2 and desorption of NH_3, among other reasons. Alternative approaches such as lithium-mediated and enzymatic NH_3 synthesis offer higher selectivities and rates, albeit at the cost of energy efficiency to the degree that these concepts are also not viable yet [8]. The hydrogen permeable electrode cell type is an unconventional cell design that addresses the problems to some degree, while at the same time introducing a different set of challenges. This section specifically focuses on the theory of HPE cell operation and performance. The choice of nickel as a hydrogen permeable electrode will be motivated, while also considering other options.

2.4.1. Hydrogen Diffusion in Metals

Due to its small size, the hydrogen atom is known to be able to diffuse through metals. Hydrogen molecules may physisorb onto a metal surface and dissociate, and subsequently enter the metal lattice in a process that takes place parallel to the reactions given in subsection 2.3.3. Hydrogen uptake and diffusion into the bulk is often an unwanted phenomenon because it may lead to embrittlement of the involved metals, as it accumulates at internal lattice defects. This process is known as H-embrittlement. Extremely high hydrogen pressures can be obtained in the bulk material at relatively small energy investment, making the H absorption reaction a research area of interest for hydrogen storage. Diffusion of H_2 through thin membranes can reach considerable rates, especially with highly diffusive metals such as palladium. The diffusion process generally takes place in the five steps given below:

1. Dissociation of hydrogen on the membrane surface
2. Dissolution into the bulk metal

3. Diffusion of protons through the bulk metal
4. Association of hydrogen atoms on the other side of the membrane
5. Desorption of hydrogen gas from the membrane

Diffusion to and from the gas bulk on both sides can be included as first and last steps respectively.

Entry into the metal

Hydrogen molecules are physisorbed onto metal surfaces, where dissociation happens chemically or electrochemically through the elementary steps given in Equation 2.32 and Equation 2.33. Once adsorbed, dissolution into the bulk metal happens according to

$$H^*(M)_{aq} + [M] \rightleftharpoons H_{int}[^*M] + (M)_{aq} \tag{2.36}$$

Where [M] is an empty metal site in the bulk, and H_{int}*[M] is an interstitial H atom bound to a bulk metal site. This step is usually considered to be in equilibrium, because the diffusion through the bulk [43]. The first atomic layers below the metal surface have a slightly stronger binding energy than the average bulk binding energy, and thus H bound to these sub-surface bulk sites is called H_{ss}. Figure 2.11 shows a conceptual potential diagram for H at the electrolyte-electrode interface. It shows different absorption pathways through the intermediate Underpotential H (UPH), which is the spontaneous binding state of hydrogen in the strong binding sites, and through the intermediate Overpotential H (OPH), which is on-top adsorption on weak binding sites. The UPH pathway is of less concern because this takes place at anodic potentials and is a pseudocapacitive process, meaning it will come to a halt once an equilibrium is reached. The OPH intermediate state is formed upon cathodic polarisation, and HER occurs simultaneously.

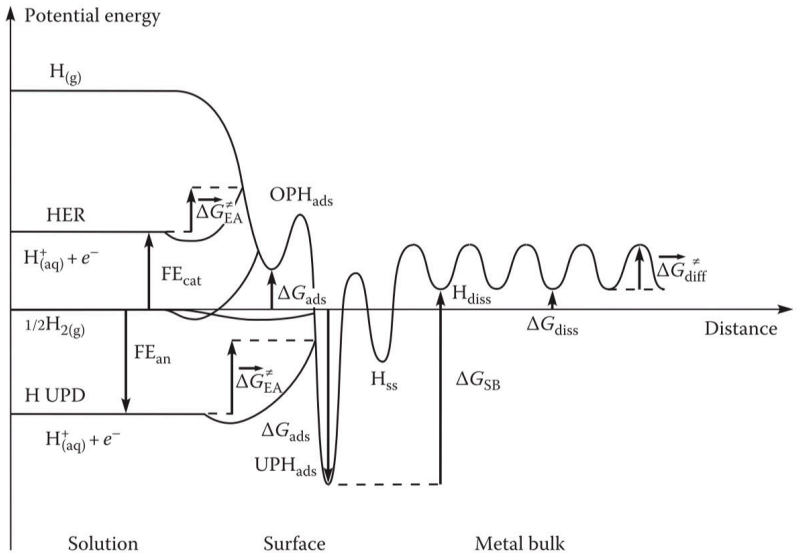

Figure 2.11: Conceptual potential diagram of H in the electroabsorption reaction. The effect of applying anodic and cathodic potential is visualised in the adsorption pathways through negative ΔG_{ads} resulting in UPH, and positive ΔG_{ads} resulting in OPH and HER. The diffusion activation energy is shown as ΔG_{diff}, and the slightly stronger bound H_{ss} resembles H absorbed in the sub-surface bulk. Image reproduced from [43].

Diffusion

In the metal lattice hydrogen is present as a proton with a delocalised electron [44]. The Fermi electrons in the metal shield the positive charge, making the proton effectively charge neutral, which is why in some literature mentions hydrogen atoms diffusing through the metal, while protons is more correct. This also means that in the case of ammonia synthesis with hydrogen permeable electrodes, the N hydrogenation steps crucially still involve participation of the delocalised electron. The crystal structure of the metal determines the type of interstitial hydrogen sites, thereby affecting the diffusivity. In Body-Centered Cubic (BCC) and Hexogonal Close-Packed (HCP) lattices hydrogen populates tetrahedral sites, as opposed to octahedral sites in Face-Centered Cubic (FCC) lattices. The high number of tetrahedral sites in BCC lattices results in a relatively short distance between nearest neighbour interstitial hydrogen sites than for FCC and HCP crystal structures [43]. This short distance results in smaller activation energies for diffusion and thus higher diffusivity.

An increase in pressure is expected to improve the permeation of hydrogen through the electrode. H_2 diffusion through dense metallic membranes follows Sieverts' law, which dictates that the solubility of diatomic gases in metals is proportional to the square root of the partial pressure of the gas in thermodynamic equilibrium [45]. Using this principle and diffusion mechanics the H_2 flux can be described by Equation 2.37.

$$N_{\mathrm{H_2}} = \frac{P}{d}(p^b_{\mathrm{H_2,entry}} - p^b_{\mathrm{H_2,perm}}) \tag{2.37}$$

The H_2 flux $N_{\mathrm{H_2}}$ depends on the hydrogen permeability coefficient of the metal P which defined as the product of the diffusivity coefficient D and solubility coefficient S the thickness of the membrane d, and the difference in partial hydrogen pressure on the entry and permeation sides of the metal. The value of the exponent b depends on the rate limiting step in the diffusion process. For membranes with a thick bulk metal layer the diffusion through the metal lattice is limiting. The diffusion rate is proportional to the concentrations of atomic hydrogen on either side of the membrane, which means proportionality to the square root of molecular H_2, and $b = 0.5$. For thin membranes the mass transfer from the bulk gas or solution to the membrane surface could be limiting, causing direct proportionality to the molecular H_2 concentration and b will approach 1 [46]. In an HPE cell the mass transport outside the membrane is not expected to be limiting because the adsorbed hydrogen is generated directly on the surface through HER.

Reporting on the hydrogen permeability of metals varies significantly, although the metal most known for its hydrogen permeability is palladium, with reported hydrogen permeabilities ranging between $1.9 \cdot 10^{-8}$ and $2.2 \cdot 10^{-7}$ $\mathrm{mol_{H_2}\,m^{-1}\,s^{-1}\,bar^{-0.5}}$ at 500 °C [47]. Nickel and iron are somewhat less permeable, both reported between $1 \cdot 10^{-7}$ and $1 \cdot 10^{-10}$ $\mathrm{mol_{H_2}\,m^{-1}\,s^{-1}\,bar^{-0.5}}$ at 500 °C [47] [48]. Still, their low cost makes nickel and iron interesting candidates for a hydrogen permeable electrode. Other elements with hydrogen permeabilities competitive with or greater than nickel are niobium, vanadium, tantalum, molybdenum, ruthenium, titanium, and platinum [47] [49]. Other pure metals are unlikely to possess the hydrogen permeability properties required for application as HPE. Hydrogen permeability can be increased through alloying of different elements, which can change properties such as the activation energy for bulk diffusion and the number of available sites for hydrogen absorption. Engineering of the crystal structure to the more permeable FCC structure could also increase H permeability.

The hydrogen diffusivity D depends on the activation energy for bulk diffusion of hydrogen through an Arrhenius relationship, which means an increase in temperature is expected to increase the permeability, as was experimentally confirmed for nickel in an earlier study [12]. Robertson [50] summarised the existing experimental data on hydrogen permeation, diffusion and, solution in pure nickel into a temperature dependent permeability of $9.50 \cdot 10^{-9} \exp\left(\frac{-54.8}{RT}\right)$ $\mathrm{mol_{H_2}\,m^{-1}\,s^{-1}\,bar^{-0.5}}$. At room temperature and pressure this gives a H_2 permeation flux of 74 $\mathrm{nmol_{H_2}\,cm^{-2}\,s^{-1}}$, while at a pressure of 4 bar this figure is doubled and at 8 bar nearly tripled to $2.1 \cdot 10^2$ $\mathrm{nmol_{H_2}\,cm^{-2}\,s^{-1}}$.

2.4.2. Nitrogen Adsorption on Transition Metals

Nitrogen must be adsorbed on the HPE surface in order for NRR take place. Many modes of adsorption exist, each with their respective adsorption energy and activation energy. This section discusses the different modes of adsorption of nitrogen on nickel and the associated kinetics.

Firstly, a distinction has to be made between molecular adsorption and dissociative adsorption, the latter of which breaks the molecular bond yielding individual N atoms. Molecular adsorption can be divided into weaker physisorption and stronger chemisorption. The former has exceedingly weak interaction energies and is only observed at temperatures below 80 K on nickel [51] [52], molecular chemisorption is however preceded by physisorbed precursor states, as shown in Equation 2.38. Two stages of physisorption are traversed, a weakly bound γ adsorption where N_2 is oriented perpendicular to the metal surface, and stronger bound (α adsorption) where N_2 is oriented parallel to the metal surface. Finally, the molecule is chemisorbed at a binding energy of between 20 and 50 kJ mol^{-1} [52].

$$N_2(g) \rightleftharpoons {N_2}^*(\gamma) \rightleftharpoons {N_2}^*(\alpha) \longrightarrow {N_2}^* \tag{2.38}$$

The N_2 molecule can also be dissociated upon chemisorption, yielding chemisorbed atomic N, at an adsorption energy of between 110 and 180 kJ mol^{-1} [52]. This is known to occur spontaneously on a clean Ni surface at room temperature and a 0.1 mbar N_2 atmosphere [53]. Chemisorbed N is located on a surface site, not in an interstitial lattice site as is the case for N atoms in nickel nitride. It is not known whether direct adsorption into a near-surface interstitial N vacancy that was formed during the MvK mechanism cycle is possible, or whether surface-chemisorbed N is a necessary intermediate step.

Adsorption energies and activation energies differ for all of the modes of adsorption mentioned above. Further variations arise from the surface arrangement of the atoms, which can be monocrystalline or polycrystalline, the temperature, pressure, presence of contaminants, and the coverage fraction θ [54]. For example, on an iron surface, the dissociative chemisorption reaction of nitrogen has a coverage dependent activation energy [55], meaning that the rate of chemisorption decreases for high coverages. The activation energy is given by $E_a = -15 + 30\theta$ kJ mol^{-1} where θ is the coverage fraction [56].

The adsorption and desorption reactions kinetics can be modelled using Arrhenius laws with experimentally determined activation energies and frequency factors [24]. The Langmuir adsorption model is commonly used. This model is based on the assumption that the specific rate of adsorption r_{ads} is the product of the molecular flux Γ and the sticking factor s, as shown in Equation 2.39. The molecular flux is the number of moles approaching one square centimeter of surface per second, while the sticking factor is the probability for a molecule that approaches the surface to be adsorbed instead of being reflected. A complete model would consist of coupled rate equations for all the reactions in Equation 2.38, although the overall behaviour can be aggregated into a single Arrhenius law for simplicity .

$$r_{ads} = s\Gamma \tag{2.39}$$

The molecular flux is the frequency factor of the Arrhenius law, and can be approximated by the Hertz-Knudsen equation below.

$$\Gamma = \frac{p \cdot 10^{-6}}{\sqrt{2\pi MRT}} \tag{2.40}$$

Here, p is the (partial) pressure of the gas above the solid surface in Pa, M the molar mass of the gas particle in g mol^{-1} and T the temperature in K. It is apparent that according to this model, increasing the N_2 pressure should proportionally increase the adsorption of N, and thus also the NH_3 production rate if N adsorption is a limiting step.

The sticking factor consists of the exponential term of the Arrhenius law with the adsorption activation energy $E_a(\theta)$ containing a possible coverage dependence, multiplied by the surface coverage coefficient $f(\theta)$ and the condensation coefficient $\kappa(\theta)$ as modifiers of the frequency factor. The surface coverage coefficient accounts for the probability that a molecule impinges on a site that is still unoccupied, which would be $1-\theta$ in the case of associative chemisorption. However, since two unoccupied adsorption sites are needed to host the two N atoms in dissociative adsorption, $f(\theta) = (1-\theta)^2$ for the dissociative chemisorption reaction. The condensation coefficient $\kappa(\theta)$ is optional and can include kinetics of the precursor states, where $(1-\kappa)$ is the probability that an molecule that approached the surface evaporates before chemisorption could take place.

$$s = \kappa(\theta) f(\theta) e^{-E_a(\theta)/RT} \tag{2.41}$$

Next, some experimentally determined values for nitrogen adsorption on nickel and iron will be given. Dissociative nitrogen adsorption on Fe(111) has a reported sticking factor of $2.2 \cdot 10^{-6}$ exp($\frac{-3.3}{RT}$) with $E_a = 3.3$ kJ mol^{-1} for a zero coverage, with an adsorption energy of around 209 kJ mol^{-1} [57]. In the Haber-Bosch process, this step is the RDS. Grunze et al. reported a sticking factor of 10^{-7} for nitrogen adsorption on Ni(110) at temperatures below 200 °K [52]. Wedler et al. reported a $3.3 \cdot 10^{-8}$ sticking factor on nickel at 333 °K and $\theta = 0.01$, s decreasing with increasing temperature [58]. On the other hand, absence of interaction between N_2 and a clean Ni surface has been reported above 300 °K by Brundle et al. [59]. Another study argues that dissociative chemisorption does not occur on clean nickel surfaces at high temperatures (room temperature and above), and any observed adsorption is caused by active sites on the nickel provided by impurities, including N atoms that were actively sputtered onto the nickel surface [60]. The pre-adsorbed N atoms receive a slightly negative charge, lowering the activation energy and thus enabling dissociative nitrogen adsorption. This supports the evidence that nickel nitride prepared through plasma enhanced chemical vapour deposition of N activates N_2 at a higher rate than clean Ni [5]. There are other studies in which doping the metal surface with promotor atoms was specifically shown to increase the N bond strength and lower the activation energy for N_2 adsorption, this includes doping iron with potassium [61], and nickel with barium and aluminium [62].

The ammonia adsorption energy is modest at 63 kJ mol^{-1} [63], an indication that ammonia will desorb from the HPE without significant difficulty. The NH_3 desorption activation energy on nickel is 80 kJ mol^{-1}. N_2 desorbs from nickel with a relatively high activation energy of 211 kJ mol^{-1} [64]. Interestingly, nickel is also known to dissociate ammonia [63]. Nitrogen desorption is the limiting step in this process [64]. At is moment, it is not clear whether an ammonia decomposition side reaction is happening on the HPE.

Overall, the experimental literature poses a mixed picture, with some reports showing no direct N_2 activation by Ni itself, instead attributing detected interaction with N_2 to impurities, and other reports showing fairly small sticking coefficients at high temperatures and below ambient pressure. It should be noted that the majority of experimental results on gas-solid interactions pertain to low pressures below 0.1 Torr. At ambient pressures, the interaction could differ significantly, for example due to the increased presence of contaminants inhibiting adsorption. Hence, nitrogen adsorption cannot be ruled out as the RDS in ammonia synthesis with an HPE.

Nevertheless, an estimation for dissociative N_2 adsorption rate on Ni can be made with the experimental results. The surface atom density of a Monolayer (ML) is taken as $7 \cdot 10^{14}$ cm^{-2} according to experimental results [58] [65]. The sticking coefficient of $5.0 \cdot 10^{-8}$ at 273 °K and $\theta = 0.01$ is used [58] to approximate standard conditions. The only unknown parameter is the steady state surface coverage θ, which will depend on the rates of the other elementary steps. θ is expected to approach 0 if N_2 adsorption is the RDS, and $\theta \to 1$ if any of the subsequent steps is limiting. For standard conditions, the N_2 molecular flux given in Equation 2.40 will be about $1.52 \cdot 10^{-4}$ cm^{-2} s^{-1}. Multiplying this result by s results in an adsorption rate of about $7.59 \cdot 10^{-12}$ mol cm^{-2} s^{-1} for $\theta = 0.01$. Changing the implicit surface coverage coefficient in s from $(0.99)^2$ to $(0.01)^2$ to model $\theta = 0.99$ coverage gives a new sticking factor of $5.1 \cdot 10^{-12}$ and an adsorption rate of $7.75 \cdot 10^{-16}$ mol cm^{-2} s^{-1}. If N adsorption was the limiting step in NH_3 synthesis, the NH_3 production rate would not be able to exceed double these quantities,

given the 2:1 N_2:NH_3 stoichiometry. The results are most likely optimistic, because the sticking factors are expected to decrease from the reported values under ambient conditions due to competition with contaminants and increased surface coverage. Ammonia production figures from the HPE cell with hydrogen permeable electrodes are closer to the adsorption estimate at $\theta = 0.01$, an indication that nitrogen adsorption is a limiting step. This supports the hypothesis that an increase in pressure might yield increase ammonia production rates from the HPE cell.

2.4.3. Nickel Nitride Formation

From the previous section it has become clear that nitrogen adsorption on nickel could be a limiting step in ammonia synthesis with an HPE, and that there is a difference between N adsorbed on top of the nickel surface, or in interstitial lattice sites. Metals containing N atoms in regular interstitial sites in the lattice are called nitrides, and these materials can possess interesting catalytic properties, notably enhanced nitrogen adsorption and the ability to catalyse ammonia synthesis from N_2 through an MvK mechanism [60] [5]. Transition Metal Nitrides (TMNs) can form with MN or M_2N stoichiometries for early Transition Metals (TMs), but M_3N and M_4N are more prevalent for late TMs such as Ni [66]. Ni_2N was synthesised recently at high pressure according to one report [67]. Nickel nitrides can be produced through plasma enhanced chemical vapour deposition, exposing the nickel surface to a plasma with activated nitrogen atoms that enter the metal [66] [68]. The sticking factor is expected to be close to unity for the activated N radicals in the plasma [69], enabling N deposition in significant quantities. Applying a bias voltage to the substrate increases the N penetration into the bulk. Alternately, nickel can be sputtered in a nitrogen plasma, enabling even thicker bulk nitride depositions. Ni_3N crystallises in an HCP structure with lattice parameters a=4.621 Å and c=4.304 Å [68] [70]. The nitrogen atoms are ordered in the interstitial sites of Ni_6 octahedra to minimise mutual repulsion, as displayed in Figure 2.12.

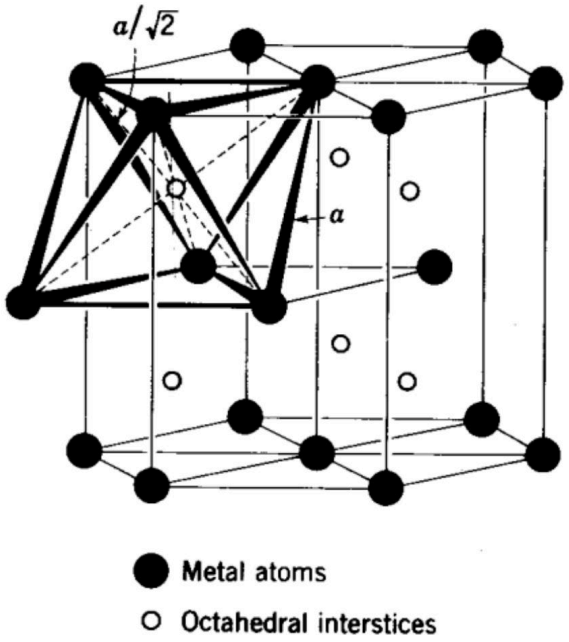

Figure 2.12: Schematic displaying the position of octahedral sites in an HCP lattice. Lattice parameter a is marked. c is half the distance between the hexagonal top and bottom layers of atoms. Image reproduced from [71].

Ni_3N is a metastable material that decomposes at temperatures above 300 °C to form Ni metal and N_2 [72]. Earlier studies showed a stability of the HPE up to at least 150 °C [12]. However, other studies how that exposure to hydrogen can significantly lower the decomposition temperature of Ni_3N, with exposure to 1 Torr H_2 atmosphere resulting in decomposition at 180 °C [73], and decomposition between 50 and 165 °C was observed under higher hydrogen activity [74] [75]. Under these conditions Ni_3N is apparently reduced to pure Ni and NH_3 [76]. This is of significant importance to the stability of the nickel nitride catalyst, as H will be readily available due to permeation, and decomposition reactions to either N_2 or NH_3 without sufficient adsorption of N_2 to replenish the nitride will cause the reaction to cease. The rate of Ni_3N decomposition is also affected by the degree of ordering of the metal, with polycrystalline nickel nitride such as the HPE decomposing more readily than highly ordered nickel nitride [73].

The metastability of nickel nitride and the predicted tendency to decompose under elevated temperatures require an estimation of the N content in the HPE after the nitriding process and before usage in the ammonia synthesis cell. Comparison of this initial N content with the total NH_3 yield of the experiment allows calculation of the contributions N_2 and Ni_3N as N sources for NH_3. Since Ni_3N is the most stable nickel nitride stoichiometry and the deposition conditions and sample analysis support this stoichiometry as the nitride present in the HPE [66] [72], this stoichiometry will be used for the calculated N content. The gravimetric density of Ni_3N is $7.71\,g\,cm^{-3}$ [70], which gives an N quantity of $4.06 \cdot 10^{-9}\,mol\,cm^{-2}\,nm^{-1}_{Ni_3N}$. This is in reasonable agreement with the deposition dose required to reach the Ni_3N stoichiometry as reported elsewhere [68]. The N content of nitrided HPEs is available in Appendix D.

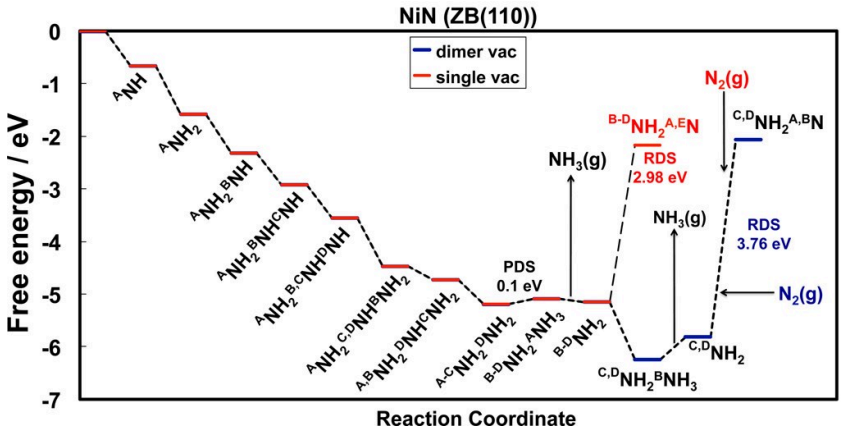

Figure 2.13: Density Functional Theory (DFT) based free energy diagram for nitrogen electroreduction to ammonia via a MvK mechanism on zincblende (110) nickel nitride. Differentiation between two pathways is made, single vacancy being the replenishment of the N vacancy after the desorption of a single NH_3 molecule, leaving an additional adsorbed N on the surface. The dimer vacancy pathway involves the release of a second NH_3 molecule before the simultaneous replenishment of two N vacancies through dissociative adsorption of N_2. The different N sites are marked with letter A-E. The PDS is the third hydrogenation of ^{A}N at 0.1 eV, and the RDS is the replenishment of the N vacancy through N adsorption at 2.98 eV. Image reproduced from [37].

Density Functional Theory (DFT) analyses can be of value to screen catalyst materials for stability, activity, and selectivity in greater numbers than would be possible experimentally. The computational results can be flawed, and hence experimental verification is important. For NRR, the studies consist of calculating the free energy of every intermediate on the catalyst surface. Using this information, the RDS and PDS can be determined, as well as the tendency for N vacancies to migrate into the bulk. Activation energies between stable intermediates can also be estimated. In a study of mononitrides (MN stoichiometry) with rocksalt and zincblende crystal structures, the most promising TMN candidates identified for NRR were ZrN, VN, NbN, CrN [77] [78] [79]. It is noted that the used crystal structure is different from the HCP structure that is most common in experimental reports on nickel nitrides. Figure 2.13 displays a Free Energy Diagram (FED) of the MvK mechanism on NiN with zincblende

(110) crystal structure. Most elementary steps in the cycle are downhill in free energy, except for the final hydrogenation of the ^{A}N atom and the replenishment of the N vacancy. The hydrogenation steps involve electron transfer and can thus be overcome by an applied potential, making vacancy replenishment the RDS. NbN appears the most able to regenerate vacancies through N_2 activation out of Sc, Ti, V, Cr, Mn, Y, Zr, Nb, Mo, Hf, Ta, W, and Re that were investigated [38]. Figure 2.14 can be used to infer the tendency of vacancies to migrate into the bulk on different TMNs.

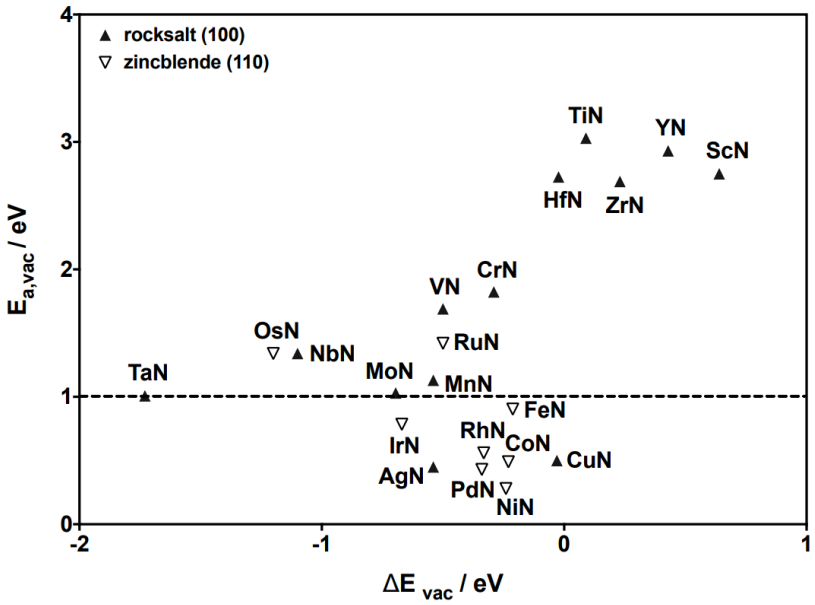

Figure 2.14: DFT-based plot of the free energy difference ΔE_{vac} between an N vacancy on the surface and in the first sub-surface layer, and the activation energy $E_{\text{a,vac}}$ for vacancy migration from the surface to the sub-surface. X-axis values below 0 indicate it is energetically favourable for an N vacancy to migrate to the bulk, which is the case for most TMNs included here. When the activation energy is above 1 eV (dashed line) the TMN is considered stable. Image reproduced from [78].

Apart from the possibility that DFT results do not hold true in practice, the requirement of high H permeability for the HPE further reduces the choices of electrode material. Hence, combining the properties of two materials could be a sound strategy to drastically improve stability and activity. For example, the reported difficulty for Ni_3N to regenerate itself was circumvented through a Ni loaded LaN catalyst with a dual mechanism in which N_2 is activated and adsorbed on vacancies in LaN and hydrogenated on the Ni clusters [80]. Other combinations of catalyst materials could also improve activity and stability.

2.4.4. Electrolyte Boiling Point

The HPE cell will be operated above room temperature to improve reaction kinetics. In particular, the overall reaction will benefit from an increased ammonia desorption rate and hydrogen permeation efficiency [6]. To increase the temperature past 100 °C, the boiling point of the electrolyte must be increased. This is done through increasing the electrolyte concentration and raising the hydrostatic pressure within the cell.

Dissolving a non-volatile solute such as salt in water will raise the boiling point through a process called boiling point elevation. Boiling of a liquid starts the moment when the vapour pressure exceeds the surrounding pressure. The vapour pressure is the pressure that a vapour exerts on its surroundings when it is in thermodynamic equilibrium with its condensed phase. When the vapour pressure that presses a bubble outward is greater than the surrounding pressure, boiling is observed. Adding a non-volatile solute with zero vapour pressure to a solvent lowers the total vapour pressure, hence requiring a higher temperature to overcome the surrounding pressure. A nearly saturated potassium hydroxide solution has a boiling point of 132 °C. This enables the operation of the electrochemical cell at 120 °C at atmospheric pressure.

Raising the hydrostatic pressure in the electrolyte can also significantly elevate the boiling point. Two boiling points at different pressures can be related through the Clausius-Clapeyron relation, shown in Equation 2.42.

$$\ln\left(\frac{p_2}{p_1}\right) = \frac{R}{\Delta H_{vap}}\left(\frac{1}{T_1} - \frac{1}{T_2}\right) \tag{2.42}$$

Here, T_1 and T_2 are the boiling points at pressures p_1 and p_2 respectively, R is the gas constant and ΔH_{vap} is the enthalpy of evaporation of the solvent at T_1. The dependence of the boiling point on pressure is given in Figure 2.15 where 132 °C is taken at the original boiling point of a concentrated KOH solution at atmospheric pressure, with the enthalpy of evaporation taken as 39 kJ mol^{-1}, calculated using a three-characteristic parameter model [81].

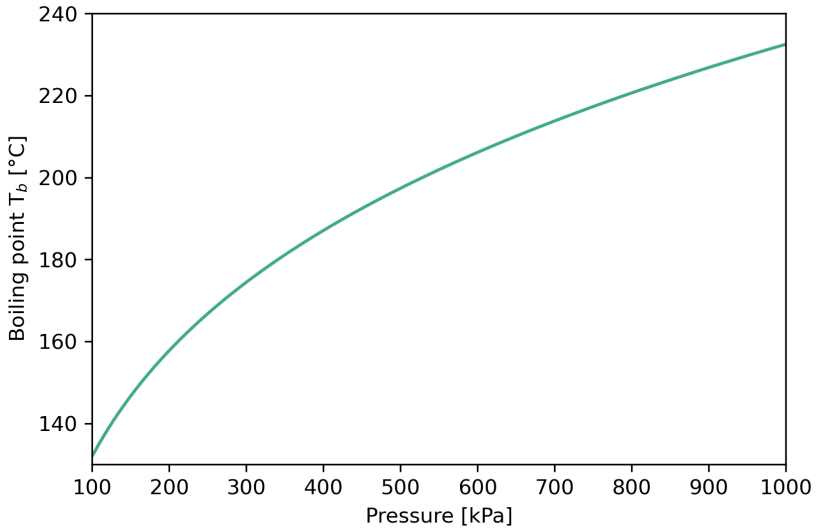

Figure 2.15: Pressure dependence of the boiling point of a 45 $\%_{wt}$ KOH solution. Raising the pressure to 5 bar will elevate the boiling point to nearly 200 °C, higher than the maximum operating temperature of the PEEK using for the cell.

Hence, the boiling point of the electrolyte can be increased significantly by pressurising the cell. The temperature limits that will be encountered first are the stability of the nitride layer, and the maximum operating temperature of the PEEK cell at 180 °C.

The past two sections mentioned a number of ways in which raising the pressure in the cell could affect the thermodynamics and kinetics of electrochemical ammonia synthesis with an HPE. In summary, hydrostatic pressure could inhibit HER (subsection 2.2.1), increase H-permeation through the HPE (subsection 2.4.1), improve the N_2 adsorption rate on on nickel nitride (subsection 2.4.2), and allow for significantly increased temperatures without exceeding the electrolyte's boiling point (subsection 2.4.4). It is expected that these changes combined improve the NH_3 yield and faradaic efficiency of the HPE cell.

2.5. Analysis Methods

The current stage of electrochemical ammonia synthesis and the associated low yields introduce specific challenges when it comes to reliably measuring cell performance. Trace amounts of extraneous N species (such as, NH_3, NO_x, N_2O, NO_x^-, and other, more labile forms of N) are often present in the environment in concentrations of around the same order of magnitude as catalytically produced ammonia from the experiment. The reduction of nitrogen oxides into ammonia is generally more facile than direct NRR. This has led to an increasing number of reported false positives and non-reproducible

results [11]. Because the performance of a cell is usually quantified in terms of the specific NH_3 yield and the faradaic efficiency, both of which rely on accurate determination of the ammonia concentration in the product stream, a reliable method for quantifying the ammonia concentration is crucial. In Equation 2.43 and Equation 2.44 for the specific NH_3 production rate and faradaic efficiency of the cell, x_{NH_3} is the detected mole fraction of ammonia in the analysed gas stream, $\dot{m}$ is the mass flow rate of the gas stream in $mL_n\,s^{-1}$, A is the working electrode surface area in cm^2, F is the Faraday constant and I is the total current supplied to the working electrode in A.

$$u_{NH_3} = \frac{x_{NH_3}\dot{m}}{A} \tag{2.43}$$

$$\eta_{NH_3} = \frac{3x_{NH_3}\dot{m}F}{I} \tag{2.44}$$

The indophenol blue method is a popular water based colorimetric analysis method, which has the disadvantages of being laborious, especially for obtaining measurements at different points in time. The sample handling can furthermore lead to contamination by compounds from the surroundings. An inline Gas-Chromatography (GC) method was previously developed to simplify the analysis process by eliminating the need for sample handling, and reducing the risk of contamination [82].

Apart from the need of reliable quantification of the cell's products, it is also of importance to inspect the composition and structure of the catalyst material, for example to investigate the deactivation mechanism. To this end X-Ray Photoelectron Spectroscopy (XPS) and Scanning Electron Microscopy (SEM) were used to study the nickel and nickel nitride electrodes. The next subsections give an overview of the operating principles of the three analysis methods.

2.5.1. Gas Chromatography

Gas-Chromatography (GC) is an analysis method used to separate gaseous compounds and quantify their concentrations in the sample. The principle is based on a carrier gas (mobile phase) flowing through a column (stationary phase) at a fixed flow rate and pressure. A sample is injected into the circuit and carried through the column by the carrier gas. Because different compounds have differing interactions with the column lining, the chemical compounds in the sample each reach the exit of the column at different characteristic retention times after the injection. The components of the sample are thus separated based on retention time. The retention time of a chemical depends on the column length, diameter, material, carrier gas, temperature, and flow rate, and overlapping retention times are possible. For example, the separation of ammonia and water is not straightforward requiring a column specialised for that purpose. Chemicals exiting the column are detected electronically, commonly using a Pulsed Discharge Ionisation Detector (PDD) or Thermal Conductivity Detector (TCD). Peaks will be present in the detector's signal centered around the retention time of each chemical, and the area below these peaks compared to the background signal level is usually linearly correlated to the concentration of the chemical in the injected sample. A calibration using samples with known concentrations is needed to obtain the slope and intercept of this relationship.

Ammonia is known to physisorb onto metal surfaces, introducing an error when passing the product gases through bare metal tubing. The SilcoNert® 2000 inert silicon based coating from SilcoTek reduces the ammonia physisorption from $1.5 \cdot 10^{14}$ molecules cm^{-2} to $5.7 \cdot 10^{12}$ molecules cm^{-2} [83]. Physisorption onto Polytetrafluorethylene (PTFE) and Polyether Ether Ketone (PEEK) are also low, under $1 \cdot 10^{13}$ molecules cm^{-2} [83].

One method to ensure reliable NH_3 production measurements is isotope labelling of the N_2 feed gas. This is based on the principle that any significant background contaminations will contain N^{14} atoms because the only other naturally occurring isotope is N^{15} with a molar abundance of 0.364 % [84]. When supplying the cell with ${N_2}^{15}$, the detected NH_3 containing N^{15} will thus be almost fully attributable to catalytic reduction of N_2 to NH_3. By studying the product composition with mass spectroscopy, the NH_3 species containing N^{14} and N^{15} can be separated. This method seems to be robust, but it must be remembered that N_2^{15} is itself commonly produced from N^{15} labelled ammonia, because the nitrogen

isotopes are separated more easily in this form [85]. With this in mind, the possibility that N^{15} labelled feed gas could contain trace amounts of N^{15} labelled ammonia must be considered. Another variant of this method that circumvents this issue would be to feed the cell with N_2^{14} because this is available in reliable high purity form, and design the setup such that any contamination of non-catalyticcally formed NH_3 entering the product stream will be N^{15} labelled. The main example is to produce any surface nitrides with N^{15}, keep the cell surroundings under an atmosphere of N_2^{15} gas in a glovebox.

2.5.2. XPS

X-Ray Photoelectron Spectroscopy (XPS) is a powerful analytical technique for investigating the surface composition and chemical state of materials, including their electronic structure. At its core, XPS operates based on the photoelectric effect: when X-rays bombard a sample's surface, the surface atoms eject photoelectrons, whose kinetic energies are measured by a detector. The fixed photon energy and differing kinetic energy of the photoelectrons can be used to infer the binding energy the electron experienced in the material. By analysing the binding energies of these photoelectrons, one can discern elemental composition, oxidation states, and chemical environments of the atoms on the electrode's surface. From the kinetic energy of the photoelectron, its binding energy in the material can be determined through a conservation of energy equation:

$$E_b = E_p - (E_k + \phi) \tag{2.45}$$

Here E_b is the electron binding energy, E_p is the photon energy, and E_k is the kinetic energy of the detected photoelectron, all given in eV. $\$phi$ is a work function term to correct for energy losses of the electron as it exits the material and enters the detector.

XPS allows for the identification of surface species, such as adsorbed intermediates or contaminants, which can significantly influence the electrode's activity and selectivity. Initially, the raw XPS spectra are processed to account for background signals, ensuring accurate determination of peak positions and intensities corresponding to different elements. Subsequently, peak fitting algorithms are employed to divide the spectra into individual peaks representing various elemental species. This deconvolution allows for identification of chemical states and bonding environments present on the electrode surface.

Additionally, depth profiling capabilities of XPS allow for the examination of elemental distribution as a function of depth into the electrode material. Depth profiling experiments elucidate any compositional gradients or changes within the surface layers, providing insights into surface modifications, diffusion processes, or interface interactions that impact the electrode's performance.

2.5.3. SEM

A scanning electron microscope generates highly detailed images with which the nanostructure of the HPE can be studied. It operates by directing a focused electron beam onto the sample surface, and detecting secondary electrons emitted from the sample's topmost atomic layers, providing high-resolution images that reveal surface topography, roughness, and nanostructural details. Complementary to secondary electrons, backscattered electrons aid in distinguishing materials with different compositions and characterising elemental distributions or phases within the electrode's nanostructure.

3

Methods and Materials

This chapter details the experimental methods used to investigate the research questions outlined in chapter 1. The work is divided in four parts, namely design and operation of the high pressure electrochemistry setup, preparation of the nickel nitride electrodes, production of electrodes with increased electrochemical surface area, and the used analysis methods.

3.1. Electrochemistry Setup Design

In this section the components and design considerations of the electrochemistry setup will discussed in detail.

3.1.1. Electrochemical Cell

The setup is built around two sizes of polyether ether ketone (PEEK) electrochemical flow cell with circular electrolyte and gas compartments, shown in Figure 3.1a and Figure 3.1b. PEEK is a suitable material for ammonia synthesis because it is inert to ammonia, relatively impermeable for trace amounts of gases, and offers high chemical, mechanical, and temperature resistance compared to other synthetic materials. Stainless steel offers some further advantages in the the areas of temperature and pressure resistance, as well as durability, although such a cell would require a coating to decrease the surface adsorption of ammonia. A nickel foil hydrogen permeable electrode (HPE) is used as the separator of the electrolyte and gas compartments, with O-rings on both sides providing the required seal. The inner diameter of the electrolyte compartment O-ring is taken to determine the Geometric Surface Area (GSA), since this is corresponds with the wetted electrode area. For the large cell, the inner diameter of the electrolyte compartment O-ring is 3.91 cm, yielding a geometrical active surface area of 12.0 cm^2, while for the smaller cell the diameter is 1.75 cm, yielding a geometrical active surface area of 2.40 cm^2. Electrical connection to the HPE is achieved using copper tape applied between the two half cells. The half cells have ports through which 1/16” outer diameter gas lines and 1/8” outer diameter electrolyte lines are connected with PEEK flangeless fittings from IDEX Health & Science. These fittings are rated up to pressures of 17 bar. An additional port on the electrolyte half cell is used to connect the >99% purity, 1 mm diameter nickel wire counter electrode. The two cells are displayed in Figure 3.1.

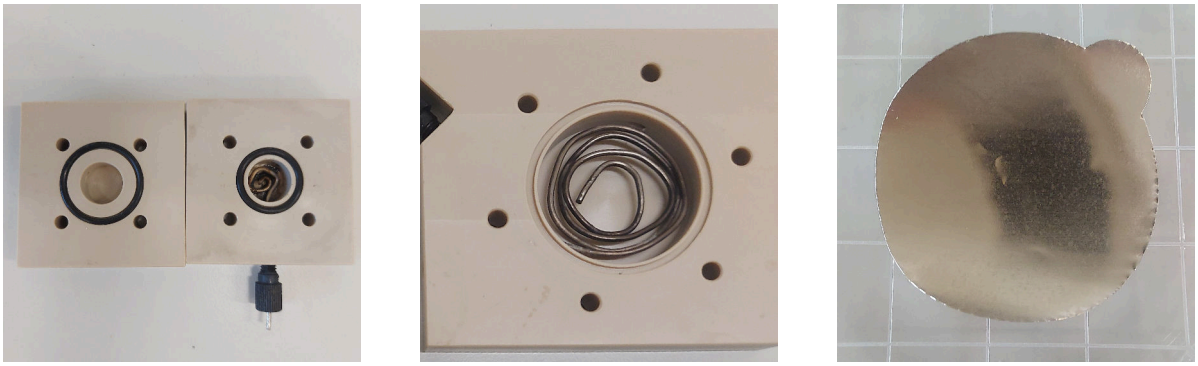

(a) Two small half cells, with the gas compartment on the left and the electrolyte compartment on the right.

(b) Large electrolyte half cell with the embedded nickel counter electrode.

(c) A 29 mm diameter nickel foil sample with lip to apply the copper tape.

Figure 3.1: Ammonia synthesis cell parts.

A Finite Element Analysis (FEA) was carried out in Autodesk Inventor to determine the pressure limits of the cells at their given dimensions. The electrolyte compartment of the larger cell is the weakest half cell, because its sidewall has a thickness of 3.5 mm whereas the gas compartment's sidewall is 13.2 cm thick. The smaller cell has the same sidewall thickness and smaller diameter compartments. The FEA indicated that the large electrolyte half cell could withstand pressures of up to 15 bar at a temperature of 120 °C, taking safety factor of 3.52 ul into account. This pressure would produce a maximal outward displacement of 330 µm in the centre of the circular compartment. An image of the FEA result is shown in Figure 3.2. Pressures below 15 bar will not pose a problem for the mechanical strength of the cells. PEEK is also suited to operation at high temperatures, with a melting point of 340°C and a maximum operating temperature of 180°C.

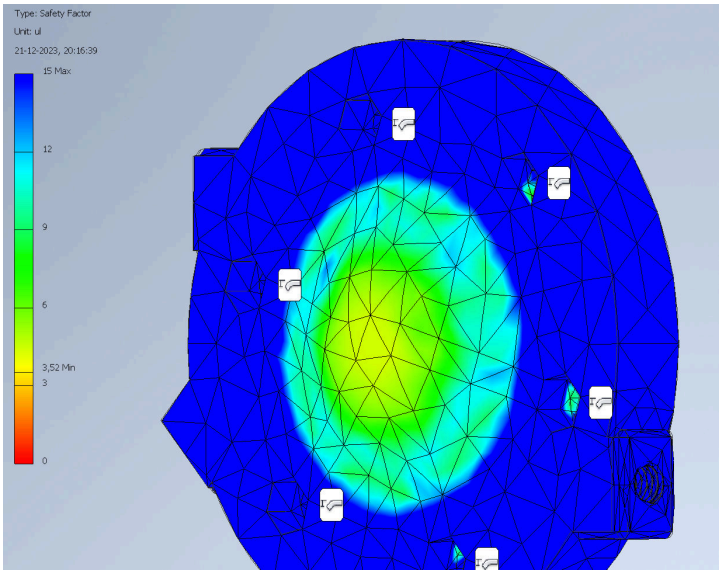

Figure 3.2: Safety factor image of the 3.91 cm diameter electrolyte half cell. The minimal safety factor is 3.52 ul, in the centre of the electrolyte compartment sidewall.

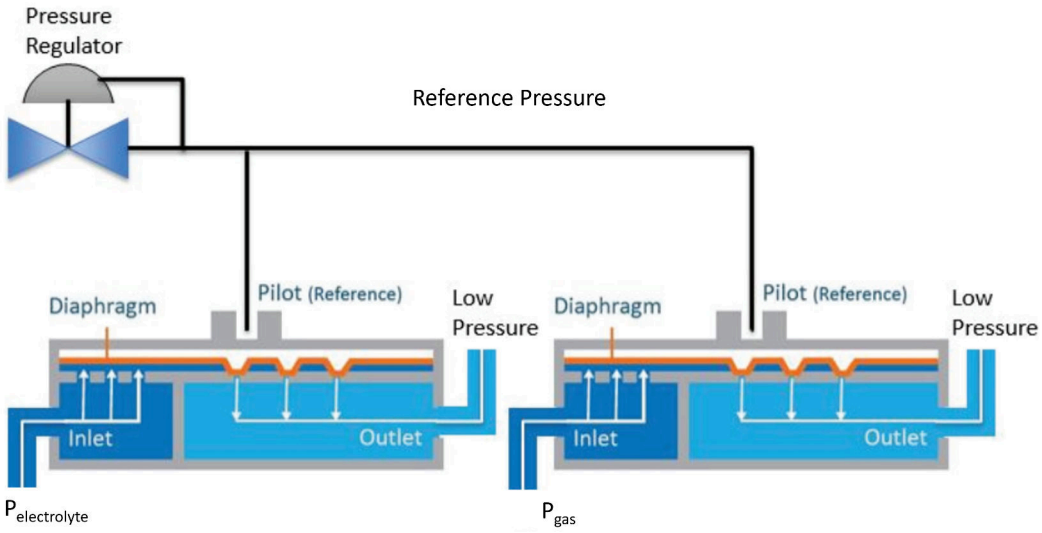

Figure 3.3: Schematic showing the operational principle of Equilibar back pressure regulators. Image reproduced from [86].

3.1.2. Back Pressure Regulators

Because the HPE is a thin metal foil, it is essential to minimise the differential pressure in the two compartments to prevent a rupture of the HPE. Two Equilibar Research Series ZF0 back pressure regulators connected to the same control pressure were used to achieve equal pressure in both compartments. A back pressure regulator is used when the flow rate through the regulator should depend on the pressure in the upstream volume, as opposed to conventional pressure regulators that admit flow based on the pressure in the downstream volume. The Equilibar design consists of a membrane that is pressed down from the top by a control pressure. A fluid channel is blocked by the membrane until the pressure at the inlet exceeds the control pressure. When this happens, membrane is pushed upwards allowing flow through the channel [86]. A schematic of the design is shown in Figure 3.3. The regulators use a stainless steel diaphragm and are rated at a maximum pressure of 200 bar. The dead space in the back pressure regulator is 0.25 mL. The control pressure is regulated by a Specken Drumag PCS-DRP70 electronic pressure controller. This controller is recommended for use with the Equilibar back pressure regulators, and enables computer controlled operation the back pressure regulators in a range from vacuum to 70 bar.

Before operating the cells at elevated pressure, the maximal pressure differential across the HPEs was investigated. As expected, the HPE in the large cell was most prone to ruptures. However, for both cells the maximum pressure differential was influenced by which of the compartments contained the highest pressure. The HPE is supported in the centre of the shallow gas compartment sidewall when there is an overpressure in the electrolyte compartment. Rupture in this scenario occurred at a pressure differential of 4 bar, and 5 repeated cycles to a 2 bar differential pressure caused no rupture. Overpressure on the gas side causes the HPE to bulge towards the deeper electrolyte compartment, where it is unsupported. Hence, rupture was already observed to 2 bar overpressure in the gas compartment. To prevent this type of rupture, three layers of polypropylene mesh were added to the electrolyte compartment to support the HPE. This improved the rupture pressure to 6 bar overpressure and 5 repeated cycles to a 2 bar differential pressure caused no rupture.

3.1.3. Auxiliary Equipment

The electrolyte circuit was fitted with a 60 mL stainless steel reservoir and a pump (Tuthill DGS.11) with flow rate control. This pump has PEEK bearings and gears, giving the required chemical and temperature resistance. The pump is rated for a system pressure of up to 34.5 bar and operating temperatures of up to 176 °C. Nitrogen gas is fed into the space above the electrolyte level in the reservoir to pressurise the circuit. Both the gas and electrolyte circuits have Bronkhorst EL-Flow Prestige Mass Flow Controllers (MFCs) with control functionality at their gas inlets, and Gems Sensors

3100 series pressure sensors inside the circuits. The electrolyte circuit has a Bronkhorst EL-Flow Select MFC downstream of its back pressure regulator to measure out-flow, while an MFC is placed at the GC outlet to measure out-flow of the gas circuit. All gases had a purity of 99.999%, and were passed through a gas purifier (Agilent OT3-4) before reaching the the inlet MFCs. This purifier removes oxygen and moisture from the gas feed to below 15 ppb, with performance rated up to 120 psi (17 bar). Furthermore, the gas circuit is fitted with a 1 psi (69 mbar) check valve from Swagelok between the cell and the gas compartment inlet MFC to prevent flooding of the MFC in the event of an HPE rupture. A moisture trap consisting of a frame with two layers of PTFE film, with a second outlet to a 10 psi (0.69 bar) check valve from Swagelok, is placed between the back pressure regulator and the GC to prevent electrolyte reaching the GC during an HPE rupture event.

All tubing and the back pressure regulators in the gas circuit are coated with a SilcoNert® 2000 coating to enhance their inertness towards ammonia. This significantly improves the response time of the measurements through a reduced ammonia retention time in the circuit. Ammonia adsorption on bare stainless steel will delay the onset of ammonia detection until the tubing walls are saturated with adsorbed ammonia. The adsorbed ammonia will be measured upon eventual desorption, causing significant measurement delay and the measured amount might deviate from the full amount.

The cell and electrolyte reservoir were placed inside a Carbolite PF30 lab oven to regulate the temperature. The pump was placed outside the oven causing a loss of electrolyte temperature when electrolyte passed through the pump. This was mitigated by placing additional tubing between the pump and the cell inlet and monitoring the electrolyte temperature at the cell inlet with a Fluke 52 II digital thermometer. The temperature probe was attached to the electrolyte tubing at the cell inlet and insulated using aluminium foil. During normal operation, the temperature on the oven thermostat was 5 degrees higher than the cell inlet temperature because of the heat loss at the pump. A schematic of the electrochemistry setup is given in Figure 3.4.

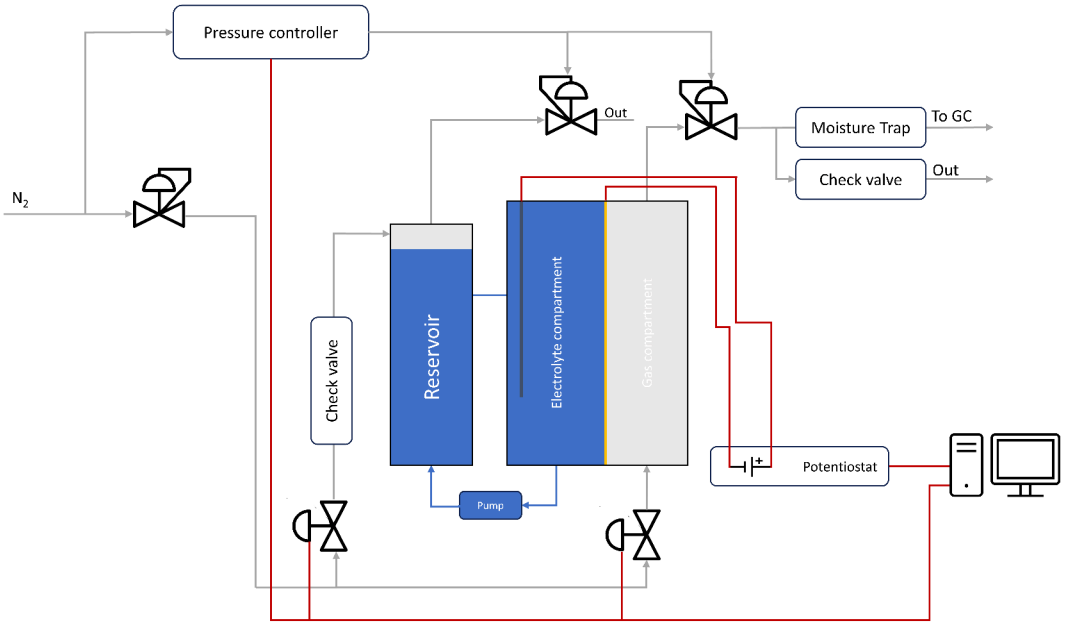

Figure 3.4: Schematic representation of the electrochemistry setup. Red lines indicate electrical connections, grey lines indicate gas tubing.

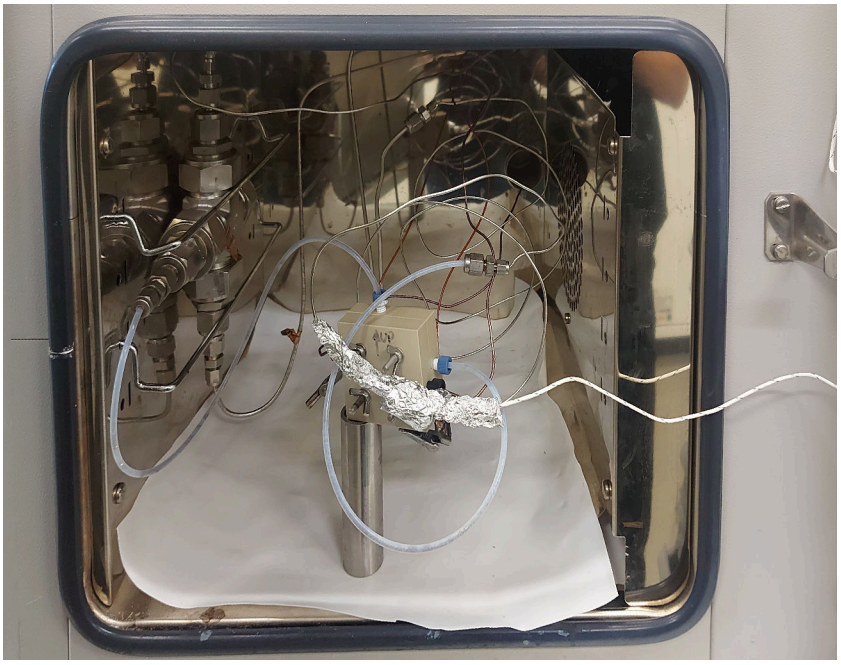

Figure 3.5: Image of the lab oven with the stainless steel reservoir, smaller PEEK cell and tubing.

3.1.4. Gas Chromatography

The product gas from the cell was analysed using a Thermo Scientific TRACE 1300 Series GC. Channel 1 is equipped with a PDD together with a Select Low Ammonia column from Agilent. This column enables adequate separation of water and ammonia in the chromatogram. The column is situated in the GC oven, and helium is used as carrier gas. This channel is used for the ammonia detection. A temperature program with linearly increasing temperature from 70 to 230 °C during 3 minutes was applied with a 250 µL sample loop. Subsequently, a cool-down period of between 3 and 4 minutes followed, giving a total injection duration of between 6 and 7 minutes. Channel 2 is equipped with a TCD in combination with a series of columns (Hayesep N 60-80 0.5m, XL-Sulfur 60-80 2m, Molsieve 5 Å 60-80 3m), located in the valve oven which was kept at 100 °C. Channel 2 was used for hydrogen and helium detection, and used nitrogen as carrier gas. A third channel could be used to detect other gases such as CO_2, CO, O_2, and N_2, while only the CO_2 retention time was under the 3 minutes interval for detection, so this channel was not used.

GC calibration

The gas-chromatography system has been calibrated in earlier research using a calibration grade bottle of nitrogen gas blended with 13.8 ppm ammonia. This starting concentration was diluted with purified nitrogen for additional data points, confirming a linear relationship between the area of the NH_3 peak and the ammonia concentration in the analysed gas [12]. A recalibration was deemed necessary to account for changes in sensitivity. A single concentration from a bottle with 18.8 ppm ammonia in nitrogen was used for this measurement, because the linear relationship was already established, hence a zero intercept was assumed. The 18.8 ppm ammonia concentration is reasonably close to the practical concentrations encountered during the measurements. Gas from the bottle was fed into the GC at 1, 2, 5, and 10 $mL_n\,min^{-1}$. Five injections were taken at each flow rate and averaged to determine the calibration slope at the respective flow rate. The H_2 calibration is given in Figure C.1. Peak areas were converted to molar NH_3 and H_2 production rates, and these were integrated with midpoint integration to calculate the total yields.

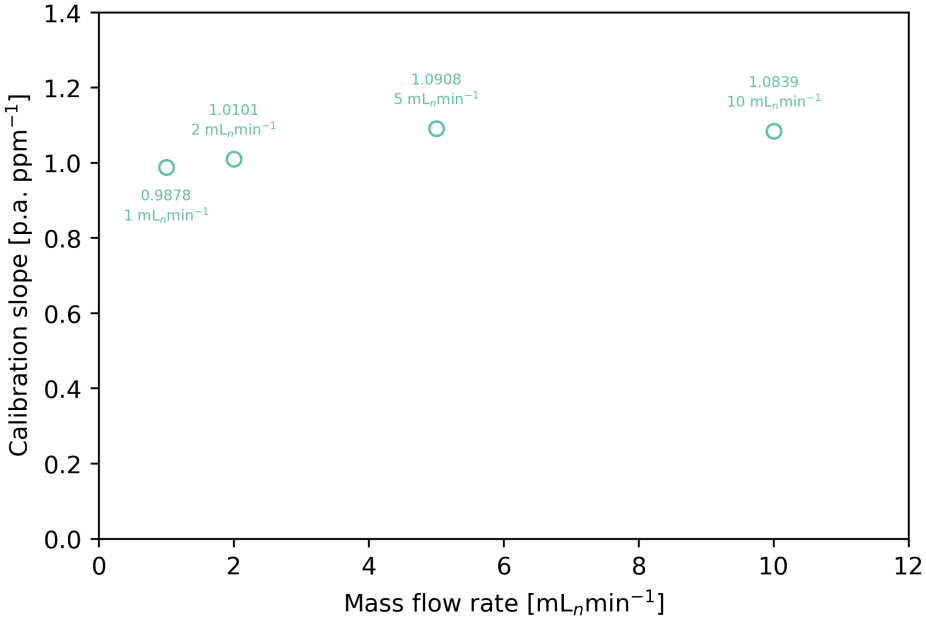

Figure 3.6: Dependence of the GC calibration slope for ammonia on the mass flow rate of the gas inlet. These slopes indicate the measured peak area per ppm of ammonia in the sample. The sensitivity of the system shows some dependence on the mass flow rate up to 5 $mL_n\ min^{-1}$.

3.1.5. Potentiostat

An Ivium Vertex potentiostat was used as a power source. The cell was connected in a two electrode setup because of the difficulties associated with placing a third electrode in the small electrolyte compartment. Chronopotentiometry was used, setting a fixed current and recording the cell potential every 200 ms.

3.1.6. Leak Testing

After assembly of the cell, some leakage issues were encountered with the flangeless IDEX fittings. In some cases these would not conform to their pressure rating of 17 bar. Because the catalyst is highly sensitive to deactivation by contaminants, especially oxygen, it is essential to ensure the absence of leaks. An Alcatel/Adixen ASM 142 helium leak detector was used to survey the cell for leaks, and the fittings were found to leak even when liquid leak detection spray would not indicate so. Subsequently, the bottoms of the PEEK cell ports were flattened to improve the seal of the ferrules, and additional gaskets were added in the ports. This improved the seal and further leak detection test were below the detection threshold.

3.2. Hydrogen Permeable Electrode Preparation

Most ammonia synthesis experiments were carried out using hydrogen permeable electrodes with a nickel nitride (Ni_3N) layer on the face that was exposed to the gas side of the cell. Nickel foil with a thickness of 12.5 µm and purity of 99.9% was purchased from Goodfellow and used as HPE. Circular pieces were cut out using a Cricut Maker^{TM} 3 cutting machine, with diameters of 53 mm and 29 mm depending on the cell that was used. An image of a 29 mm diameter circular Ni foil sample is given in Figure 3.1c. The nitride layer was produced using plasma enhanced chemical vapour depositioning. In earlier studies, the nitriding process was performed in an AJA Ultra High Vacuum (UHV) magnetron sputtering system [53]. During the present research, difficulties with this process were encountered, as will be discussed below. Hence, another nitriding process using an Atomic Layer Deposition (ALD) system was also used, and its effectiveness was investigated.

3.2.1. AJA Nitriding Process

The AJA nitriding process is the same as was carried out in earlier research [5]. The nickel foil samples were loaded into the AJA UHV system, and subsequently cleaned under an Argon:Hydrogen plasma to remove nickel oxides and other surface contaminants. The base pressure of the system was 10^{-7} bar. During cleaning, gas flow rates of 17.5 $mL_n\,min^{-1}$ and 2.5 $mL_n\,min^{-1}$ were used for Ar and H_2 respectively, while maintaining the pressure at 5 µbar. The plasma was generated for 30 min at 20 W RF power with a 0 V reflection and a voltage of 178 V.

After the cleaning step a nitriding step followed, in which N was deposited onto the nickel to create a thin layer of nickel nitride. A 2:1 Ar:N_2 mixture was fed into the deposition chamber with flow rates of 14 $mL_n\,min^{-1}$ Ar and 7 $mL_n\,min^{-1}$ N_2, while maintaining the pressure in the deposition chamber at 20 µbar. The plasma was generated for ten minutes at 40 W RF power and a voltage of 242 V. These parameters are similar to the parameters that produced a Ni_3N stoichiometry in earlier studies [68].

After the cleaning and nitriding the foils were removed from the sputtering system and kept in a glove-box under nitrogen atmosphere to prevent degradation of the nitride layer, even though stability was demonstrated for up to 150 °C [53].

Plasma deposition of nitrogen works by accelerating the reactive nitrogen radicals towards the substrate where they are adsorbed. Between batches of HPE preparation, the AJA system was also used for depositing layers of various other elements through sputtering, for example Cu, Ag, and Ti. It was discovered that the relatively high plasma pressure and power settings used for the nitrogen plasma could dislocate elements that were still present in the chamber from previous sputtering processes and deposit them onto the electrode, causing contamination. The surface of a sample that was believed to be contaminated was inspected using XPS, revealing 30% copper on the nickel surface, presumably dislocated from the chamber walls and sample holder. The details of the XPS measurements are given in section subsection 3.5.2. In earlier research it had not been discovered that elements remaining in the chamber from previous sputtering processes could be dislocated at the applied plasma settings. All samples that were prepared before the discovery of this issue could be contaminated with elements that were recently sputtered in the system. This type of contamination was subsequently prevented by pre-sputtering the empty deposition chamber with Ni to cover any contaminants. Furthermore, an alternative process for preparing the samples using an ALD system was developed. The milder plasma conditions and smaller amounts of residue in the depositioning chamber prevented contamination in this system.

3.2.2. ALD Nitriding Process

Nickel foil HPEs were prepared in a Fiji G2 high-vacuum thermal ALD system from Veeco. ALD is a technique used to create thin films of between 1 nm to 100 nm, depositing around one ML per cycle. The element used for deposition is fed into the vacuum chamber as part of a chemical compound called a precursor. The precursor adsorbs to the substrate surface forming a uniform layer, after which excess precursor is purged. A second gas is then fed into the chamber that reacts with the precursor, leaving just the deposition element on the surface. This process can then be repeated for multiple layers, yielding a highly uniform film. Reactive plasma's can be used to incorporate other elements into the deposition or drive the precursor reaction. For the formation of a nickel nitride layer, a precursor is not necessary as a nitrogen plasma provides the reactive nitrogen that is incorporated into the nickel lattice. After loading the samples the reaction chamber was heated to 100 °C and pumped to a pressure of 10^{-7} bar. Similar to the AJA process an Ar:H_2 plasma cleaning step preceded the nitriding step. Argon was fed into the chamber at 80 $mL_n\,min^{-1}$ and H_2 at 20 $mL_n\,min^{-1}$ for 20 s, after which the plasma was ignited at 300 W DC for 30 s. Pure argon was then flowed for another 20 s. This cycle was repeated 30 times. The nitriding step used a similar pattern with equal timings, argon flow rate and plasma power, and a N_2 flow rate of 50 $mL_n\,min^{-1}$. This cycle was repeated 20 times to yield a total deposition time of 10 min, equal to that of the AJA process. No bias was applied to the plasma, making the convection of the reactive gas the only driver of N particles towards the substrate.

3.3. Electrochemistry

The cell was cleaned by rinsing first with MilliQ water and then with isopropanol to remove contaminants, and subsequently dried in a vacuum oven at 50 °C for one hour to remove moisture. Next, the two half cells were joined together with an HPE inside. The assembled cell was placed in the lab oven, and the electrolyte circuit was filled with a 45 wt% KOH solution, subsequently setting the electrolyte flow rate to 20 mL min^{-1} to facilitate removal of gas bubbles produced during the electrochemistry. The system was flushed with nitrogen to purge the air remaining in the system from the assembly, and a GC sequence was started. The mass flow rate of the gas at the cell inlet was 1 mL_n min^{-1} unless stated otherwise. If necessary for the experiment, the oven temperature and the control pressure for the back pressure regulators were set and time was left for the system to reach equilibrium temperature and pressure. The potentiostat was set to chronopotentiometry. During the experiment the chromatograms were monitored for ammonia, hydrogen gas, water and other reaction products or contaminants.

3.4. Electrode Surface Morphology

It is well known that the surface morphology of an electrode can influence the catalytic activity [87]. Pores, crevices and other microstructures increase the electrochemical surface area, while the addition of defects in the surface region of the catalyst can change the kinetics of reactions with adsorbed intermediates. The Roughness Factor (RF) is the ratio of Electrochemical Active Surface Area (ECSA) and GSA.

$$RF = \frac{ECSA}{GSA} \tag{3.1}$$

The surface morphology of the nickel HPE was altered using electrodeposition to investigate the effect of higher electrochemical surface area for ammonia synthesis. Numerous electrodeposition techniques were considered, which can be divided into porous and non-porous deposits. Porous deposits are made by applying a reduction potential well beyond the HER onset potential, causing the metal to deposit around hydrogen bubbles adsorbed to the metal surface, resulting in a porous structure [88]. Typical deposition current densities exceed 1 A cm^{-2}. Electrochemical active surface areas of over 1000 times the geometric area are possible with this hydrogen bubble templated electrodeposition [89]. Factors influencing the roughness factor are the deposition current density, deposition duration, and composition of the deposition solution, including the presence of surfactants that increase the bubble size, and hence the porosity [90].

Non-porous deposits are made with lower current densities. Deposition of various nanostructures including nanopillars [91] [92], nanospheres [93], or nanowalls [94] is possible by using additives in the deposition solution that change the growth mechanism of the deposition, and altering the deposition current and duration.

For the application of ammonia synthesis with HPEs, a non-porous pillar morphology was chosen. The high current densities needed for porous electrodeposition make these methods less suited to depositing a relatively large surface area of over 3 cm^2. Furthermore, since the ammonia synthesis reaction requires protons emerging from the bulk of the nickel electrode, a thick porous region may not contribute significantly to activity, because H atoms will have difficulty reaching the porous region through metal diffusion. Of the non-porous morphologies, the pillar structures can provide a relatively large increase in ECSA [95].

Pillar morphologies can be deposited using screw-dislocation driven growth [96]. A screw dislocation is a local step in the crystal surface that promotes the interaction between the surface and the electrolyte and accelerates deposition. The deposition growth proceeds in two directions, namely the along the dislocation core (V_c), and outward parallel to the substrate surface (V_o). Adding a capping reagent restricts the outward edge growth rate, resulting in sharper pillar like structures, as displayed in Figure 3.7c. NaCl was identified as cost effective capping reagent [91] [90] and used in the deposition solutions.

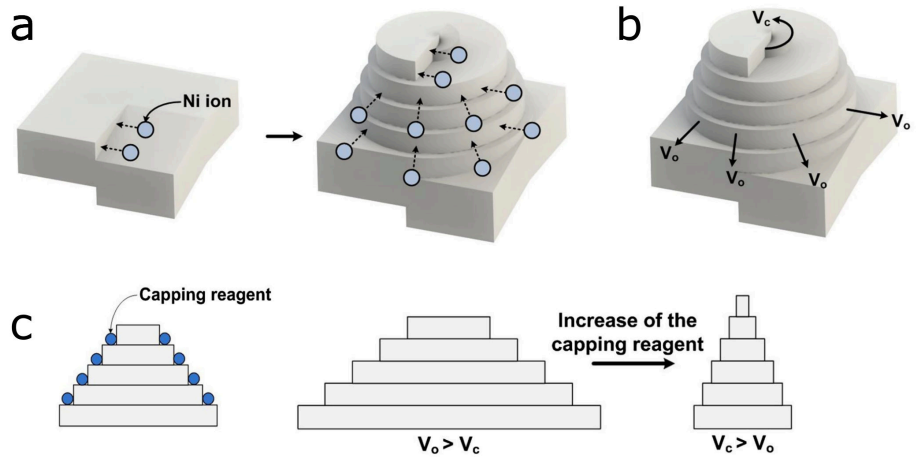

Figure 3.7: Schematic depiction of screw-dislocation driven growth. a: A screw-dislocation and the spiral growth pattern. b: Dislocation core growth direction V_c and outer edge growth direction V_o. c: Schematic showing how a capping reagent restricts the growth in the outer edge direction, increasing the aspect ration of the electrodeposition structures and forming a pillar nanostructure. Image reproduced from [91].

The three used electrodeposition solutions were based on the proposed solution in the study by Lee et al. [91], using NaCl as a capping reagent. All chemicals were sourced from Sigma-Adrich with lab grade purity of over 99.5%. The solution compositions given in Table 3.1 were prepared by first dissolving the given amounts of Ni salt into MilliQ water that was continuously stirred, followed by dissolving the additives, namely boric acid in the case of the Watts solution and NaCl for all solutions. The solutions were stored in polypropylene bottles for up to one day. The same nickel foil electrodes as described in section 3.2 were used. The foils were cleaned by submerging them in acetone for 5 min and rinsing with MilliQ, and subsequently in 1 M hydrochloric acid for 1 min and again rinsing with MilliQ. To electroplate one side of the nickel foil, it was placed in the centre of an H-cell, where the ion exchange membrane would normally be situated. By filling one compartment of the H-cell with the electrodeposition solution only the exposed area of the nickel foil will be plated, which is a circular area with 2 cm diameter, yielding a surface area of 3.14 cm^2. The deposited area was deliberately larger than the 2.4 cm^2 active area of the cell, to account for slight misalignment of the HPE during assembly of the cell. The HPE was sealed in the H-cell by Ethylene Propylene Diene Monomer (EPDM) gaskets on both sides. An anode of 99.9% purity nickel foam and a Hg/HgO reference electrode with 1 M KOH internal solution were used. The assembled H-cell was placed in a bath with MilliQ water heated to 60 °C, as this temperature was a prerequisite for the growth of the nanostructure [91]. A Parstat MC-1000 potentiostat set to chronopotentiometry was used for electrodeposition, with the deposition currents and duration ranges given in Table 3.1 .

Solution	**Ni-Sulfate**	**Watts Bath**	**Ni-Sulfamate**
Composition	1.5 M $NiSO_4$	1 M $NiSO_4$ 0.15 M $NiCl_2$ 0.70 M H_3BO_3	1.5 M $Ni(SO_3NH_2)_2$
Capping reagent	2 M NaCl		
Current density	5–30 mA cm^{-2}		
Deposition time	30 s – 5 min		
Temperature	60 °C		

Table 3.1: Parameters of electrodeposition experiments.

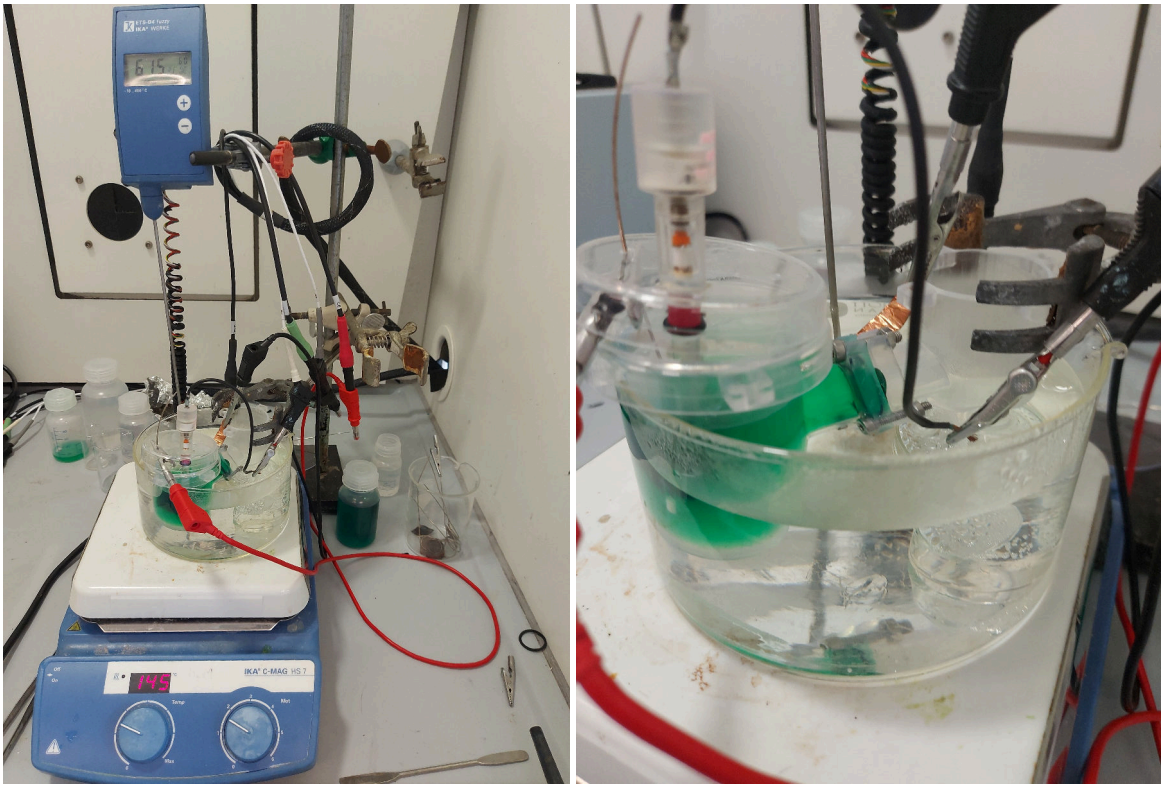

(a) Image of the electroplating setup. The H-cell containing the plating solution is situated in a heated bath of MilliQ water.

(b) Close up image of the H-cell showing the nickel electrode in the centre.

Figure 3.8

Cyclic voltammetry was used to determine the electric double layer capacitance of the electrodes before and after deposition. The H-cell was filled with a 0.5 M KOH solution. Using the same potentiostat and electrode setup as with the electrodeposition, the Open Circuit Potential (OCP) between the working and counter electrode was first measured. Subsequently a 10-cycle cyclic voltammetry program in a range of 50 mV above and below the measured OCP was carried out, with scan rates of 5, 10, 25, 50, 75, 100, 125, 150, 175, and 200 mV s^{-1}. The resultant current densities are exclusively associated with charging and discharging of the EDL, because no electrochemical reaction is driven at 50 mV above or below the OCP. The specific double layer capacitance c_{dl} in F cm^{-2} was determined by taking the slope of the linear relationship between the (dis)charging current density i in A and the scan rate v in V s^{-1} using Equation 3.2.

$$c_{dl} = \frac{i}{v} \tag{3.2}$$

The reported specific double layer capacitance c_{Ni} of bare nickel wire in 0.5 M KOH is 40 µF cm^{-2} [97]. This is the capacitance associated with flat nickel having equal ECSA and GSA. The roughness factor of a nickel surface can be calculated with Equation 3.3. Alternatively, the specific capacitance of the electrode before the electrodeposition can be taken as c_{Ni}, which gives a more accurate indication of the true RF if the measured c_{Ni} differs from the literature due to differences in the ECSA measurement conditions.

$$RF = \frac{c_{dl}}{c_{\text{Ni}}} \tag{3.3}$$

3.5. Analysis Methods

3.5.1. Scanning Electron Microscopy

The HPEs were inspected with a JEOL JSM-IT700HR scanning electron microscope. This system is also capable of elemental analysis with Electron Diffraction X-Ray Spectroscopy (EDS). The system was used in high vacuum mode.

3.5.2. X-Ray Photoelectron Spectroscopy

An XPS depth profiling measurement was conducted, to determine the surface composition of the HPE, and also to quantify the presence of nitrogen in the subsurface. The XPS spectra were recorded on a K-alpha spectrometer from Thermo Scientific. The base pressure of the UHV analysis chamber was $2 \cdot 10^{-9}$ mbar, and the spot size was 400 µm for all measurements. Survey spectra were taken at a pass energy of 140 eV and a step size of 0.4 eV. The depth profiles were made by etching the material and taking a spectrum at a pass energy of 152.4 eV and a step size of 0.319 eV. Peaks of C1s, N1s, O1s, Ni2p3, and if present K2p were included in the depth profile. The etch time was 10 s, and each sample was etched with between 8 and 10 levels at two etch rates. On the tantalum oxide reference material, the etch rates are 0.26 nm s^{-1} and 0.09 nm s^{-1}. This will differ for the samples, and the etch rate will also change with the sample composition below the surface. Still, the above numbers can be used as an indication. The two etch rates ensure a high resolution depth profile near the surface while also measuring deeper into the subsurface material.

4

Results and Discussion

Numerous avenues for improving the production rate and faradaic efficiency of ammonia synthesis with hydrogen permeable electrodes have been explored. Ammonia synthesis was carried out at pressures of up to 8 bar, and temperatures from 20 °C to 120 °C. Electrodes with an increased electrochemical surface area were produced and their performance was measured. Furthermore, a new process for producing the surface nitrides on the HPE was introduced and tested. These, along with other experiments, give a new insight in the reaction mechanism at play in the HPE ammonia synthesis cell. Regrettably, the constant ammonia production at 120 °C reported in earlier research [6] could not be reproduced. All measurements displayed a degree of decreasing production as time progressed. The instability and decreasing nature of the ammonia production rate caused the true effects of any parameter change during the course of an experiment to be indiscernible from the decreasing trend. For example, conducting a stepped current measurement with a single HPE would not produce accurate results, considering an increased current later in the experiment would result in a smaller NH_3 production rate compared to at the start of the experiment. Overall, this complicated the measurements and generated additional work, since all parameter changes had to be tested in separate measurements with a fresh HPE, and any changes during experiments had to be repeated at the same moment in subsequent measurements to ensure comparability. The raw data of the reported constant production [6] was not available. Still, new insights can be obtained from the results discussed in this chapter. In section 4.1, results of the control experiments are presented that confirm the existence of a catalytic pathway from N_2 to NH_3 using the nickel nitride HPE. In subsection 4.1.2, the atomic surface composition of the HPE before and after ammonia synthesis is presented. The difference in performance between the two nitriding processes is discussed. Next, the effects of pressure and temperature on the hydrogen permeation and ammonia production rate are discussed in section 4.2 and section 4.3. The results of the electrodeposition experiments and the performance of the resulting samples are presented in section 4.4. Finally, reasons for the deactivation of the nickel nitride catalysts are given in section 4.5.

4.1. Control Experiments

4.1.1. Current Response

As an initial test, the behaviour of the H permeation and NH_3 production was investigated under repeated current cycles, with the result presented in Figure 4.1. The current density was set to 0.5 mA cm^{-2} for 30 min at two instances. Both H permeation and ammonia production display a prompt response to the first current cycle, although only the H permeation decreases rapidly to zero after electrochemical charging is stopped. The NH_3 production decreases more slowly, which indicates that desorption from the electrode is a limiting step at this temperature. Retention on the tubing walls is unlikely to be a factor since ammonia was detected promptly after starting the electrochemistry. Upon the second current cycle a similar response is observed for the H permeation, while hardly any change is apparent in the ammonia production. The downward trend in the ammonia production rate is stopped and the production rate increases slightly before continuing to decrease. Thus, the initial NH_3 production rate is not recovered.

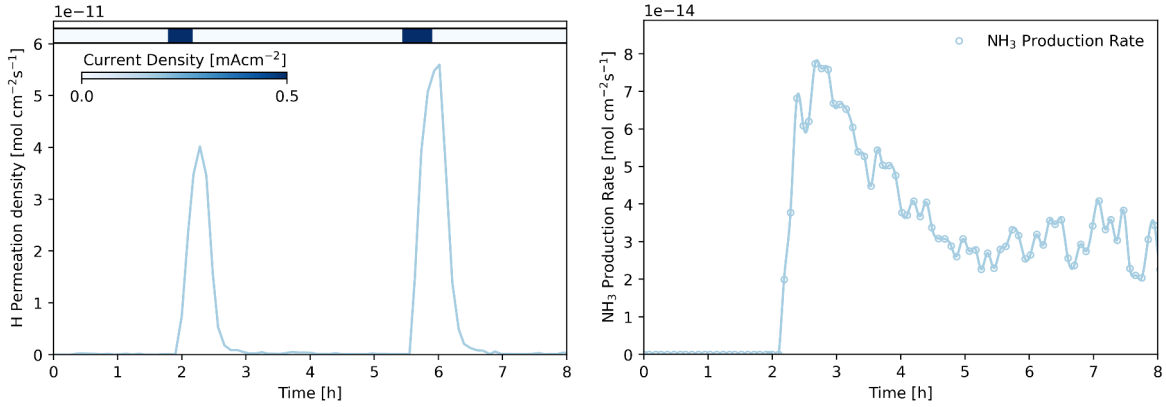

(a) Molar H permeation density over time at room temperature and pressure. The bar at the top of the figure indicates when the current was applied.

(b) NH_3 production rate over time at room temperature and pressure.

Figure 4.1: Molar H flux density and ammonia production rate at room temperature and pressure, and a charging current density of 0.5 mA cm^{-2}.

The current efficiencies of the measurement in Figure 4.1 are given in rows 1 and 2 of Table 4.1. Three efficiencies are identified, namely the permeation Faradaic Efficiency (FE) being the number of protons crossing the HPE as a percentage of the applied current, the hydrogenation efficiency as the percentage of permeated H that takes part in the reaction to ammonia, and the total FE being the number of protons used for synthesising NH_3 as a percentage of the applied current. The method for calculating these values is given in section A.4. In Figure 4.1, the permeation FE is 1.1%, while the hydrogenation efficiency is only 0.139%, giving a total FE of 0.015%. Hence, nearly the full amount of the permeated H is detected as H_2.

Desorption from the electrode surface can be improved by raising the temperature to 120 °C [12], which will decrease the response time of NH_3 GC measurements. In addition, Figure 4.1 forebodes an issue that was present during all the experiments conducted, namely that the initial NH_3 production is inflated by partial or complete consumption of the nitride layer, masking limitations in the reaction mechanism for the duration that N is abundant on the nickel surface.

4.1.2. HPE Surface Composition

Both used and unused HPEs were inspected with XPS depth profiling to analyse the nitride layer. The XPS spectra are given in Figure 4.2. It is apparent that on both types of HPE lattice N from the surface and subsurface is converted during operation. The used samples in Figure 4.2b and Figure 4.2d display a minor N1s peak in the surface spectrum recorded before etching, and no discernible peaks in the spectra recorded after etching. The surface peak is also markedly reduced. It is not known whether the remaining N corresponds to an equilibrium amount or whether the HPE would deplete further through continued operation. It is apparent that the AJA nitriding process deposits greater quantities of N, even though this method does not accelerate radicals to the substrate with a bias voltage. The greater N content is likely due to the nitrogen plasma being generated at a higher power setting, and the 1:2.5 ratio of Ar:N_2 in the plasma.

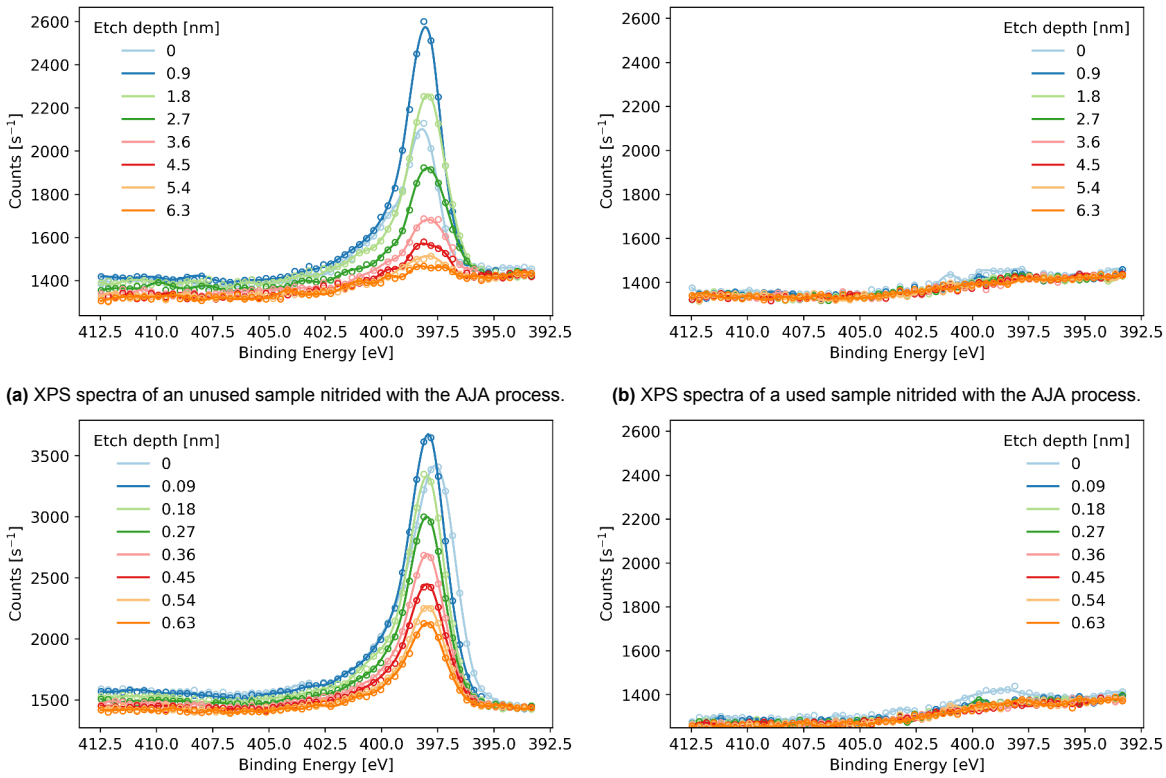

(a) XPS spectra of an unused sample nitrided with the AJA process.

(b) XPS spectra of a used sample nitrided with the AJA process.

(c) XPS spectra of an unused sample nitrided with the ALD process.

(d) XPS spectra of a used sample nitrided with the ALD process.

Figure 4.2: XPS spectra of HPE samples at 8 different etch levels. The region around the N1s binding energy is plotted. The pass energy was 152.4 eV and the step size was 0.319 eV. All y axes have the same scale except figure c which has larger y scale. The Etch depth is given for tantalum oxide reference material.

The N content calculations in section D.2 show N content equivalent to 6.78 nm and 2.31 nm thick Ni_3N layers in the ALD- and AJA-prepared HPEs respectively, the difference confirming the visual appearance of Figure 4.2. The N loading associated with this indicates that not all deposited N is reduced to NH_3, and that decomposition into N_2 is taking place in parallel. This assessment is greatly dependent on the estimation of the N loading prior to the experiment, and possible inaccuracies in this result demand careful consideration.

4.1.3. Confirmation of Catalysis Using Argon

To confirm the process of catalytic reduction of gaseous N_2 to NH_3, a control experiment was conducted under an inert argon atmosphere. Isotope labelling experiments confirming this pathway have been conducted before and were thus not repeated [5] [6]. Both HPE samples were nitrided with the ALD process, and the experiment was conducted at 120 °C. At 5.5 hours into the measurement, a current density of $0.25\,\mathrm{mA\,cm^{-2}}$ was applied to extract the maximum yield from the samples. As shown in Figure 4.3, the total NH_3 yield per square centimeter of electrode in the first 10 hours is $1.98 \cdot 10^{-9}\,\mathrm{mol_{NH_3}\,cm^{-2}}$ under argon atmosphere and $1.31 \cdot 10^{-8}\,\mathrm{mol_{NH_3}\,cm^{-2}}$ under nitrogen atmosphere, a 6.65 times greater yield. This confirms that N_2 can be activated by the HPE and that the presence of gaseous N_2 contributes to replenishment of N vacancies in the nitride, enhancing the NH_3 production. It is also apparent that a small amount of H permeates through the electrodes at OCP, caused by a spontaneous oxidation reaction on the HPE, namely $7\,Ni + 2\,H_2O \longrightarrow Ni(OH)_2 + 2\,Ni_3H$. Hence, NH_3 can be produced without applying a current. At atmospheric pressure, a $0.25\,\mathrm{mA\,cm^{-2}}$ current density does enhance the H permeation significantly above the spontaneous H insertion.

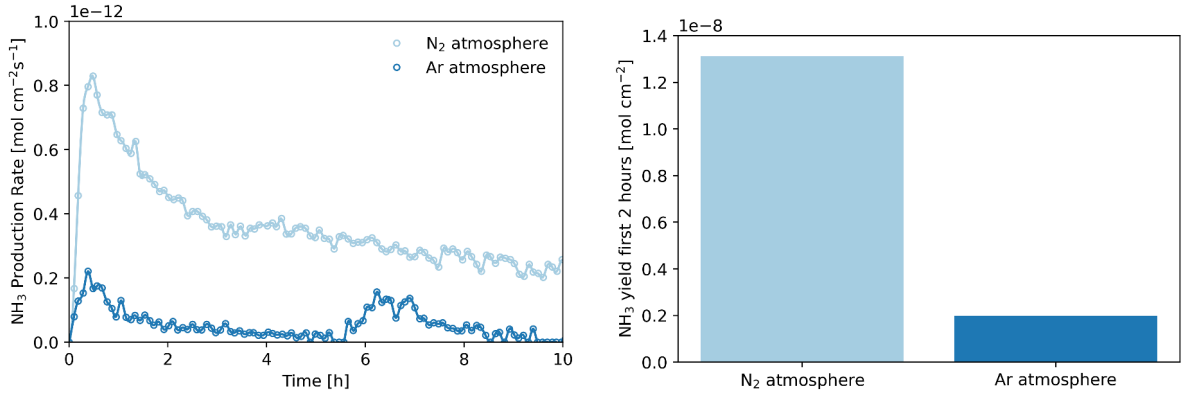

(a) NH_3 production rate under N_2 and Ar atmosphere.

(b) NH_3 yield during the first 10 hours under N_2 and Ar atmosphere.

Figure 4.3: Comparison of ammonia production rate and total yield for an ALD-nitrided electrode under argon and nitrogen atmospheres. The temperature was 120 °C, and the current density was $0.25\,\mathrm{mA\,cm^{-2}}$, applied 5.5 hours into the experiment.

4.1.4. Ammonia Yield of Two Nitriding Processes

XPS depth profiling given in Appendix D indicates that the ALD process deposited 2.93 times more N in the HPE than the AJA process. Thus, a comparison between the two processes was necessary, as given in Figure 4.4. This provides insight into the effect of N loading on the elementary steps, and the presence of side reactions such as Ni_3N decomposition to N_2. The experiment was conducted at 120 °C and the current density was $0.25\,\mathrm{mA\,cm^{-2}}$, applied 5.5 hours into the experiment.

The production rate of the HPE prepared with the ALD process starts at nearly double that of the HPE prepared with the AJA process, and the difference diminishes with time. After 9 hours the production rates are nearly equal. This is expected from the similar N loading that was observed with XPS after the experiment. The discrepancy between the increase in N loading and the increase in NH_3 yield between the ALD- and AJA-prepared HPEs is an additional indication of Ni_3N decomposition to N_2.

Furthermore, these measurements are relatively constant, albeit at a lower production rate than the $2.54 \cdot 10^{-12}\,\mathrm{mol\,cm^{-2}\,s^{-1}}$ that was reported earlier for these conditions [6]. The NH_3 yield during the first 9 hours of the ALD-prepared electrode is greater than that of the AJA-prepared electrode by $3.77 \cdot 10^{-9}$ mol or 44%. The fact that the NH_3 yield did not increase by the same factor as the N insertion between the AJA and ALD nitriding processes indicates part of the deposited N is participating in some reaction other than NH_3 synthesis, possibly Ni_3N decomposition to N_2.

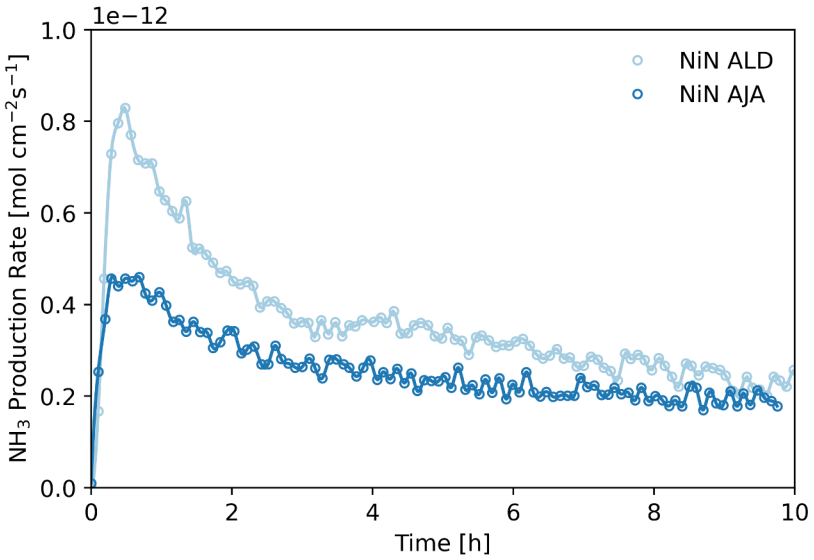

Figure 4.4: Comparison of the NH_3 production rate for HPEs prepared with the ALD and AJA processes. The current density was 0.25 mA cm^{-2} 5.5 hours into the experiment, and the temperature was 120 °C.

4.2. Temperature

In the following two sections on temperature and pressure effects two series of experiments are included, one using the larger 3.91 cm diameter cell and AJA-prepared electrodes, and another series using the smaller 1.75 cm diameter cell and electrodes prepared with the ALD process. The main reasons for this change in approach are the contamination that was eventually discovered on the AJA-prepared electrodes, and the requirement of smaller electrodes for electrodeposition. The measurements on the large cell were conducted before the HPE contamination was discovered, and hence all measured samples could also be contaminated in some form. It was decided to include the measurements to critically compare them with the later ALD-based measurements, investigating similarities or differences in the temperature and pressure dependence of the H permeation and NH_3 production.

The large cell measurements displayed in Table 4.1 confirm the significant increase in H permeation when increasing the temperature from 20 to 120 °C reported earlier [6]. The H permeation flux at 0.5 mA cm^{-2} is improved 33 times by the temperature increase. The hydrogenation efficiency decreases with increased H permeation, indicating N hydrogenation and NH_3 desorption limit the NH_3 production at when N is abundant on the HPE, and their optimal rate is significantly below the H permeation rate at 0.5 mA cm^{-2} at both 20 and 120 °C.

The results for the smaller cell in Table 4.2 are broadly comparable to those in Table 4.1, except for the low H permeation at 0.5 mA cm^{-2} and 120 °C. This is an example of unstable H permeation resulting from non-uniform wetting of the HPE with electrolyte. The small cell was prone to this issue because its shape and size made gas removal challenging. Table B.2 contains results from a 3D-printed cell with a compartment design more conducive to gas removal, resulting in improved H-permeation.

Furthermore, H permeation is remarkably low at 0.25 mA cm^{-2} compared to 0.5 mA cm^{-2}, indicative of a similar effect to what was noted in subsection 4.1.3. The optimum H activity for insertion into the HPE is not reached at current densities below 0.5 mA cm^{-2}, resulting in low H permeation efficiencies. The resulting level of H permeation is not limited by the H permeability of the HPE at room temperature. Interestingly, the exceptionally low H permeation flux in row 25 and 26 of Table 4.2 give rise to a hydrogenation efficiency of nearly 55%, indicating that with initial N loading achieved by the ALD nitriding process, the optimal hydrogenation rate is close to the observed ammonia production rate in these rows. Increasing the permeation flux lowers the hydrogenation efficiency drastically.

#	i [mA cm^{-2}]	E [V]	T [°C]	p [bar]	H_{perm} [mol cm^{-2} s^{-1}]	H_{perm} FE [%]	u_{H_2} [mol cm^{-2} s^{-1}]	u_{NH_3} [mol cm^{-2} s^{-1}]	Hydr. Eff. [%]	Tot. FE [%]
1	0.5	1.80	20	1	$5.54 \cdot 10^{-11}$	1.07	$2.76 \cdot 10^{-11}$	$2.57 \cdot 10^{-14}$	0.139	0.0015
2	0.5	1.55	120	1	$1.73 \cdot 10^{-9}$	33.32	$8.63 \cdot 10^{-10}$	$1.49 \cdot 10^{-13}$	0.026	0.0086
3	5	1.60	120	1	$2.26 \cdot 10^{-9}$	4.36	$1.13 \cdot 10^{-9}$	$3.29 \cdot 10^{-14}$*	0.004*	0.0002*
4	10	1.68	120	1	$3.05 \cdot 10^{-9}$	2.94	$1.53 \cdot 10^{-9}$	$2.70 \cdot 10^{-14}$*	0.003*	0.0001*

Table 4.1: Large cell measurement results on the temperature dependence of H permeation and NH_3 production rate. Cells marked with * are NH_3 peaks recorded late in the experiment, and thus not representative of initial NH_3 production. The row numbers match the raw GC data table in Appendix C. Two or more injections are averaged per row.

#	i [mA cm^{-2}]	E [V]	T [°C]	p [bar]	H_{perm} [mol cm^{-2} s^{-1}]	H_{perm} FE [%]	u_{H_2} [mol cm^{-2} s^{-1}]	u_{NH_3} [mol cm^{-2} s^{-1}]	Hydr. Eff. [%]	Tot. FE [%]
5	0.25	1.60	20	1	$1.39 \cdot 10^{-11}$	0.54	$6.54 \cdot 10^{-12}$	$2.88 \cdot 10^{-13}$	6.197	0.0334
6	0.5	1.73	20	1	$1.59 \cdot 10^{-10}$	3.08	$7.95 \cdot 10^{-11}$	$1.56 \cdot 10^{-13}$	0.293	0.0090
7	0.25	1.20	120	1	$4.21 \cdot 10^{-12}$	0.16	$9.50 \cdot 10^{-13}$	$7.69 \cdot 10^{-13}$	54.841	0.0890
8	0.5	1.25	120	1	$2.21 \cdot 10^{-10}$	4.26	$1.10 \cdot 10^{-10}$	$3.74 \cdot 10^{-13}$*	0.508*	0.0216*
9	1	1.41	120	1	$1.65 \cdot 10^{-9}$	15.89	$8.23 \cdot 10^{-10}$	$3.57 \cdot 10^{-13}$*	0.065*	0.0103*
10	5	1.54	120	1	$1.43 \cdot 10^{-9}$	2.76	$7.14 \cdot 10^{-10}$	$4.72 \cdot 10^{-14}$*	0.010*	0.0003*

Table 4.2: Small cell measurement results on the temperature dependence of H permeation and NH_3 production rate. Cells marked with * are NH_3 peaks recorded late in the experiment, and thus not representative of initial NH_3 production. The row numbers match the raw GC data table in Appendix C. Two or more injections are averaged per row.

4.3. Pressure

Figure 4.5 displays the ammonia production rates and the total yield over the first four hours of measurement with AJA-prepared HPEs at pressures from 1 to 8 bar. These measurements were carried out with a current density of 0.5 mA cm^{-2}, and a temperature of 120 °C. The mass flow rate of nitrogen through the gas circuit was 1 mL$_n$ min^{-1} at all times, to prevent excessive ammonia dilution causing increased measurement error. At a constant mass flow rate, the residence time of N_2 in the circuit increases linearly with the pressure. This led to an increasing delay in the appearance of the NH_3 peak in the chromatograms, which has been corrected for in Figure 4.5 to give a clear comparison. The graphs start on the first GC injection with an ammonia peak. In fact, the decreased volumetric flow rate revealed separation of H_2 and NH_3 in the gas circuit before injection into the GC, arising from NH_3 adsorption onto the tubing walls. This was corrected for in Table 4.3.

There is no clear relationship between the pressure and the NH_3 production rate, even though a linear relationship would be expected if the adsorption of nitrogen was the limiting elementary step in the reaction. While the yield at 2 bar is increased by 36% relative to atmospheric pressure, the 4 and 8 bar measurements show a slight decrease in the production rate and total yield compared to 2 bar. The 4 bar measurement does not surpass the 2 bar measurement at any point in time. Overall, it appears that increasing the pressure beyond two bar has no significant effect on the ammonia production rate.

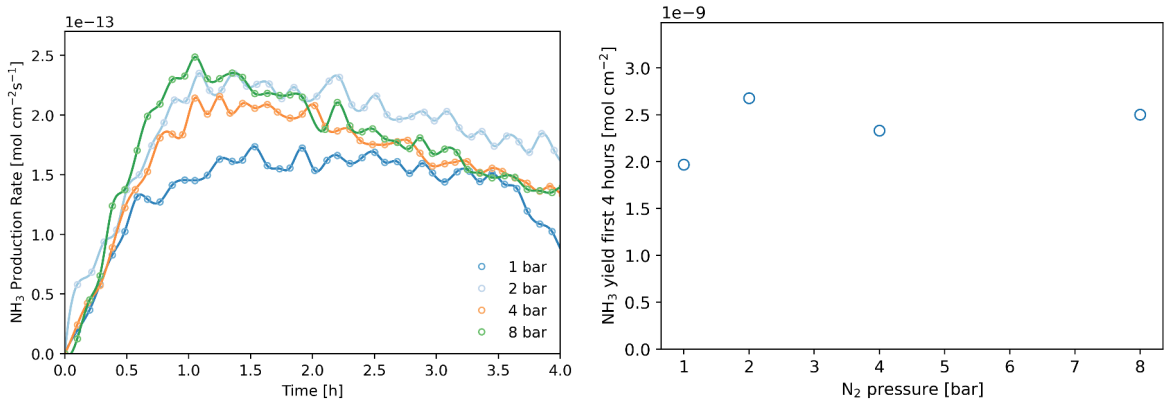

(a) NH_3 production rates at for high pressure measurements using samples prepared with the AJA process.

(b) NH_3 yield comparison for the first four hours of ammonia synthesis at higher pressures and flow rates.

Figure 4.5: Ammonia production measurements at different cell pressures. The larger cell was used with NiN deposited on the HPE with the AJA process. The temperature was 120 °C and the current density was 0.25 mA cm^{-2}.

One of the factors contributing to this result is the aforementioned constant N_2 mass flow rate used. The partial NH_3 pressure will stay constant when the pressure is increased constant N_2 mass flow rate, so a shift in equilibrium is not immediately expected for the NH_3 desorption step. Slower diffusion at higher pressures is also not expected to be problematic, as is calculated in section A.2. However, the slow convection causing significant delay in the removal of NH_3 could drive a rise in NH_3 concentration in the cell near the gas-electrode interface, shifting the equilibrium between desorption of NH_3 and re-adsorption from the gas phase. This could be a relevant equilibrium because NH_3 is the strongest adsorbing molecular species on Ni in the gas mixture of N_2, H_2, and NH_3. Hence, the later set of pressure experiments was conducted at greater N_2 mass flow rates, resulting in improved NH_3 production rates.

#	i [mA cm^{-2}]	E [V]	T [°C]	p [bar]	H_{perm} [mol cm^{-2} s^{-1}]	H_{perm} FE [%]	u_{H_2} [mol cm^{-2} s^{-1}]	u_{NH_3} [mol cm^{-2} s^{-1}]	Hydr. Eff. [%]	Tot. FE [%]
2	0.5	1.55	120	1	$1.73 \cdot 10^{-9}$	33.32	$8.63 \cdot 10^{-10}$	$1.49 \cdot 10^{-13}$	0.026	0.0086
11	0.5	1.55	120	2	$1.55 \cdot 10^{-9}$	29.98	$7.76 \cdot 10^{-10}$	$2.10 \cdot 10^{-13}$	0.041	0.0122
12	0.5	1.55	120	4	$1.52 \cdot 10^{-9}$	29.28	$7.58 \cdot 10^{-10}$	$1.84 \cdot 10^{-13}$	0.036	0.0107
13	0.5	1.46	120	8	$1.87 \cdot 10^{-9}$	36.11	$9.35 \cdot 10^{-10}$	2.24e-13	0.036	0.0130
14	0.25	1.30	120	8	$1.07 \cdot 10^{-9}$	41.47	$5.37 \cdot 10^{-10}$	$3.50 \cdot 10^{-14}$*	0.010*	0.0041*

Table 4.3: Large cell measurement results on the pressure dependence of H permeation and NH_3 production rate. Cells marked with * are NH_3 peaks recorded late in the experiment, and thus not representative of initial NH_3 production. The row numbers match the raw GC data table in Appendix C. Two or more injections are averaged per row.

While these results appear to show that N_2 adsorption is not the limiting step, these measurements were all conducted with a fresh HPE with full N loading. The connection between the reduction in N content of the HPE shown by XPS and the general decreasing pattern of the NH_3 production rate suggest that the amount of N available in the HPE determines the limit of achievable NH_3 production. At the start of the experiment, the abundance of pre-adsorbed N makes hydrogenation the limiting step as is reported elsewhere [98], temporarily obscuring the lack of N_2 adsorption required to maintain the N content of the HPE. Over time, as the N content dwindles, the reaction becomes limited by N_2 adsorption, which is the slowest elementary step. It is also expected that nitrogen adsorption itself decreases together with the N content, as N promotes the activity of Ni towards N_2 adsorption.

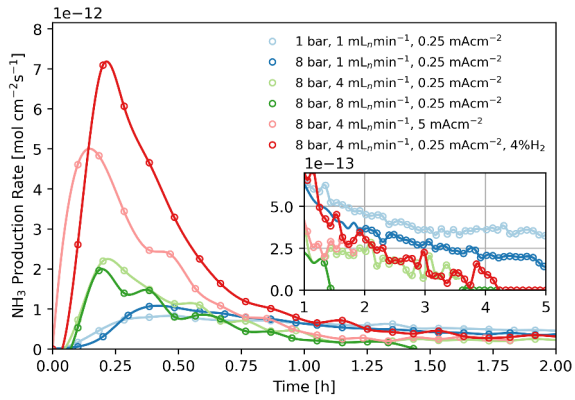

(a) NH_3 production rate during the first 2 hours of electrochemistry for different operating parameters. Inset: zoomed figure showing the production rate from 1 to 5 hours.

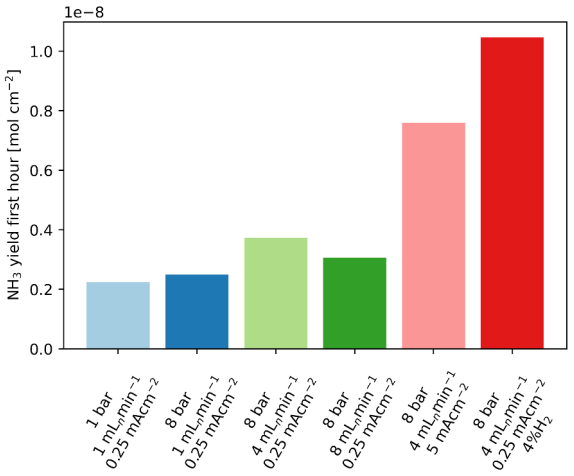

(b) Total NH_3 yields in the first hour of electrochemistry for different operating parameters.

Figure 4.6: NH_3 production rate and yield during high pressure experiments with the smaller cell and ALD prepared NiN. The current density used was 0.25 mA cm^{-2}, and the temperature was 120 °C. Different mass flow rates for N_2 were used, and one experiment was conducted with nitrogen gas blended with 4% H_2.

The second series of experiments relating to the pressure dependence of the ammonia production rate were conducted using the small cell ALD-prepared electrodes. These electrodes were confirmed to be free of contaminants through XPS measurements. It was decided that 2 and 4 bar measurements would not be conducted in favour of measurements at different mass flow rates for the feed gas. 8 bar was chosen as the high pressure setting to preserve comparability with the existing measurements. The current density was reduced in an effort to increase the stability of the measurements. Furthermore, some measurements were conducted using feed gas consisting of 96% N_2 and 4% H_2, because the hydrogen was expected to prevent oxidation of the catalyst surface. The NH_3 production rates for the first two hours and total yields for the first hour are given in Figure 4.6. High NH_3 production rate was generally accompanied by a significantly faster decline in the first hour, as shown in Figure 4.6a.

#	i [mA cm^{-2}]	E [V]	T [°C]	p [bar]	H_{perm} [mol cm^{-2} s^{-1}]	H_{perm} FE [%]	u_{H_2} [mol cm^{-2} s^{-1}]	u_{NH_3} [mol cm^{-2} s^{-1}]	Hydr. Eff. [%]	Tot. FE [%]
7	0.25	1.20	120	1	$4.21 \cdot 10^{-12}$	0.16	$9.50 \cdot 10^{-13}$	$7.69 \cdot 10^{-13}$	54.841	0.0890
15	0.25	1.23	120	8	$8.47 \cdot 10^{-11}$	3.27	$3.92 \cdot 10^{-11}$	$2.08 \cdot 10^{-12}$	7.371	0.2411
16	0.25	1.42	120	8	$1.06 \cdot 10^{-9}$	40.86	$5.27 \cdot 10^{-10}$	$1.78 \cdot 10^{-12}$	0.505	0.2063
17	2.5	1.55	120	8	$2.72 \cdot 10^{-9}$	10.48	$1.36 \cdot 10^{-9}$	$2.42 \cdot 10^{-13}$*	0.027*	0.0028*
18	5	1.63	120	8	$4.40 \cdot 10^{-9}$	8.49	$2.19 \cdot 10^{-9}$	$3.65 \cdot 10^{-12}$	0.249	0.0211

Table 4.4: Small cell measurement results on the pressure dependence of H permeation and NH_3 production rate. Cells marked with * are NH_3 peaks recorded late in the experiment, and thus not representative of initial NH_3 production. The row numbers match the raw GC data table in Appendix C. Two or more injections are averaged per row.

Firstly, it should be noted that the initial NH_3 production rate at atmospheric pressure with the small cell and ALD-prepared HPEs is about 5 times greater than that of the large cell with AJA-prepared HPEs, even though the current density was halved. This could in part be due to contamination on the AJA-prepared HPEs hampering the reaction, or by unidentified leaks in the system that allowed oxygen or other contaminants to enter the cell. The larger cell was only leak tested by comparing the inlet and outlet mass flow rates, and applying leak detection fluid. However, the main reason for the increased NH_3 production on ALD-prepared HPEs is the greater amount deposited N. This is a further sign that the limit for the NH_3 production rate is governed by the availability of N on the surface, which itself is limited by N adsorption.

The result at 8 bar pressure and 1 $mL_n\,min^{-1}$ mass flow rate is similar to the measurement with equal parameters conducted on the large cell, as the NH_3 production rate is initially slightly higher compared to atmospheric pressure, with the difference decreasing over time. However, upon increasing the N_2 mass flow rate to 4 $mL_n\,min^{-1}$, a 67% increase in ammonia production in the first hour is observed. Increasing the mass flow rate beyond 4 $mL_n\,min^{-1}$ does not increase the production rate further, and leads to a slightly lower total yield. This indicates that the N_2 residence time in the circuit is optimal to facilitate desorption and removal of NH_3 around 4 $mL_n\,min^{-1}$ at 8 bar or 0.5 $mL_n\,min^{-1}$ at atmospheric pressure. These observations combined could indicate that gaseous NH_3 can re-adsorb to the HPE reducing the rate of Ni_3N decomposition. At low flow rates, more NH_3 is present to re-adsorb, possibly explaining why the cell sustains a greater NH_3 production rate at lower flow rates.

Table 4.4 shows that an increase in pressure is generally followed by an increase in H permeation. This added permeation then yields a higher NH_3 production. It is therefore likely not the increased adsorption resulting from the greater number of nitrogen molecules impinging on the HPE surface that increases the NH_3 production. Rather, the increased H permeation arising from the higher hydrostatic pressure in the electrolyte compartment increases NH_3 production. The decreasing trend of the hydrogenation efficiency with increasing H permeation is also replicated at high pressure, as shown in Table 4.4.

The addition of 4% H_2 in the gas feed has a remarkable effect on the ammonia production rate during the first hour, because sufficient H is always available to convert the Ni_3N layer to NH_3. The peak production rate and yield in the first hour exceed a measurement with a 20-fold greater current without H_2 added to the gas feed. The average FE towards ammonia is 0.33% in this hour, noting that hydrogen from the gas feed can also participate in the reaction, so the FE is not properly defined. It appears that the supplied gaseous hydrogen does not just aid in reducing the catalytic surface of the HPE, yet also actively participates in the reaction towards ammonia, as was expected based on literature. It is suspected that the enhanced reaction rate due to presence of hydrogen results in faster depletion of the nitride layer. This explains the steeper downward slope that is observed along with the greater initial production rate.

An overarching pattern of Figure 4.6a is that greater initial production rate is sustained for shorter durations. This suggests that there is a deactivation mechanism at play that is connected to N content of the HPE. As shown in the inset of Figure 4.6a, after 3 hours, the sample that was run at atmospheric pressure maintains the highest production rate, on account of its Ni_3N layer being depleted slower than that of the other HPEs.

4.4. Electrodeposition

To further enhance the ammonia production rate, the surface area on the gas side of the HPE was increased through electrodeposition. Nickel foil was electroplated in three different electrodeposition solutions (Ni-sulfate based, Ni-sulfamate based, and a Watts solution). The electrochemical surface area of the samples was determined, and the most promising samples were further analysed using SEM. The nitriding processes were found not to impact the structure of the deposits. Finally, samples were tested in the ammonia synthesis cell to assess the production rate.

4.4.1. ECSA Measurements

Figure 4.7 shows the cyclic voltammetry plots of a sample before and after electroplating in a Watts solution at 5 mA cm^{-2} for 3 minutes. The y-scales are equal, making the increase in electric double layer capacity after electrodeposition apparent from the increased EDL (dis)charge current. Figure 4.7b has some imperfections, namely a slight shift towards more negative currents for all cycles, and (dis)charge currents that are not constant for each scan rate, and rather slightly increasing or decreasing depending on the sweep direction. The OCP is also different from that of Figure 4.7a. This could be due to presence of nickel oxides on the surface of the sample with electrodeposition, making the sample not in complete equilibrium with the solution. Nevertheless, the sweeps show clear separation for each scan rate and appear to be correlated linearly as expected. The current values of each sweep were taken at the OCP and plotted against the scan rate in Figure 4.8.

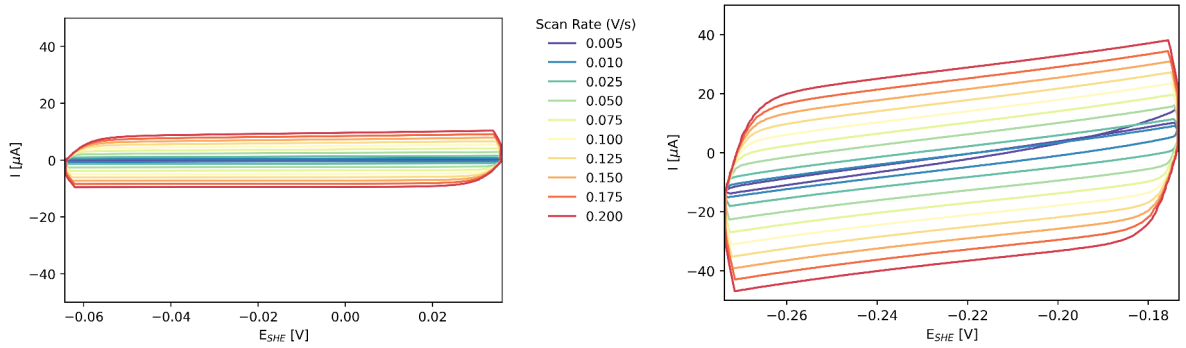

(a) Cyclic voltammetry before electrodeposition.

(b) Cyclic voltammetry after electrodeposition.

Figure 4.7: Cyclic voltammetry plots at scan rates between 5 and 200 mV s^{-1} of a Ni foil sample in 0.5M KOH. a: Bare Ni foil before electrodeposition. b: After electrodeposition in the Watts solution solution at 5 mA cm^{-2} for 3 minutes. The increase in EDL (dis)charge current in Figure 4.7b indicates the ECSA has increased during the electrodeposition.

During the preparation of the electrodeposited nanostructures various current densities and deposition durations were chosen. It was established that depositions with current densities and durations reported in literature [91] would not adhere to the nickel foil. This applied for example to a 5 min deposition at 30 mA cm^{-2} in the Ni-sulfate and Ni-sulfamate solutions. Curiously, a deposition with this set of parameters did adhere to the host metal when the Watts solution was used. The lack of adhesion could be due to an inadequate cleaning procedure, however, acetone and hydrochloric acid submergence with intermittent MilliQ rinsing is usually considered sufficient. The composition of the Watts solution appears to limit structural defects, thereby increasing adherence. It is suspected that the lack of adherence arose as a consequence of attempting to only electroplate a circular area that was enclosed by an EPDM gasket. Significant defects will be formed at the edge of the deposition area near the gasket, which can prompt the surrounding deposition to not adhere properly to the host metal. This phenomenon required limiting the deposition current and duration. In future studies, deposition times below 10 seconds at greater current densities could provide a desired combination of adherence and ECSA increase.

The quantification of the ECSA increase by electrodeposition is aided by Figure 4.8. The figure is meant to illustrate the principle, a summary of the ECSA results is given in Figure 4.9. For all three subfigures in Figure 4.8 the same deposition current density and duration were used with a different deposition solution. The slope of the pre-deposition ECSA measurement is similar for all three samples, as would be expected. Steeper post-depositions slopes indicate greater the ECSA and corresponding roughness factor. The roughness factors in Figure 4.9 are calculated by dividing the post-deposition slope by the average of all the pre-deposition slopes.

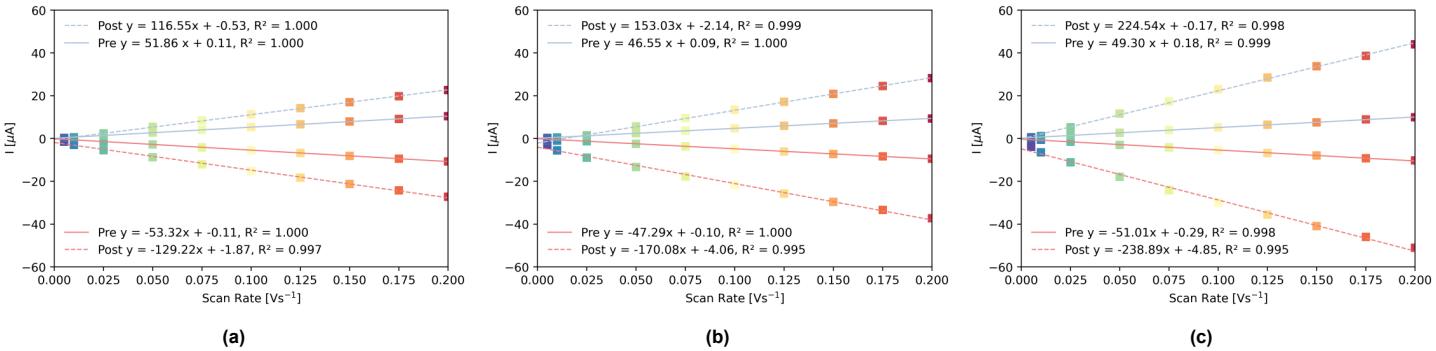

Figure 4.8: Electric double layer (dis)charge current of HPE samples at different scan rates for cycles of 50 mV above and below OCP. All samples displayed here were deposited at 5 mA cm^{-2} for 3 min. a: Ni-sulfamate solution. b: Watts solution. c: Ni-sulfate solution. The sweep directions are marked separately, upward in blue and downward in red. Linear least squares fits have been made through the data, with the resultant slopes given in the legends.

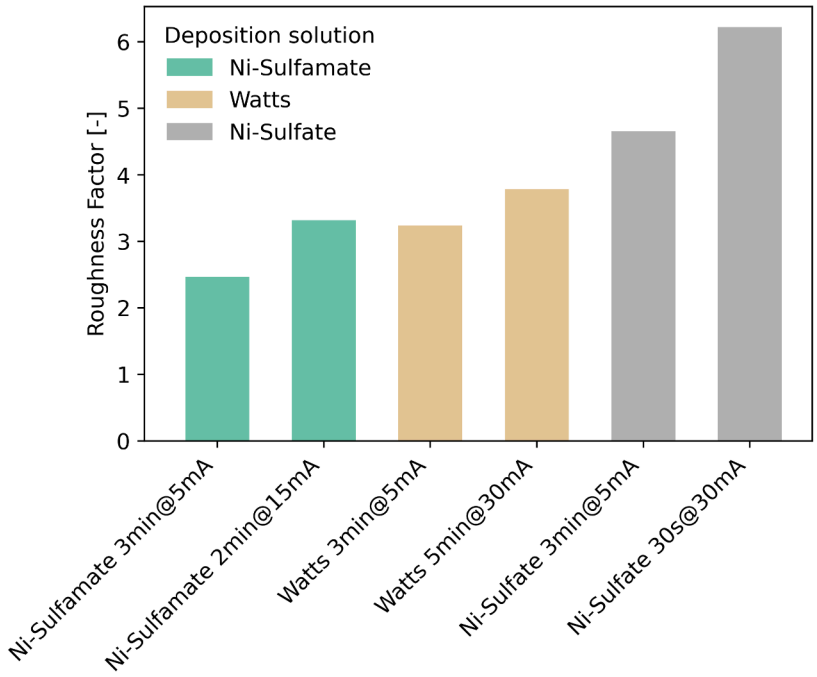

Figure 4.9: Roughness factors for HPE samples prepared with three electrodeposition solutions, each of which was deposited with 5 mA cm^{-2} as low current density option, and 15 or 30 mA cm^{-2} as the high current density option. The high current density options and their deposition times vary due to differing adherence of the deposition to the nickel foil.

The roughness factors of the depositions that properly adhered to the host metal are displayed in Figure 4.9. Depositions of 5 min at 30 mA cm^{-2} were taken as a starting point, although this only yielded satisfactory results in combination with the Watts solution. For the Ni-Sulfate solution the deposition time at 30 mA cm^{-2} had to be reduced to 30 s. This gave an adhering deposition, still including some visible imperfections that led to selection of other samples for further testing. Still, these parameters enlarged the chemical active surface area by a factor of 6.22, and the value is included here to show the effect of current density on the roughness factor. For the Watts solution, increasing the current density is relatively ineffective for increasing the ECSA. This indicates that the nickel structure growth is coarser, possibly owing to fewer defects being produced upon deposition. The Ni-sulfamate solution is the least able to produce adhering depositions, and also yields the smallest increase in ECSA for

the shared parameters of 3 min at 5 mA cm^{-2}. The Ni-Sulfate deposition with these parameters was selected for use in ammonia synthesis and comparison with the bare nickel electrode, considering its relatively high roughness factor of 4.65. Furthermore, from the electrodeposition thickness calculations in section A.3 it is concluded that a deposition of 3 min at 5 mA cm^{-2} with an assumed FE close to 100% has a thickness of 0.31 µm. This relatively small deposition thickness is advantageous for the hydrogen permeation.

4.4.2. SEM Images of Surface Morphology

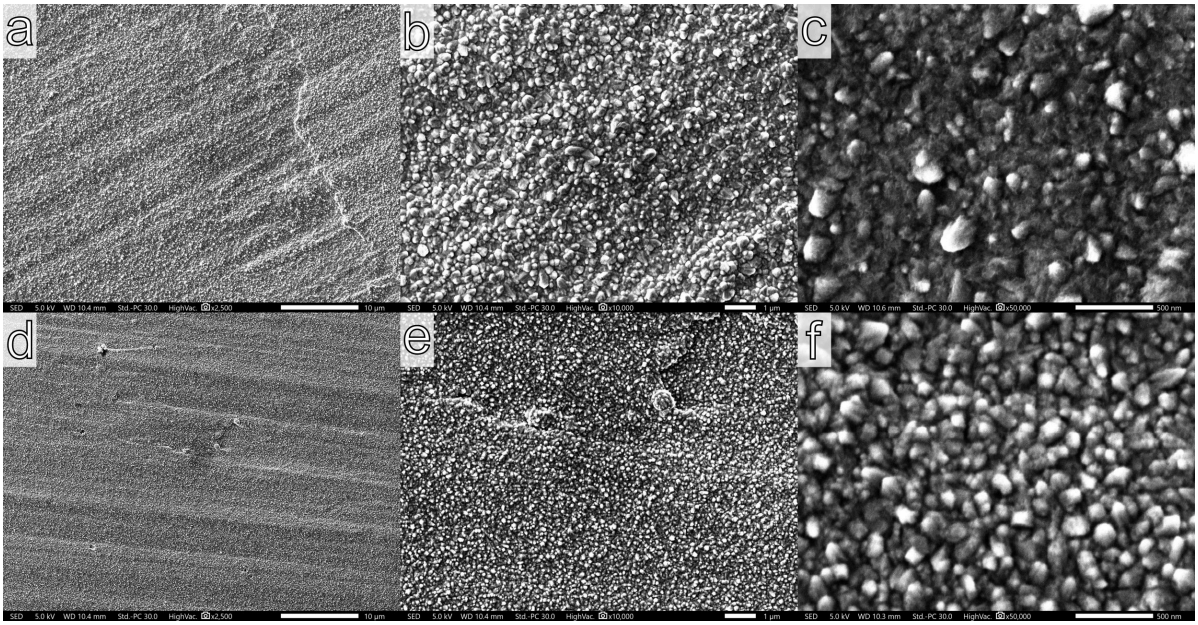

Figure 4.10: SEM images of HPE samples electroplated with the Ni-Sulfate electrodeposition solution at zoom levels of 2.500x (left), 10.000x (centre), and 50.000x (right). Top row (a-c): the sample was electroplated at a current density of 5 mA cm^{-2} for 3 min. Bottom row (d-f): the sample was electroplated at a current density of 30 mA cm^{-2} for 30 s.

The Ni-sulfate and Watts deposition solutions were selected for SEM analysis to determine the surface structure, and to verify whether the structures are affected by exposure to hydrogen and nitrogen plasma's during the nitriding process. SEM images of samples plated with the Ni-sulfate solution are displayed in Figure 4.10. A pillar structure is visible in both samples, albeit less developed for the lower current density sample when comparing the two rows. Some imperfections are visible in Figure 4.10d and e. Such irregularities would also appear for the sample with lower deposition current density, albeit less prevalently.

The depositions from the Watts solution are displayed in Figure 4.11, and show unexpectedly fine surface structures gives the measured roughness factors. The sample on the top row was plated for 3 min at 5 mA cm^{-2} similar to the top row in Figure 4.10, while showing greater resemblance to the sample plated at higher current density in Figure 4.10. The bottom row was plated at 30 mA cm^{-2} for a longer duration of 5 min, and these parameters create a significantly altered surface structure, with the pillars being replaced by unordered walls and pyramids.

The high current deposition in the Watts solution appears to have the finest surface structures out of the four samples, although this is not reflected in the roughness factor measurements. This might originate from the surface structure being electrically isolated from the host metal as a result of a greater number of defects in the bulk and the deposit-host metal interface, or possibly the images in Figure 4.10 were not able to capture fine nanostructures contributing to the ECSA. The confidence in the ECSA measurements is high considering that they were repeated. Still, another measurement of the fourth sample presented here in Figure 4.11d-f is recommended.

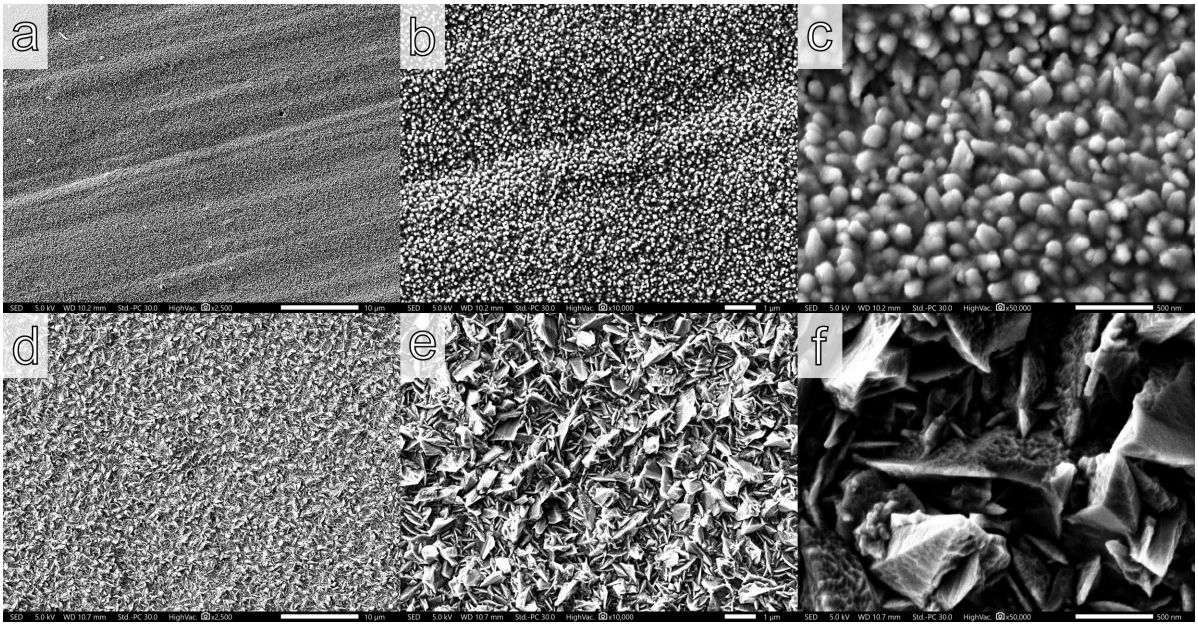

Figure 4.11: SEM images of samples electroplated with the Watts electrodeposition solution at zoom levels of 2.500x (left), 10.000x (centre), and 50.000x (right). Top row (a-c): sample was electroplated at a current density of 5 mA cm^{-2} for 3 min. Bottom row: sample was electroplated at a current density of 30 mA cm^{-2} for 5 min.

Figure 4.12a shows the surface of a bare nickel foil, compared to a sample with deposition in Figure 4.12b, to show the difference in surface roughness. Figure 4.12b was taken at the edge of the deposition area, where the gasket was located during the electrodeposition. There is an area of high elevation where the deposition would have grown up against the gasket material. The resulting imperfections in the surface are believed to have contributed to the lack of adhesion of the deposit in some samples. Figure 4.12c and d show a comparison between a freshly electroplated sample and an electroplated sample after the AJA nitriding process. The structure remains largely intact with no significant differences in surface roughness. The peaks of some pillars appear somewhat rounded, although this will not have significant impact on the ECSA.

4.4.3. Ammonia Production Rate

The ammonia production rate of the HPE with deposition from the Ni-sulfate solution at 5 mA cm^{-2} for 3 min was tested at atmospheric conditions with pure N_2 gas, and at a pressure of 8 bar with the 96% N_2 and 4% H_2 gas blend. The results are displayed in Figure 4.13. At atmospheric pressure the electroplated HPE briefly produces significantly more NH_3, while the production falls below that of bare Ni within two hours. The NH_3 yield of the electroplated sample during the first two hours is 37% higher. When inspecting the H permeation of the two measurements it becomes apparent that more H was permeating in the bare Ni measurement, inflating its NH_3 production rate. The result is different in Figure 4.13b, where the gas feed with 4% H_2 shows a considerable impact on the initial NH_3 production rate, the size of which grows by over 4 times from the bare nickel HPE to the electroplated HPE. This corresponds nearly exactly with the roughness factor of 4.65 of the sample. The high production subsides within an hour, yet the electroplated sample maintains an NH_3 production rate about 2 times that of the bare nickel sample, until the end of the measurement at 2.25h. The result indicates that more N can be deposited the electroplated surface by ALD, and this N is accessible for NH_3 synthesis, although the N content of the HPE is eventually depleted similarly to with the other measurements. It is unknown whether the surface morphology of the HPE increases N adsorption. Nevertheless, the 4.65 times greater ECSA appears to be insufficient to sustain the reaction at the previously reported NH_3 production rate [6].

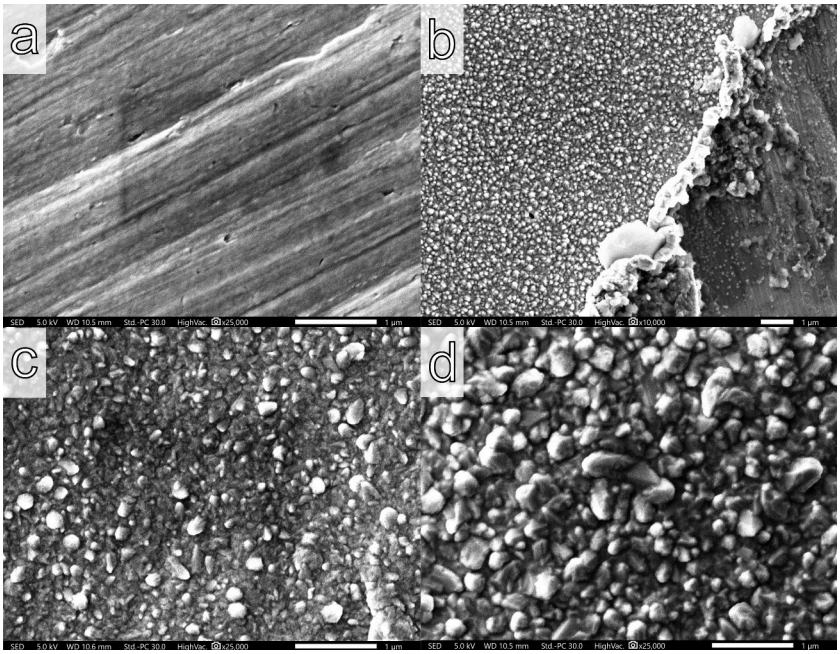

Figure 4.12: a: image of bare Ni foil at a magnification of 25.000x, for comparison with the electroplated samples. The surface is significantly flatter compared to electroplated surfaces, although some imperfections are visible. The diagonal lines are resultant from the manufacturing process of the foil. b: 10.000x magnified image of the edge of the electrodeposition area showing the imperfections induced by the gasket that encloses this area, and the difference between the deposited surface structure and the bare Ni surface. Sample was made with the Watts solution at 5 mA cm^{-2} for 3 min. c and d: Comparison of the surface structure before and after the AJA nitriding process at 25.000x magnification. No significant differences are visible, indicating that the nitriding process does not damage the surface structure or significantly decrease the ECSA. The sample was plated in the Ni-sulfate solution at 5 mA cm^{-2} for 3 min.

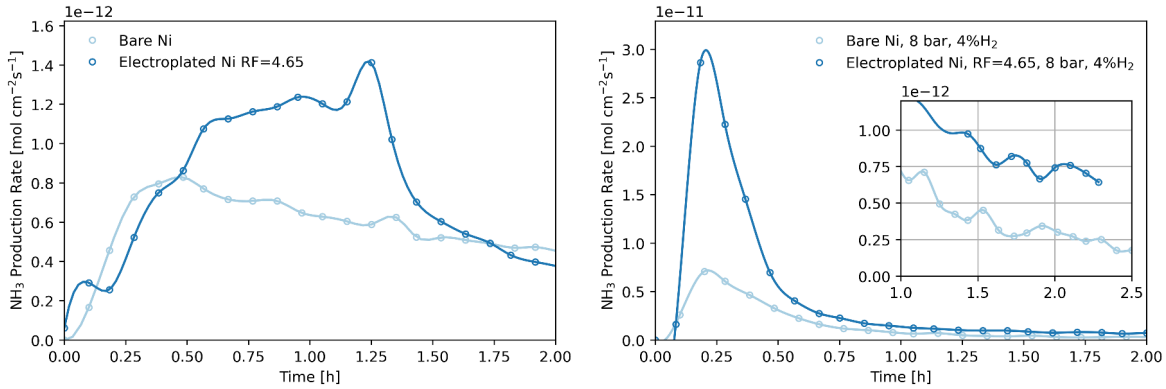

Figure 4.13: NH_3 production rate during the first two hours for a bare nickel sample and an electroplated sample, both nitrided using the ALD process. The electroplated sample had a roughness factor of 4.65. Current density was 0.25 mA cm^{-2} and the temperature was 120 °C. a: atmospheric pressure, 1 mL_n min^{-1} of N_2 feed gas. b: 8 bar 4 mL_n min^{-1} of 96% N_2 and 4% H_2 feed gas.

4.5. Deactivation Mechanism

While the different operating parameters could significantly increase the initial NH_3 production rate, the decreasing trend seems to be present at all times. The stability of the production rate appears to depend on the production rate itself: the greater the production, the steeper and earlier the decline. This means that some measurements with modest NH_3 production rates could be run for long durations. In some measurements with the small cell the NH_3 production appears to stabilise at $0.2 \cdot 10^{-12}$ mol cm^{-2} s^{-1}, although a slow decrease may still be present upon further inspection.

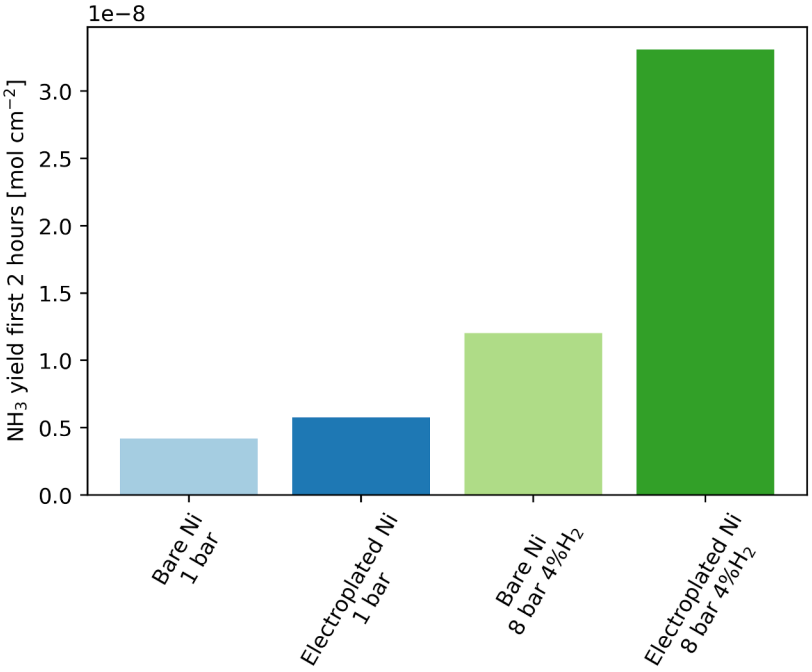

Figure 4.14: NH_3 yield during the first 2 hours of ammonia synthesis for a bare nickel electrode and an electroplated electrode with a roughness factor of 4.65, at one bar of pure nitrogen gas (blue bars) and 8 bar of nitrogen gas blended with 4% hydrogen (green bars). The current density was 0.25 mA cm^{-2} and the temperature was 120 °C in all measurements. The electroplated Ni performs 21% better than the bare Ni at 1 bar, while at 8 bar the improvement of the electroplated Ni over bare Ni is 280%.

DFT calculations by Abghoui et al. have marked the MvK mechanism on NiN as potentially unstable, due to insufficient stability of the adsorption sites, and a tendency for vacancies to migrate into the bulk [77] [99]. However, some form of reactivation has been observed during prolonged interruptions of the N_2 flow and current while maintaining the cell temperature at 120 °C. This phenomenon is displayed in Figure 4.15.

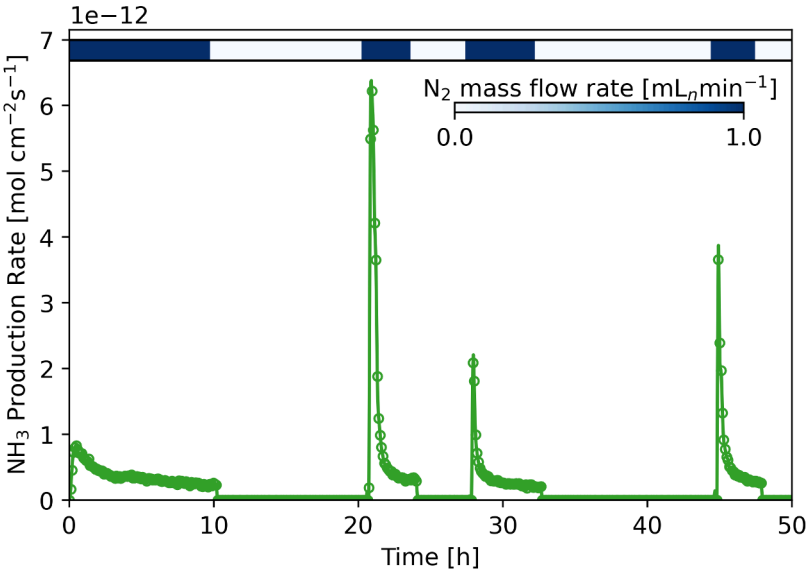

Figure 4.15: NH_3 production rate of a long duration measurement. The bar along the top indicates at when the N_2 flow was switched on, and the potentiostat was supplying a current density of 0.25 mA cm^{-2}. The temperature was kept at 120 °C for the full duration of the experiment. The first two injections after resuming N_2 flow are not displayed.

Upon restarting the N_2 flow and current at 20h into the experiment after a pause of 10h, a remarkable NH_3 production was observed for the first 30 to 45 minutes after the restart. This excludes the first two GC injections after the restart, since the flow and gas concentration were not stabilised. The initial peak in production rate was followed by a decreasing pattern. Surprisingly, the total NH_3 yield during the first measured 45 minutes after the restart was close to the extrapolation of the production rate before the 9h interruption. This is another indication that N adsorption does take place and regenerates the activity of the HPE surface, as the argon control experiment also confirmed. The absence of H could also help with the stability of the nitride layer, promoting reactivation. Still, the rate of the N adsorption is too slow to sustain an operating cell.

Another possibility that the reaction $7\,Ni + 2\,H_2O \longrightarrow Ni(OH)_2 + 2\,Ni_3H$ with a negative ΔG results in a small amount of H insertion into the HPE, as discussed earlier. This permeation rate during OCP conditions at high temperature could be close to rate of N adsorption on the gas side of the HPE, resulting in a balanced presence of N and H on the surface conducive to stable NH_3 synthesis without Ni_3N decomposition. The continuation of this process under OCP conditions and without gas flow, could result in a buildup of NH_3, which is measured as the gas flow is resumed.

5

Conclusions and Recommendations

5.1. Conslusions

1. What are the elementary steps in NH_3 synthesis with HPEs?
The elementary steps depend on the NRR reaction mechanism that is applicaple to the specific cell design and catalyst. For NRR using a Ni_3N HPE, this mechanism is the Mars-van Krevelen (MvK) mechanism. The associative variant of the MvK mechanism seems the most energetically favourable [36] [37] [38]. The elementary steps in this mechanism are as follows:

$$\begin{aligned}
MN + H^* &\rightleftharpoons MNH + {}^* \\
MNH + H^* &\rightleftharpoons MNH_2 + {}^* \\
MNH_2 + H^* &\rightleftharpoons MNH_3 + {}^* \\
MNH_3 &\rightleftharpoons M\square + NH_3(g) \\
M\square + N_2(g) &\rightleftharpoons MN{-}N^* \\
MN{-}N^* + H^* &\rightleftharpoons MN{-}NH^* + {}^* \\
MN{-}NH^* + H^* &\rightleftharpoons MN{-}NH_2{}^* + {}^* \\
MN{-}NH_2{}^* + H^* &\rightleftharpoons MN{-}NH_3{}^* + {}^* \\
MN{-}NH_3{}^* &\rightleftharpoons MN + NH_3(g)
\end{aligned} \tag{5.1}$$

1.1 Which elementary steps are limiting?
At a global level, N_2 adsorption to replenish N vacancies appears to be the limiting elementary step. However, the significance of this step for the NH_3 production rate is initially low, as there is sufficient N available in the Ni_3N lattice. Under high availability of lattice N, the first hydrogenation step is limiting. As lattice N is consumed in the reaction towards NH_3, replenishment of the N vacancies gains importance and it being limiting is signified by the decreasing NH_3 production rate over time. The N vacancy replenishment step is given below.

$$M\square + N_2(g) \rightleftharpoons MN{-}N^* \tag{5.2}$$

The rate of this elementary step was not determined experimentally. An HPE without the nitriding treatment would not produce measurable amounts of NH_3, giving an indication that for clean Ni the N adsorption rate is below the detection threshold of the GC. The N_2 absorption rate is likely higher on Ni_3N as opposed to pure Ni, although still below the rate of other elementary steps. Apart from the decreasing NH_3 production rate, this assessment is supported by XPS depth profiling showing a marked decrease N content of the HPE after operation on both the surface and sub-surface, demonstration of high initial rates of N hydrogenation and NH_3 desorption that exclude these steps from being limiting, and literature demonstrating the instability of nickel nitride at elevated temperatures, especially in the presence of hydrogen.

1.2 If present, what is the mechanism of deactivation?
The main mechanism of deactivation is depletion of the Ni_3N layer due to the rate of vacancy replenishment not equalling the combined rate of two processes contributing to nitride decomposition, these being the conversion of lattice N to NH_3 and possibly to N_2. The depletion of the Ni_3N layer is shown on the XPS depth profiles, where the HPE surface N1s peak is severely reduced after the operation at high temperature. The decomposition of Ni_3N to N_2 is expected to occur at elevated temperatures, although the rate of this process under the experimental conditions was not quantified through analysis of the outlet gas for N_2. However, the XPS profiles do indicate the presence of a reaction besides hydrogenation to NH_3. Using H_2 in the feed gas accelerates the Ni_3N decomposition towards NH_3, shown by the remarkable improvements in initial production rate. Reduced presence of N near the surface is expected to further reduce HPE's ability to activate N_2.

The nitride layer appears to be able to regenerate itself if H permeation is minimised by setting the potentiostat to OCP and stopping the inlet gas flow. The minimal NH_3 formation under these conditions appears to enable N adsorption to take place effectively. Furthermore, the increased presence of NH_3 near the HPE under these conditions perhaps results in increased re-adsorption of NH_3, and possibly formation of Ni_3N. If this is the case, it would also explain lower gas flow rates having a slightly more stable NH_3 production rate. The instability does return upon resuming the gas flow and current.

2. How does increasing pressure in an NH_3 synthesis cell with an HPE affect the NH_3 production rate and faradaic efficiency?
The initial NH_3 production rate is increased by up to 67% by a pressure increase from 1 to 8 bar. Most of this increase is attributed to a higher H permeation rate enabling increased NH_3 production from the abundant N in the nitride layer. The details on the elementary steps are given in 2.3.

2.1 How can an NH_3 synthesis cell with an HPE be pressurised?
The use of back pressure regulators solves the challenge of pressure differential across the HPE, potentially causing ruptures. It facilitates the maintaining of the pressure while simultaneously allowing a fixed mass flow rate of gas to exit the cell for GC analysis. PEEK is suitable for pressures of up to 15 bar at 120 °C, although stainless steel is a preferred option for higher pressures. Furthermore, the implementation of check valves and a moisture trap in the circuit prevent electrolyte from reaching the GC in the event of an HPE rupture.

2.2 How can the GC measuring equipment be used with a pressurised cell?
Maintaining the inlet gas mass flow rate while increasing the pressure decreases the volumetric flow rate of the gas. This increases the residence time of N_2 molecules in the circuit, causing measurement delays, while increasing the mass flow rate proportionally with the pressure results in dilution of the ammonia peak, reducing measurement accuracy. Maintaining $1\,mL_n\,min^{-1}$ at elevated pressure also revealed differing retention times of H_2 and NH_3 in the gas circuit before the GC, indicating a degree of NH_3 adsorption despite the use of an inert coating. At 8 bar, the optimal mass flow rate was identified as $4\,mL_n\,min^{-1}$, giving half the volumetric flow rate of $1\,mL_n\,min^{-1}$ at 1 bar.

2.3 How are the elementary steps influenced by an increase in pressure?
With N_2 adsorption established as the limiting elementary step, increasing the N_2 pressure becomes the default strategy to increase the production rate and faradaic efficiency. A 36% increase in initial production was observed the larger cell by raising the pressure to 2 bar, yet further increases showed no positive effect. The reason for this is presumed to be that the initial NH_3 production is not limited by N_2 adsorption due to the abundance of pre-deposited N on the HPE. The adsorption rate is expected to be a few orders of magnitude slower than the other elementary steps, making an 8 bar pressure increase insufficient to accelerate N_2 adsorption to a rate that will sustain the reaction.

Increasing pressure has a mildly positive effect on H permeation, as expected. For the small cell, the greater initial NH_3 production at elevated pressures can be explained by the increase in H permeation, hydrogenating nitrogen from the Ni_3N layer at an increased rate. This aligns with the observed pattern of increased initial NH_3 production rate being accompanied by earlier and sharper decrease over time.

3. What are other strategies to improve the NH_3 production rate and faradaic efficiency in a cell with an HPE, apart from an increase in pressure?
Apart from increasing the temperature and modifying the electrode surface morphology mentioned below, alloying, doping, and other forms of combining catalyst materials are identified as strategies to increase the activity, stability, and selectivity of HPEs. Combining species that each offer activity towards one of the elementary steps into a catalyst potentially enables breaking of the scaling relations. Nickel could be replaced by another element or an alloy to increase H permeability, although this is of low priority, since most of the permeated H is not hydrogenated to NH_3. The priority should be to develop a more stable and active nitride surface, through combination of Ni_3N with another nitride or a dopant that promotes N_2 activation and adsorption, such as potassium or niobium nitride.

3.1 How does increasing the temperature affect the faradaic efficiency and production rate of ammonia production?
A temperature increase improves the permeability of the HPE through the Arrhenius law of bulk H diffusion. This is reflected in the results that show improvement in H permeation with a factor of 33 upon increasing temperature from 20 to 120 °C, confirming earlier research [6]. The permeation FE is improved significantly, yet not all permeating H can take part in the hydrogenation reaction to ammonia, sharply decreasing the hydrogenation efficiency. The Total FE still shows improvement at higher temperatures.

At 120 °C the stability of the nitride layer is reduced, possibly increasing unintended Ni_3N decomposition to N_2. This should be confirmed with a control experiment.

3.2 How does modifying the electrode surface morphology affect the ammonia production rate?
A facile method was developed to increase the ECSA of one side of the HPE by a factor of 4.65. The surface structure was not affected by exposure to hydrogen and nitrogen. The electroplated HPE showed the increased initial NH_3 production of up to 4 times, corresponding to its increase in ECSA and representing the highest instantaneous NH_3 production rate across the current and earlier studies. The chromatogram of the injection with the greatest NH_3 concentration is given in Figure B.2. Unfortunately, any increase in nitrogen adsorption due to the enhanced ECSA was not enough to sustain the reaction.

5.2. Recommendations

Despite the improvements realised in this project, a reproduction of the stable NH_3 production [6] is strongly desired. NH_3 production by consumption of the nitride layer does not constitute catalytic reduction of N_2, and thus future experiments should isolate these reactions under the different conditions, possibly with isotope labelling. Isotope labelling has been conducted before, proving a catalytic pathway from N_2 to NH_3 using Ni_3N [5], yet these experiments should be revisited at 120 °C with a focus on the stability over several hours. A stable production will also greatly simplify measurements, because parameters could be changed during an experiment without planning without the result being affected by an inevitable downward trend. With this in mind, the main objective should be stabilising the reaction rate.

5.2.1. HPE Improvements

The recommended approach is to gain more insight into the composition of the nitride layer and its evolution during the operation. An estimation of the N content was made here, while a rigorous measurement would be preferred to accurately determine the amount of N atoms on the HPE before operation. The surface could be inspected with x-ray diffraction (XRD) to determine the crystal structure of the nitride. Next, the possibility of Ni_3N decomposition to N_2 should be investigated, by feeding the cell with an inert gas other than nitrogen, and preventing hydrogen from permeating through the HPE. Heating the cell and analysing the gas composition using GC will show whether Ni_3N decomposes to N_2. If this would be the case, it would explain part of the loss of surface nitride. Overall, attention should be given to tracking the amount of N on the HPE surface and quantifying the existing streams of N to and from the HPE surface.

It is possible that the stable production rate of NH_3 was facilitated in a small window of operational parameters, and that this window had not been found since. The AJA-based nitriding process is an unknown factor in this consideration, considering that the samples that were capable of stable NH_3 production could also have trace amounts of other elements on them, which is impossible to verify.

In any case, applying dopants should be pursued as a method to increase the stability and activity of the HPE. It is expected that single atom dopants or regions of alternating elements on the surface can increase the activity, because different elements may promote different elementary steps. An additional catalyst component should be added to the current nickel nitride material, for instance potassium, a nitride based on niobium, lanthanum or another element that is marked as favourable towards nitrogen adsorption by computational studies [38]. Dispersing the elements across the surface without creating full coverage allows both elements to contribute to the reaction, as has been achieved in other studies [80]. Furthermore, partial exposure of the nickel will ensure minimal effect on the H permeability of the HPE.

5.2.2. Pressure Improvements

Increasing the pressure in the cell has not been disqualified as a means to improve the stability of NH_3 production in an HPE cell for NRR. The limited improvements must be seen in the context of a generally decreasing NH_3 production over time, caused by limited N vacancy replenishment. This means that the true N adsorption limited production rate could be significantly below the NH_3 production rate observed in the first hours of NH_3 production. If this is correct, the pressure would have to be raised further, to between 50 and 150 bar, still below Haber-Bosch conditions, yet more likely to reveal the improvement in N adsorption rate.

It is recommended to design a stainless steel cell for operation with an HPE at pressures above 8 bar. Not only will this be necessary for pressures above 15 bar due to the mechanical limitations of the PEEK cells, the IDEX flangeless fittings have also shown to be unsuitable for high pressure and temperature applications. The cell and connections should be inert to ammonia, possibly through application of the same coating as was used for the gas lines and back pressure regulators in this research.

References

[1] K. Calvin et al. *IPCC, 2023: Climate Change 2023: Synthesis Report, Summary for Policymakers. Contribution of Working Groups I, II and III to the Sixth Assessment Report of the Intergovernmental Panel on Climate Change [Core Writing Team, H. Lee and J. Romero (eds.)]. IPCC, Geneva, Switzerland.* Ed. by P. Arias et al. July 2023, pp. 1–34. DOI: 10.59327/ipcc/ar6-9789291691647.001.

[2] IEA. *Ammonia Technology Roadmap – Analysis*. 2020.

[3] M. Appl. *Ammonia, 1. Introduction*. Wiley, Oct. 2011. ISBN: 9783527306732. DOI: 10.1002/14356007.a02_143.pub3.

[4] Y. H. Moon et al. "Recent advances in electrochemical nitrogen reduction reaction to ammonia from the catalyst to the system". en. In: *Catalysts* 12.9 (Sept. 2022), p. 1015.

[5] D. Ripepi et al. "Ammonia Synthesis at Ambient Conditions via Electrochemical Atomic Hydrogen Permeation". In: *ACS Energy Letters* 6.11 (Oct. 2021), pp. 3817–3823. ISSN: 2380-8195. DOI: 10.1021/acsenergylett.1c01568.

[6] D. Ripepi, H. Schreuders, F. M. Mulder. "Effect of Temperature and H Flux on the NH3 Synthesis via Electrochemical Hydrogen Permeation". In: *ChemSusChem* 16.13 (May 2023). ISSN: 1864-564X. DOI: 10.1002/cssc.202300460.

[7] Lazard. *Levelised Cost of Energy Analysis - Version 16.0*. Apr. 2023.

[8] D. R. MacFarlane et al. "A roadmap to the ammonia economy". en. In: *Joule* 4.6 (June 2020), pp. 1186–1205. DOI: 10.1016/j.joule.2020.04.004.

[9] V. Smil. "Nitrogen and Food Production: Proteins for Human Diets". In: *AMBIO: A Journal of the Human Environment* 31.2 (Mar. 2002), pp. 126–131. DOI: 10.1579/0044-7447-31.2.126.

[10] C. Kurien, M. Mittal. "Utilization of green ammonia as a hydrogen energy carrier for decarbonization in spark ignition engines". In: *International Journal of Hydrogen Energy* 48.74 (Aug. 2023), pp. 28803–28823. ISSN: 0360-3199. DOI: 10.1016/j.ijhydene.2023.04.073.

[11] H.-L. Du et al. "Critical Assessment of the Electrocatalytic Activity of Vanadium and Niobium Nitrides toward Dinitrogen Reduction to Ammonia". In: *ACS Sustainable Chemistry Engineering* 7.7 (Feb. 2019), pp. 6839–6850. ISSN: 2168-0485. DOI: 10.1021/acssuschemeng.8b06163.

[12] D. Ripepi, H. Schreuders, F. M. Mulder. "Effect of Temperature and H Flux on the NH3 Synthesis via Electrochemical Hydrogen Permeation". In: *ChemSusChem* 16.13 (May 2023). ISSN: 1864-564X. DOI: 10.1002/cssc.202300460.

[13] J. W. Erisman et al. "How a century of ammonia synthesis changed the world". en. In: *Nat. Geosci.* 1.10 (Oct. 2008), pp. 636–639. DOI: 10.1038/ngeo325.

[14] K. H. R. Rouwenhorst, A. S. Travis, L. Lefferts. "1921–2021: A Century of Renewable Ammonia Synthesis". In: *Sustainable Chemistry* 3.2 (Apr. 2022), pp. 149–171. DOI: 10.3390/suschem3020011.

[15] W. Avery. "A role for ammonia in the hydrogen economy". In: *International Journal of Hydrogen Energy* 13.12 (1988), pp. 761–773. ISSN: 0360-3199. DOI: 10.1016/0360-3199(88)90037-7.

[16] F. M. Mulder. "Implications of diurnal and seasonal variations in renewable energy generation for large scale energy storage". In: *Journal of Renewable and Sustainable Energy* 6.3 (May 2014). ISSN: 1941-7012. DOI: 10.1063/1.4874845.

[17] O. Hatfield. *Ammonia Energy Association - Review of global ammonia supply*. 2020.

[18] A. M. Bazzanella, F. Ausfelder. *Technology Study: Low Carbon Energy and Feedstock for the European Chemical Industry*. https://dechema.de/dechema_media/Technology_study_Low_carbon_energy_and_feedstock_for_the_European_chemical_industry-p-20002750.pdf. Dechema: Gesellschaft für Chemische Technik und Biotechnologie e.V, 2017.

[19] K. H. R. Rouwenhorst et al. *Ammonia, 4. Green Ammonia Production*. May 2020. DOI: 10.1002/14356007.w02_w02.

[20] V. Smil. "Detonator of the population explosion". In: *Nature* 400.6743 (July 1999), pp. 415–415. ISSN: 1476-4687. DOI: 10.1038/22672.

[21] T. R. Malthus. *Essay on the Principle of Population: The 1803 Edition*. Ed. by S. C. Stimson. Yale University Press, Oct. 2019. ISBN: 9780300231892. DOI: 10.12987/9780300231892.

[22] W. Crookes. "Address of the President Before the British Association for the Advancement of Science, Bristol, 1898". In: *Science* 8.200 (1898), pp. 561–575. ISSN: 00368075, 10959203.

[23] K. H. Rouwenhorst, A. G. V. der Ham, L. Lefferts. "Beyond Haber-Bosch: The renaissance of the Claude process". In: *International Journal of Hydrogen Energy* 46.41 (June 2021), pp. 21566–21579. DOI: 10.1016/j.ijhydene.2021.04.014.

[24] G. Ertl. "Reactions at Surfaces: From Atoms to Complexity (Nobel Lecture)". In: *Angewandte Chemie International Edition* 47.19 (Apr. 2008), pp. 3524–3535. DOI: 10.1002/anie.200800480.

[25] K. Rouwenhorst et al. "Ammonia Production Technologies". In: *Techno-Economic Challenges of Green Ammonia as an Energy Vector*. Elsevier, 2021, pp. 41–83. ISBN: 9780128205600. DOI: 10.1016/b978-0-12-820560-0.00004-7.

[26] M. Mori et al. "Integral Characteristics of Hydrogen Production in Alkaline Electrolysers". In: *Strojniški vestnik – Journal of Mechanical Engineering* 10.59 (Oct. 2013), pp. 585–594. ISSN: 0039-2480. DOI: 10.5545/sv-jme.2012.858.

[27] J. Newman, N. P. Balsara. *Electrochemical systems*. en. 4th ed. The ECS Series of Texts and Monographs. Nashville, TN: John Wiley & Sons, Jan. 2021.

[28] G. Qing et al. "Recent advances and challenges of electrocatalytic N2 reduction to ammonia". en. In: *Chem. Rev.* 120.12 (June 2020), pp. 5437–5516. DOI: 10.1021/acs.chemrev.9b00659.

[29] N. Bauer. "Theoretical Pathways for the Reduction of N2 Molecules in Aqueous Media: Thermodynamics of N2Hn1". In: *The Journal of Physical Chemistry* 64.7 (July 1960), pp. 833–837. ISSN: 1541-5740. DOI: 10.1021/j100836a001.

[30] X. Cui, C. Tang, Q. Zhang. "A Review of Electrocatalytic Reduction of Dinitrogen to Ammonia under Ambient Conditions". In: *Advanced Energy Materials* 8.22 (May 2018). ISSN: 1614-6840. DOI: 10.1002/aenm.201800369.

[31] C. J. M. van der Ham, M. T. M. Koper, D. G. H. Hetterscheid. "Challenges in reduction of dinitrogen by proton and electron transfer". In: *Chem. Soc. Rev.* 43.15 (2014), pp. 5183–5191. ISSN: 1460-4744. DOI: 10.1039/c4cs00085d.

[32] M. A. Shipman, M. D. Symes. "Recent progress towards the electrosynthesis of ammonia from sustainable resources". In: *Catalysis Today* 286 (May 2017), p. 58. ISSN: 0920-5861. DOI: 10.1016/j.cattod.2016.05.008.

[33] E. Skúlason et al. "A theoretical evaluation of possible transition metal electro-catalysts for N_2 reduction". In: *Phys. Chem. Chem. Phys.* 14.3 (2012), pp. 1235–1245. DOI: 10.1039/c1cp22271f.

[34] P. Mars, D. van Krevelen. "Oxidations carried out by means of vanadium oxide catalysts". In: *Chemical Engineering Science* 3 (1954), pp. 41–59. ISSN: 0009-2509. DOI: 10.1016/s0009-2509(54)80005-4.

[35] C. Doornkamp, V. Ponec. "The universal character of the Mars and Van Krevelen mechanism". In: *Journal of Molecular Catalysis A: Chemical* 162.1–2 (Nov. 2000), pp. 19–32. ISSN: 1381-1169. DOI: 10.1016/s1381-1169(00)00319-8.

[36] A. Daisley, J. Hargreaves. "Metal nitrides, the Mars-van Krevelen mechanism and heterogeneously catalysed ammonia synthesis". In: *Catalysis Today* 423 (Nov. 2023), p. 113874. ISSN: 0920-5861. DOI: 10.1016/j.cattod.2022.08.016.

[37] Y. Abghoui, E. Skúlason. "Computational Predictions of Catalytic Activity of Zincblende (110) Surfaces of Metal Nitrides for Electrochemical Ammonia Synthesis". In: *The Journal of Physical Chemistry C* 121.11 (Mar. 2017), pp. 6141–6151. ISSN: 1932-7455. DOI: 10.1021/acs.jpcc.7b00196.

[38] Y. Abghoui, E. Skúlason. "Electrochemical synthesis of ammonia via Mars-van Krevelen mechanism on the (111) facets of group III–VII transition metal mononitrides". In: *Catalysis Today* 286 (May 2017), pp. 78–84. ISSN: 0920-5861. DOI: 10.1016/j.cattod.2016.06.009.

[39] R. Battino, T. R. Rettich, T. Tominaga. "The Solubility of Nitrogen and Air in Liquids". In: *Journal of Physical and Chemical Reference Data* 13.2 (Apr. 1984), pp. 563–600. ISSN: 1529-7845. DOI: 10.1063/1.555713.

[40] S. M. Stratton, S. Zhang, M. M. Montemore. “Addressing complexity in catalyst design: From volcanos and scaling to more sophisticated design strategies”. In: *Surface Science Reports* 78.3 (Aug. 2023), p. 100597. ISSN: 0167-5729. DOI: 10.1016/j.surfrep.2023.100597.

[41] B. Yang et al. “Recent progress in electrochemical synthesis of ammonia from nitrogen: strategies to improve the catalytic activity and selectivity”. In: *Energy &amp Environmental Science* 14.2 (2021), pp. 672–687. DOI: 10.1039/d0ee02263b.

[42] M. Salciccioli, Y. Chen, D. G. Vlachos. “Density Functional Theory-Derived Group Additivity and Linear Scaling Methods for Prediction of Oxygenate Stability on Metal Catalysts: Adsorption of Open-Ring Alcohol and Polyol Dehydrogenation Intermediates on Pt-Based Metals”. In: *The Journal of Physical Chemistry C* 114.47 (Nov. 2010), pp. 20155–20166. ISSN: 1932-7455. DOI: 10.1021/jp107836a.

[43] E. Protopopoff, P. Marcus. “Surface Effects on Hydrogen Entry into Metals”. In: *Corrosion Mechanisms in Theory and Practice*. CRC Press, Aug. 2011, pp. 117–160. DOI: 10.1201/b11020-6.

[44] A. Turnbull. “Hydrogen diffusion and trapping in metals”. In: *Gaseous Hydrogen Embrittlement of Materials in Energy Technologies*. Elsevier, 2012, pp. 89–128. DOI: 10.1533/9780857095374.1.89.

[45] C. K. Gupta. *Chemical Metallurgy: Principles and Practice*. Wiley, July 2003. ISBN: 9783527602001. DOI: 10.1002/3527602003.

[46] A. Caravella, G. Barbieri, E. Drioli. “Concentration polarization analysis in self-supported Pd-based membranes”. In: *Separation and Purification Technology* 66.3 (May 2009), pp. 613–624. ISSN: 1383-5866. DOI: 10.1016/j.seppur.2009.01.008.

[47] S. A. Steward. *Review of Hydrogen Isotope Permeability Through Materials*. Aug. 1983. DOI: 10.2172/5277693.

[48] Y. Li et al. “Mechanism and Evaluation of Hydrogen Permeation Barriers: A Critical Review”. In: *Industrial Engineering Chemistry Research* 62.39 (Aug. 2023), pp. 15752–15773. ISSN: 1520-5045. DOI: 10.1021/acs.iecr.3c02259.

[49] A. Santucci, S. Tosti, A. Basile. “Alternatives to palladium in membranes for hydrogen separation: nickel, niobium and vanadium alloys, ceramic supports for metal alloys and porous glass membranes”. In: *Handbook of Membrane Reactors*. Elsevier, 2013, pp. 183–217. DOI: 10.1533/9780857097330.1.183.

[50] W. M. Robertson. “Hydrogen Permeation, Diffusion and Solution in Nickel”. In: *International Journal of Materials Research* 64.6 (June 1973), pp. 436–443. ISSN: 1862-5282. DOI: 10.1515/ijmr-1973-640606.

[51] G. Rao, C. Rao. “Adsorption of nitrogen on clean and modified single-crystal Ni surfaces”. In: *Applied Surface Science* 45.1 (Aug. 1990), pp. 65–69. ISSN: 0169-4332. DOI: 10.1016/0169-4332(90)90021-q.

[52] M. Grunze et al. “Molecular and dissociative chemisorption of N2 on Ni(110)”. In: *Surface Science* 89.1-3 (Jan. 1979), pp. 381–390. DOI: 10.1016/0039-6028(79)90624-1.

[53] D. Ripepi et al. “In Situ Study of Hydrogen Permeable Electrodes for Electrolytic Ammonia Synthesis Using Near Ambient Pressure XPS”. In: *ACS Catalysis* 12.21 (Oct. 2022), pp. 13781–13791. ISSN: 2155-5435. DOI: 10.1021/acscatal.2c03609.

[54] T. Smith. “Effect of Surface Coverage and Temperature on the Sticking Coefficient”. In: *The Journal of Chemical Physics* 40.7 (Apr. 1964), pp. 1805–1812. ISSN: 1089-7690. DOI: 10.1063/1.1725409.

[55] F. Bozso. “Interaction of nitrogen with iron surfaces I. Fe(100) and Fe(111)”. In: *Journal of Catalysis* 49.1 (July 1977), pp. 18–41. DOI: 10.1016/0021-9517(77)90237-8.

[56] M. Muhler, F. Rosowski, G. Ertl. “The dissociative adsorption of N2 on a multiply promoted iron catalyst used for ammonia synthesis: a temperature-programmed desorption study”. In: *Catalysis Letters* 24.3-4 (1994), pp. 317–331. DOI: 10.1007/bf00811804.

[57] G. Ertl, S. Lee, M. Weiss. “Kinetics of nitrogen adsorption on Fe(111)”. In: *Surface Science* 114.2–3 (Feb. 1982), pp. 515–526. ISSN: 0039-6028. DOI: 10.1016/0039-6028(82)90702-6.

[58] G. Wedler, G. Alshorachi. “Adsorption of Nitrogen on Polycrystalline Nickel Films between 77 K and 333 K”. In: *Berichte der Bunsengesellschaft für physikalische Chemie* 84.3 (Mar. 1980), pp. 277–281. DOI: 10.1002/bbpc.19800840317.

[59] C. R. Brundle. “XPS and UPS studies of the interaction of nitrogen containing molecules with nickel: The use of binding energy patterns and relative intensities to diagnose surface species”. In: *Journal of Vacuum Science and Technology* 13.1 (Jan. 1976), pp. 301–309. ISSN: 0022-5355. DOI: 10.1116/1.568833.

[60] V. Zhukov, A. Ferstl, K. D. Rendulic. “Interaction of nitrogen with the Ni(111) plane.” In: *Fizika A* 4.1 (Jan. 1995), pp. 271–277.

[61] G. Ertl, S. Lee, M. Weiss. “Adsorption of nitrogen on potassium promoted Fe(111) and (100) surfaces”. In: *Surface Science* 114.2–3 (Feb. 1982), pp. 527–545. ISSN: 0039-6028. DOI: 10.1016/0039-6028(82)90703-8.

[62] G. Rao, K. Prabhakaran, C. Rao. “Nitrogen adsorbed on clean and promoted Ni surfaces”. In: *Surface Science* 176.1-2 (Oct. 1986), pp. L835–L840. DOI: 10.1016/0039-6028(86)90157-3.

[63] I. Bassignana et al. “Adsorption and thermal decomposition of ammonia on a Ni(110) surface: Isolation and identification of adsorbed NH2 and NH”. In: *Surface Science* 175.1 (Sept. 1986), pp. 22–44. ISSN: 0039-6028. DOI: 10.1016/0039-6028(86)90081-6.

[64] R. MCCABE. “Kinetics of ammonia decomposition on nickel”. In: *Journal of Catalysis* 79.2 (Feb. 1983), pp. 445–450. ISSN: 0021-9517. DOI: 10.1016/0021-9517(83)90337-8.

[65] J. W. Whalen. “Physical chemistry of surfaces, fourth edition (Adamson, Arthur W.)” In: *Journal of Chemical Education* 60.11 (Nov. 1983), A322. ISSN: 1938-1328. DOI: 10.1021/ed060pa322.2.

[66] N. Pandey, M. Gupta, J. Stahn. “Study of reactively sputtered nickel nitride thin films”. In: *Journal of Alloys and Compounds* 851 (Jan. 2021), p. 156299. ISSN: 0925-8388. DOI: 10.1016/j.jallcom.2020.156299.

[67] K. Niwa et al. “High Pressure Synthesis and Phase Stability of Nickel Pernitride”. In: *European Journal of Inorganic Chemistry* 2019.33 (Aug. 2019), pp. 3753–3757. ISSN: 1099-0682. DOI: 10.1002/ejic.201900489.

[68] D. Vempaire et al. “Structure and magnetic properties of nickel nitride thin film synthesized by plasma-based ion implantation”. In: *Journal of Magnetism and Magnetic Materials* 272–276 (May 2004), E843–E844. ISSN: 0304-8853. DOI: 10.1016/j.jmmm.2004.01.069.

[69] W. Yu et al. “Spatial distribution study of a nitrogen plasma in an ion-filtered inductively coupled plasma used to grow GaN films”. In: *Journal of Physics D: Applied Physics* 52.39 (July 2019), p. 395101. DOI: 10.1088/1361-6463/ab2ea3.

[70] R. Juza, W. Sachsze. “Zur Kenntnis des Systems Nickel/Stickstoff. Metallamide und Metallnitride, 12. Mitt.” In: *Zeitschrift für anorganische und allgemeine Chemie* 251.2 (Apr. 1943), pp. 201–212. ISSN: 0863-1786. DOI: 10.1002/zaac.19432510205.

[71] N. Shohoji. *Statistical Thermodynamic Approach to Interstitial Non-stoichiometric Compounds (Hydride, Carbide, Nitride, Phosphide and Sulphide)*. Sept. 2013. ISBN: 978-3-659-45506-3.

[72] A. Leineweber, H. Jacobs, S. Hull. “Ordering of Nitrogen in Nickel Nitride Ni3N Determined by Neutron Diffraction”. In: *Inorganic Chemistry* 40.23 (Sept. 2001), pp. 5818–5822. ISSN: 1520-510X. DOI: 10.1021/ic0104860.

[73] E. Lindahl, M. Ottosson, J.-O. Carlsson. “Growth and stability of CVD Ni3N and ALD NiO dual layers”. In: *Surface and Coatings Technology* 205.3 (Oct. 2010), pp. 710–716. ISSN: 0257-8972. DOI: 10.1016/j.surfcoat.2010.07.059.

[74] A. Baiker, M. Maciejewski. “Formation and thermal stability of copper and nickel nitrides”. In: *Journal of the Chemical Society, Faraday Transactions 1: Physical Chemistry in Condensed Phases* 80.8 (1984), p. 2331. ISSN: 0300-9599. DOI: 10.1039/f19848002331.

[75] M. Verhaak, A. van Dillen, J. Geus. “Measuring the acid-base properties of supported nickel catalysts using temperature-programmed desorption of ammonia”. In: *Applied Catalysis A: General* 105.2 (Nov. 1993), pp. 251–269. ISSN: 0926-860X. DOI: 10.1016/0926-860x(93)80251-k.

[76] A.-M. Alexander, J. S. J. Hargreaves, C. Mitchell. “The Reduction of Various Nitrides under Hydrogen: Ni3N, Cu3N, Zn3N2 and Ta3N5”. In: *Topics in Catalysis* 55.14–15 (Aug. 2012), pp. 1046–1053. ISSN: 1572-9028. DOI: 10.1007/s11244-012-9890-3.

[77] Y. Abghoui et al. “Enabling electrochemical reduction of nitrogen to ammonia at ambient conditions through rational catalyst design”. In: *Physical Chemistry Chemical Physics* 17.7 (2015), pp. 4909–4918. ISSN: 1463-9084. DOI: 10.1039/c4cp04838e.

[78] Y. Abghoui, E. Skúlasson. “Transition Metal Nitride Catalysts for Electrochemical Reduction of Nitrogen to Ammonia at Ambient Conditions”. In: *Procedia Computer Science* 51 (2015), pp. 1897–1906. ISSN: 1877-0509. DOI: 10.1016/j.procs.2015.05.433.

[79] Y. Abghoui et al. “Electroreduction of N2 to Ammonia at Ambient Conditions on Mononitrides of Zr, Nb, Cr, and V: A DFT Guide for Experiments”. In: *ACS Catalysis* 6.2 (Dec. 2015), pp. 635–646. ISSN: 2155-5435. DOI: 10.1021/acscatal.5b01918.

[80] T.-N. Ye et al. “Vacancy-enabled N2 activation for ammonia synthesis on an Ni-loaded catalyst”. In: *Nature* 583.7816 (July 2020), pp. 391–395. ISSN: 1476-4687. DOI: 10.1038/s41586-020-2464-9.

[81] X. Ge, X. Wang. “Calculations of Freezing Point Depression, Boiling Point Elevation, Vapor Pressure and Enthalpies of Vaporization of Electrolyte Solutions by a Modified Three-Characteristic Parameter Correlation Model”. In: *Journal of Solution Chemistry* 38.9 (July 2009), pp. 1097–1117. DOI: 10.1007/s10953-009-9433-0.

[82] R. Zaffaroni et al. “Gas Chromatographic Method for In Situ Ammonia Quantification at Parts per Billion Levels”. In: *ACS Energy Letters* 5.12 (Nov. 2020), pp. 3773–3777. ISSN: 2380-8195. DOI: 10.1021/acsenergylett.0c02219.

[83] O. Vaittinen et al. “Adsorption of ammonia on treated stainless steel and polymer surfaces”. In: *Applied Physics B* 115.2 (Aug. 2013), pp. 185–196. ISSN: 1432-0649. DOI: 10.1007/s00340-013-5590-3.

[84] J. R. de Laeter et al. “Atomic weights of the elements. Review 2000 (IUPAC Technical Report)”. In: *Pure and Applied Chemistry* 75.6 (Jan. 2003), p. 738. ISSN: 0033-4545. DOI: 10.1351/pac200375060683.

[85] S. D. Minteer, P. Christopher, S. Linic. “Recent Developments in Nitrogen Reduction Catalysts: A Virtual Issue”. In: *ACS Energy Letters* 4.1 (Dec. 2018), pp. 163–166. ISSN: 2380-8195. DOI: 10.1021/acsenergylett.8b02197.

[86] *Equilibar Research Series Back Pressure Regulators Technical Literature*. 2011.

[87] C. Marozzi, A. Chialvo. “Development of electrode morphologies of interest in electrocatalysis. Part 1: Electrodeposited porous nickel electrodes”. In: *Electrochimica Acta* 45.13 (Mar. 2000), pp. 2111–2120. ISSN: 0013-4686. DOI: 10.1016/s0013-4686(99)00422-3.

[88] K. Siwek et al. “3D nickel foams with controlled morphologies for hydrogen evolution reaction in highly alkaline media”. In: *International Journal of Hydrogen Energy* 44.3 (Jan. 2019), pp. 1701–1709. ISSN: 0360-3199. DOI: 10.1016/j.ijhydene.2018.11.070.

[89] B. J. Plowman, L. A. Jones, S. K. Bhargava. “Building with bubbles: the formation of high surface area honeycomb-like films via hydrogen bubble templated electrodeposition”. In: *Chemical Communications* 51.21 (2015), pp. 4331–4346. DOI: 10.1039/c4cc06638c.

[90] Y. Xu et al. “Honeycomb-like porous 3D nickel electrodeposition for stable Li and Na metal anodes”. In: *Energy Storage Materials* 12 (May 2018), pp. 69–78. DOI: 10.1016/j.ensm.2017.11.011.

[91] J. M. Lee, K. K. Jung, J. S. Ko. “Effect of NaCl in a nickel electrodeposition on the formation of nickel nanostructure”. In: *Journal of Materials Science* 51.6 (Nov. 2015), pp. 3036–3044. ISSN: 1573-4803. DOI: 10.1007/s10853-015-9614-8.

[92] T. Hang et al. “Characterization of nickel nanocones routed by electrodeposition without any template”. In: *Nanotechnology* 19.3 (Dec. 2007), p. 035201. ISSN: 1361-6528. DOI: 10.1088/0957-4484/19/03/035201.

[93] M. Torabi, A. Dolati. “A kinetic study on the electrodeposition of nickel nanostructure and its electrocatalytic activity for hydrogen evolution reaction”. In: *Journal of Applied Electrochemistry* 40.11 (July 2010), pp. 1941–1947. ISSN: 1572-8838. DOI: 10.1007/s10800-010-0170-2.

[94] S. Pilban Jahromi et al. “The effect of supporting electrolyte concentrations on the growth of nickel nanostructures”. In: *Journal of Alloys and Compounds* 880 (Nov. 2021), p. 160408. ISSN: 0925-8388. DOI: 10.1016/j.jallcom.2021.160408.

[95] Z. Chen et al. “Growth and morphology tuning of ordered nickel nanocones routed by one-step pulse electrodeposition”. In: *Applied Surface Science* 508 (Apr. 2020), p. 145291. ISSN: 0169-4332. DOI: 10.1016/j.apsusc.2020.145291.

[96] Z. Ren, P.-X. Gao. “A review of helical nanostructures: growth theories, synthesis strategies and properties”. In: *Nanoscale* 6.16 (Mar. 2014), p. 9366. ISSN: 2040-3372. DOI: 10.1039/c4nr00330f.

[97] P. Gu et al. “Problems in the determination of adsorption behaviour of intermediates in faradaic reactions: Distinction between double layer and adsorption capacitance of electrocatalysts determined from fast potential relaxation transients”. In: *Electrochimica Acta* 37.12 (Sept. 1992), pp. 2145–2154. ISSN: 0013-4686. DOI: 10.1016/0013-4686(92)85105-t.

[98] H.-P. Jia, E. A. Quadrelli. “Mechanistic aspects of dinitrogen cleavage and hydrogenation to produce ammonia in catalysis and organometallic chemistry: relevance of metal hydride bonds and dihydrogen”. In: *Chem. Soc. Rev.* 43.2 (2014), pp. 547–564. ISSN: 1460-4744. DOI: 10.1039/c3cs60206k.

[99] Y. Abghoui, E. Skúlason. “Onset potentials for different reaction mechanisms of nitrogen activation to ammonia on transition metal nitride electro-catalysts”. In: *Catalysis Today* 286 (May 2017), pp. 69–77. ISSN: 0920-5861. DOI: 10.1016/j.cattod.2016.11.047.

[100] D. W. Breck. “Zeolite Molecular Sieves: Structure, Chemistry, and Use”. In: *Journal of Chromatographic Science* 13.4 (Apr. 1975), p. 771. DOI: 10.1093/chromsci/13.4.18a-c.

[101] S. Kunze et al. “Molecular diameters of rarefied gases”. In: *Scientific Reports* 12.1 (Feb. 2022). DOI: 10.1038/s41598-022-05871-y.

A

Appendix A - Supplementary Calculations

A.1. Energy Efficiency for Green HB and NRR

The theoretical maximal energy efficiency for NRR will be based on the thermoneutral cell voltage and 100% faradaic efficiency. The reaction is given by:

$$N_2 + 3H_2O \rightarrow 2NH_3 + \frac{3}{2}O_2 \tag{A.1}$$

The enthalpies of formation for water and ammonia are given by -285.83 kJ mol^{-1} and -46.11 kJ mol^{-1}. These values are used to calculate the thermoneutral voltage.

$$E^0_{tn} = \frac{\Delta H_{f,red} - \Delta H_{f,ox}}{nF} = \frac{-2 \cdot 46.11 + 3 \cdot 285.83}{6F} \cdot 10^3 = 1.32 \text{ V} \tag{A.2}$$

The energy expenditure required to synthesise one tonne NH_3 is given below.

$$\Delta E = \frac{m}{M_{NH_3}} nFE^0_{tn} = \frac{10^6}{17.03} \cdot 3 \cdot 96485 \cdot 1.32 = 22.4 \text{ GJ } t^{-1}_{NH_3} \tag{A.3}$$

The energy consumption of a practical electrochemical ammonia synthesis plant was estimated with the efficiency targets defined in the US Department of Energy's REFUEL program, namely a 300 mA cm^{-2} current density with 90% FE and 60% effective energy efficiency [8]. At this efficiency the energy expenditure of ammonia production would be 37.3 GJ $t^{-1}_{NH_3}$.

In a Green HB process, the water electrolysis consumes some 95 % of the required energy [23].

$$N_2 + 3H_2 \rightarrow 2NH_3 \tag{A.4}$$

One can calculate using the primary HB reaction above that 88.06 kmol H_2 is needed to synthesise one tonne NH_3. Producing this amount of hydrogen using alkaline electrolysis at thermoneutral voltage of 1.48 V gives an energy expenditure of 25.2 GJ $t^{-1}_{NH_3}$. Assuming current best case water electrolysis efficiency of 70% this is expected to be closer to 36 GJ $t^{-1}_{NH_3}$ for only the hydrogen production, and 37.8 GJ $t^{-1}_{NH_3}$ including energy for auxiliary systems.

These rough estimations show that ammonia synthesis using green Haber-Bosch and direct electrochemical NRR will be competitive in terms of energy cost, even in a scenario where drastic improvements to the FE and production rate of NRR are realised in the future. Hence, if such efficiency gains are realised, the advantages of NRR over green HB are not concentrated around energy efficiency, but around smaller scale, decentralised production, and intermittent operation.

A.2. Gas Diffusion of Ammonia in Nitrogen

The diffusion length of ammonia in nitrogen is calculated to determine whether concentration gradients of ammonia can be expected inside the cell. The nitrogen flow follows the shortest path from the inlet to the outlet of the cell, leading to greater flow velocity near the centre of the cylindrical compartment. Diffusion could aid the ammonia produced near the edges in reaching the centre. We use the following formula derived using mean free path theory for the diffusion coefficient of gas A in gas B:

$$D_{AB} = \frac{2}{3}\sqrt{\frac{k_B^3}{\pi^3}}\sqrt{\frac{1}{2m_A}+\frac{1}{2m_B}}\frac{4T^{\frac{3}{2}}}{p(d_A+d_B)^2} \tag{A.5}$$

where

1. $kB = 1.38\ 10^{-23}$ m^2 kg s^{-2} K^{-1}
2. $m_A = 17 \cdot 1.67\ 10^{-27}$ kg ammonia mass
3. $m_B = 28 \cdot 1.67\ 10^{-27}$ kg N_2 mass
4. $p =$ between 0.1 MPa and 1 MPa
5. $T =$ between 293 and 393 K
6. $d_A = 0.26$ nm [100]
7. $d_B = 0.364$ nm molecular diameter of N_2 [101]

Computing the result for room temperature and atmospheric pressure ($T = 293$ K and $p = 100$ kPa) gives.

$$D_{AB} = \frac{2}{3}\sqrt{\frac{(1.38\ 10^{-23})^3}{\pi^3}}\sqrt{\frac{1}{2\cdot 17\cdot 1.67\ 10^{-27}}+\frac{1}{228\cdot 1.67\ 10^{-27}}}\frac{4\cdot 293^{\frac{3}{2}}}{10^5(0.624\ 10^{-9})^2} = 1.68\ 10^{-5} \tag{A.6}$$

in units of m^2s^{-1}, so 0.168 cm^2s^{-1}. With the diffusion length being given by $L = 2\sqrt{Dt}$ this leads to $L = 0.82$ cm for a diffusion time of 1 second.

For $T = 393$ K and $P = 1$ MPa the value changes to $D_{AB} = 0.0261$ cm^2s^{-1} and a diffusion length in 1 second of 0.32 cm.
These results indicate that at room temperature and pressure there is likely no appreciable concentration gradient inside the cell's gas compartment, because ammonia can diffuse from area's where the convection rate is low to the centre, where convection is high. Increasing the pressure does reduce the diffusion length, and the temperature increase does not offer complete compensation, so at these conditions ammonia produced at the edges of the cell will have a slightly longer retention time in the cell. However, the diffusion length is still expected to be sufficient for all ammonia to be carried away and measured.

A.3. Electrodeposition Layer Thickness

Equation A.7 is used for calculating the thickness of a uniform electrodeposition.

$$d_{\text{dep}} = \frac{i\eta\, t}{nF}\frac{M_{\text{Ni}}}{\rho}\cdot 10^4 \tag{A.7}$$

Here d_{dep} is directly converted from cm to microns by the factor 10^4. i is the current density in A cm^{-2}, η the faradaic efficiency, and t the deposition duration. M_{Ni}=58.69 g mol^{-1}, the molar weight of Ni. ρ is the gravimetric density of Ni given by 8.90 g cm^{-3}. The faradaic efficiency is taken as 100% at the moderate current densities used, and n=2 for the reduction of Ni^{2+} ions.

t [s]	i [A cm^{-2}]	d [µm]
180	$5 \cdot 10^{-3}$	0.31
120	$15 \cdot 10^{-3}$	0.62
30	$30 \cdot 10^{-3}$	0.31
300	$30 \cdot 10^{-3}$	3.08

Table A.1: Deposition thicknesses for the used current densities and deposition durations.

A.4. Faradaic Efficiencies

The total FE for ammonia synthesis is first calculated using Equation 2.44 repeated here as Equation A.8.

$$\eta_{NH_3} = \frac{n u_{NH_3} F}{i} \frac{3 u_{NH_3} F}{i} \times 100 \tag{A.8}$$

Next the permeation FE is calculated by adding the H_2 and NH_3 production rates after multiplying these by their number of H atoms per molecule, and dividing by the current density.

$$\eta_{permeation} = \frac{(3 u_{NH_3} + 2 u_{H_2}) F}{i} \times 100 \tag{A.9}$$

Here 2 is used as the charge transfer number for HER. The hydrogenation efficiency is finally calculated by:

$$\eta_{hydr.} = \frac{3 u_{NH_3}}{3 u_{NH_3} + 2 u_{H_2}} \times 100 \tag{A.10}$$

B

Appendix B - Supplementary GC Results

#	i [mA cm^{-2}]	E [V]	T [°C]	p [bar]	H_{perm} [mol cm^{-2} s^{-1}]	H_{perm} FE [%]	u_{H_2} [mol cm^{-2} s^{-1}]	u_{NH_3} [mol cm^{-2} s^{-1}]	Hydr. Eff. [%]	Tot. FE [%]
19	1	1.43	120	1	$6.64 \cdot 10^{-10}$	6.4	$3.32 \cdot 10^{-10}$	$5.83 \cdot 10^{-14}$	0.026	0.0017
20	0.25	1.21	120	1	$2.06 \cdot 10^{-12}$	0.1	$8.44 \cdot 10^{-13}$	$1.24 \cdot 10^{-13}$	18.047	0.0143

Table B.1: Argon measurements results. The row numbers match the raw GC data table in Appendix C. Two or more injections are averaged per cell value.

#	i [mA cm^{-2}]	E [V]	T [°C]	p [bar]	H_{perm} [mol cm^{-2} s^{-1}]	H_{perm} FE [%]	u_{H_2} [mol cm^{-2} s^{-1}]	u_{NH_3} [mol cm^{-2} s^{-1}]	Hydr. Eff. [%]	Tot. FE [%]
21	0.38	1.71	20	1	$3.74 \cdot 10^{-10}$	9.4	$1.87 \cdot 10^{-10}$	$5.32 \cdot 10^{-14}$	0.043	0.0040
22	1.59	1.78	20	1	$6.01 \cdot 10^{-10}$	3.6	$3.01 \cdot 10^{-10}$	$8.66 \cdot 10^{-14}$	0.043	0.0016

Table B.2: Results for cell with enhanced electrode wetting. The geometric surface area had a diameter of 2 cm, giving an electrode area of 3.14 cm^2. The row numbers match the raw GC data table in Appendix C. Two or more injections are averaged per cell value.

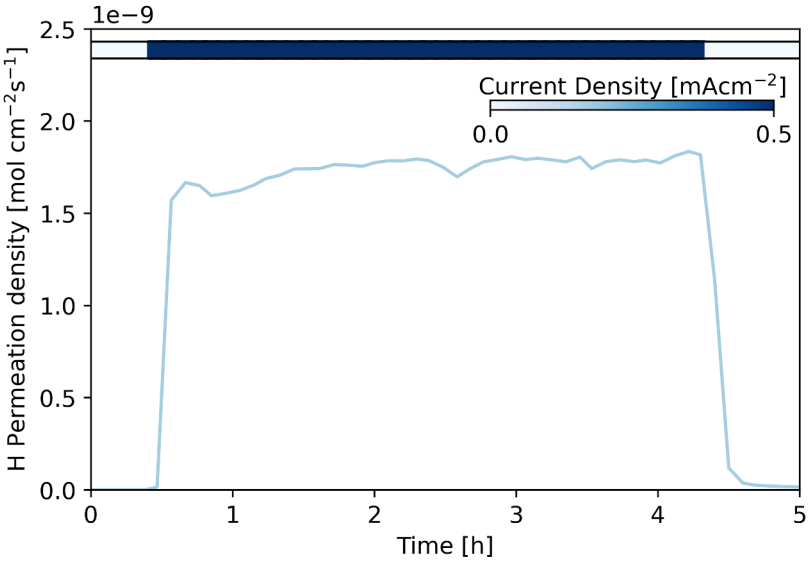

Figure B.1: Constant H permeation during a 4 hour chronopotentiometry cycle. The measurement was conducted on the 12 cm^2 cell at atmospheric pressure and 120 °C, with a 0.5 mA cm^{-2} current density.

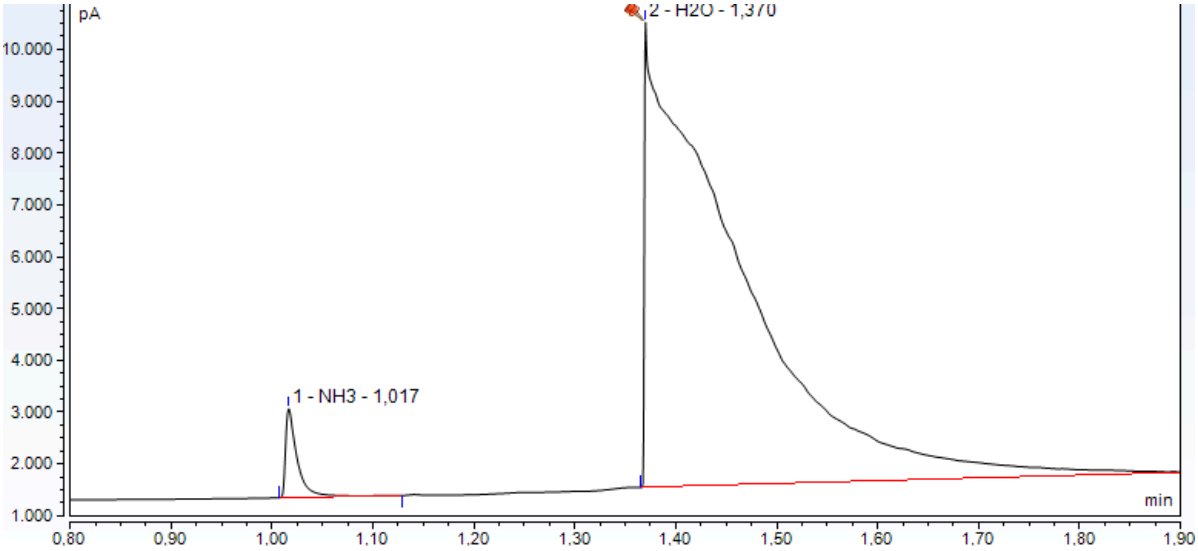

Figure B.2: Largest NH_3 peak recorded with the HPE cell, with an area of 23.1 pA min. The chromatogram was recorded during the experiment with electroplated HPE and N_2 inlet gas with 4% H_2.

C

Appendix C - Raw GC Data

Table C.1: Raw GC data. The row numbers in the # column correspond to the row numbers in the result tables. When two injection numbers are given, the left injection pertains to H_2 and the right to NH_3. Two different injections were taken because ammonia had a significantly longer retention time in the cell on the experiment with 1 $mL_n\,min^{-1}$ flow rate 8 bar pressure.

#	Date	Inj.	p.a. H_2	ppm H_2	p.a. NH_3	ppm NH_3	Mass flow rate [$mL_n\,min^{-1}$]	Molar flow rate [$mol\,s^{-1}$]
1	20230428	64	0.130	446.9	0.4112	0.416	1	7.34E-07
	20230428	65	0.1324	456.6	0.4172	0.422	1	7.34E-07
2	20230703	39	4.0577	13992.1	2.1237	2.150	1	7.34E-07
	20230703	51	4.0669	14023.8	2.5028	2.534	1	7.34E-07
	20230703	63	4.1476	14302.1	2.5737	2.605	1	7.34E-07
3	20230706	67	5.5151	19017.6	0.4774	0.483	1	7.34E-07
	20230706	70	5.1702	17828.3	0.5752	0.582	1	7.34E-07
	20230706	73	5.3808	18554.5	0.5405	0.547	1	7.34E-07
4	20230706	90	7.1428	24630.3	0.393	0.398	1	7.34E-07
	20230706	94	7.3122	25214.5	0.4799	0.486	1	7.34E-07
5	20230929	9	0.0062	21.4	0.9049	0.916	1	7.34E-07
	20230929	10	0.0062	21.4	0.9553	0.967	1	7.34E-07
6	20230929	20	0.0759	261.7	0.4914	0.497	1	7.34E-07
	20230929	23	0.0748	257.9	0.514	0.520	1	7.34E-07
7	20231106	9	0.0008	2.8	2.6765	2.710	1	7.34E-07
	20231106	12	0.001	3.4	2.2873	2.316	1	7.34E-07
8	20231026	68	0.1142	393.8	1.3735	1.390	1	7.34E-07
	20231026	76	0.0939	323.8	1.0387	1.052	1	7.34E-07
9	20231016	51	0.7979	2751.4	1.1424	1.157	1	7.34E-07
	20231016	53	0.7616	2626.2	1.164	1.178	1	7.34E-07
10	20231026	225	0.6766	2333.1	0.1524	0.154	1	7.34E-07
11	20230710	40	3.8793	13376.9	3.5607	3.605	1	7.34E-07
	20230710	56	3.4797	11999.0	3.2343	3.274	1	7.34E-07
12	20230713	40	3.584	12358.6	3.384	3.426	1	7.34E-07
	20230713	57	3.6047	12430.0	2.5715	2.603	1	7.34E-07
13	20230717	20/30	4.4612	15383.4	3.709	3.755	1	7.34E-07
	20230717	21/38	4.4027	15181.7	3.5236	3.567	1	7.34E-07
14	20230717	295	2.5092	8652.4	0.5017	0.508	1	7.34E-07
	20230717	300	2.5822	8904.1	0.6297	0.637	1	7.34E-07
15	20231208-1	10	0.0115	39.7	1.775	1.797	4	2.94E-06
	20231208-1	11	0.0071	24.5	1.5858	1.605	4	2.94E-06
16	20231211	10	0.0666	229.7	0.8304	0.841	8	5.87E-06
	20231211	12	0.0582	200.7	0.6078	0.615	8	5.87E-06
17	20231208-1	23	0.3146	1084.8	0.2027	0.205	4	2.94E-06
	20231208-1	25	0.3287	1133.4	0.1879	0.190	4	2.94E-06
18	20231208	7	0.5215	1798.3	3.9015	3.950	4	2.94E-06
	20231208	9	0.5184	1787.6	1.9948	2.019	4	2.94E-06

#	Date	Inj.	p.a. H_2	ppm H_2	p.a. NH_3	ppm NH_3	Mass flow rate [$mL_n\ min^{-1}$]	Molar flow rate [$mol\ s^{-1}$]
19	20231120	242	0.3245	1119.0	0.1879	0.190	1	7.34E-07
	20231120	255	0.3044	1049.7	0.1883	0.191	1	7.34E-07
20	20231120	79	0.0008	2.8	0.4324	0.438	1	7.34E-07
	20231120	82	0.0008	2.8	0.3677	0.372	1	7.34E-07
21	20231010	14	0.2395	825.9	0.2037	0.206	1	7.34E-07
	20231010	19	0.2238	771.7	0.2460	0.249	1	7.34E-07
22	20231010	66	0.3961	1365.9	0.4160	0.421	1	7.34E-07
	20231010	70	0.3494	1204.8	0.3156	0.319	1	7.34E-07

Table C.2: GC calibration data for the N_2 calibration gas with 18.8 ppm NH_3.

Mass flow rate [$mL_N\ min^{-1}$]	p.a. NH_3	Slope
1	18.75	0.9877
1	18.61	
1	18.513	
1	18.506	
1	18.474	
2	18.9	1.010
2	18.913	
2	18.913	
2	18.952	
2	19.201	
2	18.953	
2	19.097	

Mass flow rate [$mL_N\ min^{-1}$]	p.a. NH_3	Slope
5	20.411	1.0907
5	20.449	
5	20.507	
5	20.445	
5	20.618	
5	20.605	
10	19.966	1.083
10	20.113	
10	20.261	
10	20.515	
10	20.641	
10	20.74	

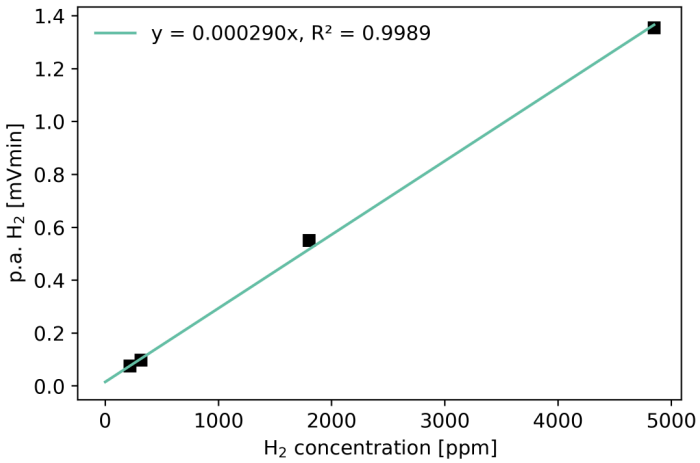

Figure C.1: GC calibration curve for H_2. The calibration was carried out using a certified calibration gas of 4% H_2 in N_2, diluting to the chosen concentration with N_2. Each data point is the average of three or more repeated measurements. Data from [6].

D

Appendix D - NiN HPE Composition

D.1. XPS Depth Profiles

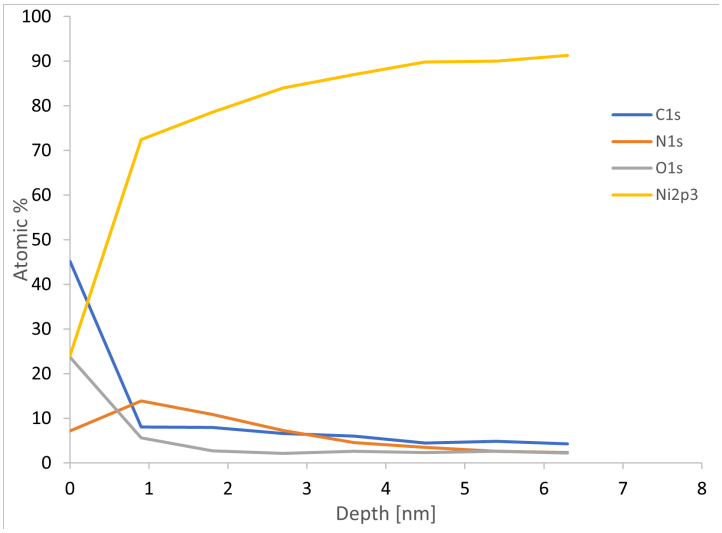

(a) XPS depth profile of an unused sample nitrided with the AJA process.

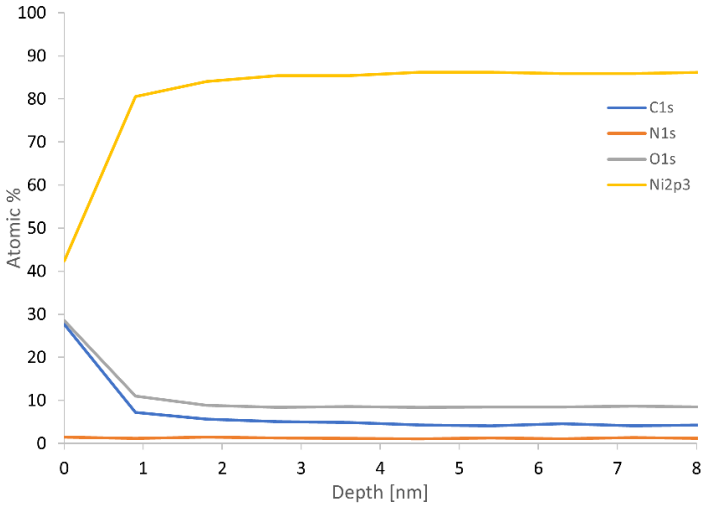

(b) XPS depth profile of a used sample nitrided with the AJA process.

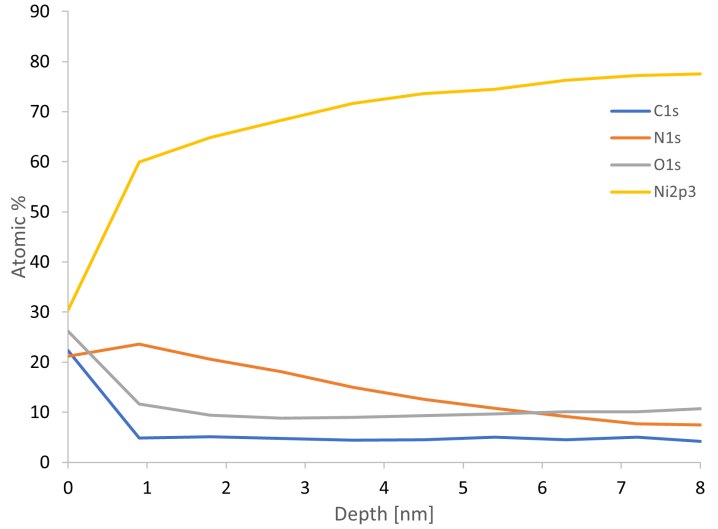

(c) XPS depth profile of an unused sample nitrided with the ALD process.

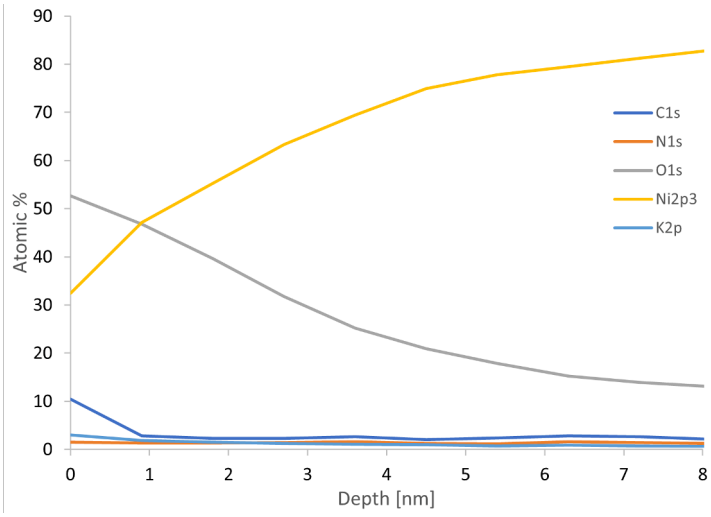

(d) XPS depth profile of a used sample nitrided with the ALD process.

Figure D.1: XPS depth profiles of HPE samples.

D.2. N Content Estimation

The nitrogen content of the samples can be estimated based on the XPS depth profiles above. The stoichiometry of each etch level is calculated by taking the ratio of N and Ni atomic percentages. This ratio is divided by the standard Ni:N=3:1 ratio, and multiplied by the etch distance of 0.9 nm based on the etch rate of 0.09 nm s^{-1} and etch time of 10 s per level. This is based on the assumption that a 1 nm thick layer of Ni:N=6:1 contains the same amount of N atoms as a 0.5 nm layer of Ni:N=3:1. Differences in density between varying stoichiometries are disregarded. The formula for the Ni_3N equivalent layer thickness is given below.

$$d = \sum_{k=1}^{n} \frac{N\%_k / Ni\%_k}{1/3} \cdot 0.9\,\text{nm} \tag{D.1}$$

With the estimated thickness of a pure Ni_3N layer containing the same amount of N as the sample, the atomic density of N in the HPE τ_N in mol cm^{-2} can be calculated using Equation D.2.

$$\tau = \frac{\rho d}{M_{Ni_3N}} \cdot 10^2 \tag{D.2}$$

The results of the calculation are given in Table D.1.

	Equivalent Ni_3N layer d [nm]	τ_N [mol cm^{-2}]	N reacted [mol]	Remaining N [%]	ML equivalent [-]
AJA	2.31	$9.38 \cdot 10^{-9}$		100.0	8.07
Used AJA	0.44	$1.77 \cdot 10^{-9}$	$7.61 \cdot 10^{-9}$	18.9	1.53
ALD	6.78	$2.75 \cdot 10^{-8}$		100.0	23.67
Used ALD	0.61	$2.49 \cdot 10^{-9}$	$2.50 \cdot 10^{-8}$	9.1	2.14

Table D.1: N content of the nitride layer before and after NH_3 synthesis. The ML equivalent is the number of N atoms divided by $7 \cdot 10^{14}$, the atoms in one ML of adsorbed N.